

Measurement of the $t\bar{t}$ Production Cross Section in $p\bar{p}$ collisions at $\sqrt{s} = 1.96$ TeV using Lepton+Jets Events with Jet Probability b-tagging

A. Abulencia,²³ D. Acosta,¹⁷ J. Adelman,¹³ T. Affolder,¹⁰ T. Akimoto,⁵⁵ M.G. Albrow,¹⁶ D. Ambrose,¹⁶ S. Amerio,⁴³ D. Amidei,³⁴ A. Anastassov,⁵² K. Anikeev,¹⁶ A. Annovi,¹⁸ J. Antos,¹ M. Aoki,⁵⁵ G. Apollinari,¹⁶ J.-F. Arguin,³³ T. Arisawa,⁵⁷ A. Artikov,¹⁴ W. Ashmanskas,¹⁶ A. Attal,⁸ F. Azfar,⁴² P. Azzi-Bacchetta,⁴³ P. Azzurri,⁴⁶ N. Bacchetta,⁴³ H. Bachacou,²⁸ W. Badgett,¹⁶ A. Barbaro-Galtieri,²⁸ V.E. Barnes,⁴⁸ B.A. Barnett,²⁴ S. Baroiant,⁷ V. Bartsch,³⁰ G. Bauer,³² F. Bedeschi,⁴⁶ S. Behari,²⁴ S. Belforte,⁵⁴ G. Bellettini,⁴⁶ J. Bellinger,⁵⁹ A. Belloni,³² E. Ben Haim,⁴⁴ D. Benjamin,¹⁵ A. Beretvas,¹⁶ J. Beringer,²⁸ T. Berry,²⁹ A. Bhatti,⁵⁰ M. Binkley,¹⁶ D. Bisello,⁴³ R. E. Blair,² C. Blocker,⁶ B. Blumenfeld,²⁴ A. Bocci,¹⁵ A. Bodek,⁴⁹ V. Boisvert,⁴⁹ G. Bolla,⁴⁸ A. Bolshov,³² D. Bortoletto,⁴⁸ J. Boudreau,⁴⁷ A. Boveia,¹⁰ B. Brau,¹⁰ C. Bromberg,³⁵ E. Brubaker,¹³ J. Budagov,¹⁴ H.S. Budd,⁴⁹ S. Budd,²³ K. Burkett,¹⁶ G. Busetto,⁴³ P. Bussey,²⁰ K. L. Byrum,² S. Cabrera,¹⁵ M. Campanelli,¹⁹ M. Campbell,³⁴ F. Canelli,⁸ A. Canepa,⁴⁸ D. Carlsmith,⁵⁹ R. Carosi,⁴⁶ S. Carron,¹⁵ M. Casarsa,⁵⁴ A. Castro,⁵ P. Catastini,⁴⁶ D. Cauz,⁵⁴ M. Cavalli-Sforza,³ A. Cerri,²⁸ L. Cerrito,⁴² S.H. Chang,²⁷ J. Chapman,³⁴ Y.C. Chen,¹ M. Chertok,⁷ G. Chiarelli,⁴⁶ G. Chlachidze,¹⁴ F. Chlebana,¹⁶ I. Cho,²⁷ K. Cho,²⁷ D. Chokheli,¹⁴ J.P. Chou,²¹ P.H. Chu,²³ S.H. Chuang,⁵⁹ K. Chung,¹² W.H. Chung,⁵⁹ Y.S. Chung,⁴⁹ M. Ciljak,⁴⁶ C.I. Ciobanu,²³ M.A. Ciocchi,⁴⁶ A. Clark,¹⁹ D. Clark,⁶ M. Coca,¹⁵ G. Compostella,⁴³ M.E. Convery,⁵⁰ J. Conway,⁷ B. Cooper,³⁰ K. Copic,³⁴ M. Cordelli,¹⁸ G. Cortiana,⁴³ F. Cresciolo,⁴⁶ A. Cruz,¹⁷ C. Cuenca Almenar,⁷ J. Cuevas,¹¹ R. Culbertson,¹⁶ D. Cyr,⁵⁹ S. DaRonco,⁴³ S. D'Auria,²⁰ M. D'Onofrio,³ D. Dagenhart,⁶ P. de Barbaro,⁴⁹ S. De Cecco,⁵¹ A. Deisher,²⁸ G. De Lentdecker,⁴⁹ M. Dell'Orso,⁴⁶ F. Delli Paoli,⁴³ S. Demers,⁴⁹ L. Demortier,⁵⁰ J. Deng,¹⁵ M. Deninno,⁵ D. De Pedis,⁵¹ P.F. Derwent,¹⁶ C. Dionisi,⁵¹ J.R. Dittmann,⁴ P. DiToro,⁵² C. Dörr,²⁵ S. Donati,⁴⁶ M. Donega,¹⁹ P. Dong,⁸ J. Donini,⁴³ T. Dorigo,⁴³ S. Dube,⁵² K. Ebina,⁵⁷ J. Efron,³⁹ J. Ehlers,¹⁹ R. Erbacher,⁷ D. Errede,²³ S. Errede,²³ R. Eusebi,¹⁶ H.C. Fang,²⁸ S. Farrington,²⁹ I. Fedorko,⁴⁶ W.T. Fedorko,¹³ R.G. Feild,⁶⁰ M. Feindt,²⁵ J.P. Fernandez,³¹ R. Field,¹⁷ G. Flanagan,⁴⁸ L.R. Flores-Castillo,⁴⁷ A. Foland,²¹ S. Forrester,⁷ G.W. Foster,¹⁶ M. Franklin,²¹ J.C. Freeman,²⁸ I. Furic,¹³ M. Gallinaro,⁵⁰ J. Galyardt,¹² J.E. Garcia,⁴⁶ M. Garcia Sciveres,²⁸ A.F. Garfinkel,⁴⁸ C. Gay,⁶⁰ H. Gerberich,²³ D. Gerdes,³⁴ S. Giagu,⁵¹ P. Giannetti,⁴⁶ A. Gibson,²⁸ K. Gibson,¹² C. Ginsburg,¹⁶ N. Giokaris,¹⁴ K. Giolo,⁴⁸ M. Giordani,⁵⁴ P. Giromini,¹⁸ M. Giunta,⁴⁶ G. Giurgiu,¹² V. Glagolev,¹⁴ D. Glenzinski,¹⁶ M. Gold,³⁷ N. Goldschmidt,³⁴ J. Goldstein,⁴² G. Gomez,¹¹ G. Gomez-Ceballos,¹¹ M. Goncharov,⁵³ O. González,³¹ I. Gorelov,³⁷ A.T. Goshaw,¹⁵ Y. Gotra,⁴⁷ K. Goulianos,⁵⁰ A. Gresele,⁴³ M. Griffiths,²⁹ S. Grinstein,²¹ C. Grosso-Pilcher,¹³ R.C. Group,¹⁷ U. Grundler,²³ J. Guimaraes da Costa,²¹ Z. Gunay-Unalan,³⁵ C. Haber,²⁸ S.R. Hahn,¹⁶ K. Hahn,⁴⁵ E. Halkiadakis,⁵² A. Hamilton,³³ B.-Y. Han,⁴⁹ J.Y. Han,⁴⁹ R. Handler,⁵⁹ F. Happacher,¹⁸ K. Hara,⁵⁵ M. Hare,⁵⁶ S. Harper,⁴² R.F. Harr,⁵⁸ R.M. Harris,¹⁶ K. Hatakeyama,⁵⁰ J. Hauser,⁸ C. Hays,¹⁵ A. Heijboer,⁴⁵ B. Heinemann,²⁹ J. Heinrich,⁴⁵ M. Herndon,⁵⁹ D. Hidas,¹⁵ C.S. Hill,¹⁰ D. Hirschbuehl,²⁵ A. Hocker,¹⁶ A. Holloway,²¹ S. Hou,¹ M. Houlden,²⁹ S.-C. Hsu,⁹ B.T. Huffman,⁴² R.E. Hughes,³⁹ J. Huston,³⁵ J. Incandela,¹⁰ G. Introzzi,⁴⁶ M. Iori,⁵¹ Y. Ishizawa,⁵⁵ A. Ivanov,⁷ B. Iyutin,³² E. James,¹⁶ D. Jang,⁵² B. Jayatilaka,³⁴ D. Jeans,⁵¹ H. Jensen,¹⁶ E.J. Jeon,²⁷ S. Jindariani,¹⁷ M. Jones,⁴⁸ K.K. Joo,²⁷ S.Y. Jun,¹² T.R. Junk,²³ T. Kamon,⁵³ J. Kang,³⁴ P.E. Karchin,⁵⁸ Y. Kato,⁴¹ Y. Kemp,²⁵ R. Kephart,¹⁶ U. Kerzel,²⁵ V. Khotilovich,⁵³ B. Kilminster,³⁹ D.H. Kim,²⁷ H.S. Kim,²⁷ J.E. Kim,²⁷ M.J. Kim,¹² S.B. Kim,²⁷ S.H. Kim,⁵⁵ Y.K. Kim,¹³ L. Kirsch,⁶ S. Klimenko,¹⁷ M. Klute,³² B. Knuteson,³² B.R. Ko,¹⁵ H. Kobayashi,⁵⁵ K. Kondo,⁵⁷ D.J. Kong,²⁷ J. Konigsberg,¹⁷ A. Korytov,¹⁷ A.V. Kotwal,¹⁵ A. Kovalev,⁴⁵ A. Kraan,⁴⁵ J. Kraus,²³ I. Kravchenko,³² M. Kreps,²⁵ J. Kroll,⁴⁵ N. Krumnack,⁴ M. Kruse,¹⁵ V. Krutelyov,⁵³ S. E. Kuhlmann,² Y. Kusakabe,⁵⁷ S. Kwang,¹³ A.T. Laasanen,⁴⁸ S. Lai,³³ S. Lami,⁴⁶ S. Lammel,¹⁶ M. Lancaster,³⁰ R.L. Lander,⁷ K. Lannon,³⁹ A. Lath,⁵² G. Latino,⁴⁶ I. Lazzizzera,⁴³ T. LeCompte,² J. Lee,⁴⁹ J. Lee,²⁷ Y.J. Lee,²⁷ S.W. Lee,⁵³ R. Lefèvre,³ N. Leonardo,³² S. Leone,⁴⁶ S. Levy,¹³ J.D. Lewis,¹⁶ C. Lin,⁶⁰ C.S. Lin,¹⁶ M. Lindgren,¹⁶ E. Lipeles,⁹ T.M. Liss,²³ A. Lister,¹⁹ D.O. Litvintsev,¹⁶ T. Liu,¹⁶ N.S. Lockyer,⁴⁵ A. Loginov,³⁶ M. Loreti,⁴³ P. Loverre,⁵¹ R.-S. Lu,¹ D. Lucchesi,⁴³ P. Lujan,²⁸ P. Lukens,¹⁶ G. Lungu,¹⁷ L. Lyons,⁴² J. Lys,²⁸ R. Lysak,¹ E. Lytken,⁴⁸ P. Mack,²⁵ D. MacQueen,³³ R. Madrak,¹⁶ K. Maeshima,¹⁶ T. Maki,²² P. Maksimovic,²⁴ S. Malde,⁴² G. Manca,²⁹

F. Margaroli,⁵ R. Marginean,¹⁶ C. Marino,²³ A. Martin,⁶⁰ V. Martin,³⁸ M. Martínez,³ T. Maruyama,⁵⁵ P. Mastrandrea,⁵¹ H. Matsunaga,⁵⁵ M.E. Mattson,⁵⁸ R. Mazini,³³ P. Mazzanti,⁵ K.S. McFarland,⁴⁹ P. McIntyre,⁵³ R. McNulty,²⁹ A. Mehta,²⁹ S. Menzemer,¹¹ A. Menzione,⁴⁶ P. Merkel,⁴⁸ C. Mesropian,⁵⁰ A. Messina,⁵¹ M. von der Mey,⁸ T. Miao,¹⁶ N. Miladinovic,⁶ J. Miles,³² R. Miller,³⁵ J.S. Miller,³⁴ C. Mills,¹⁰ M. Milnik,²⁵ R. Miquel,²⁸ A. Mitra,¹ G. Mitselmakher,¹⁷ A. Miyamoto,²⁶ N. Moggi,⁵ B. Mohr,⁸ R. Moore,¹⁶ M. Morello,⁴⁶ P. Movilla Fernandez,²⁸ J. Mülmenstädt,²⁸ A. Mukherjee,¹⁶ Th. Müller,²⁵ R. Mumford,²⁴ P. Murat,¹⁶ J. Nachtman,¹⁶ J. Naganoma,⁵⁷ S. Nahn,³² I. Nakano,⁴⁰ A. Napier,⁵⁶ D. Naumov,³⁷ V. Nečula,¹⁷ C. Neu,⁴⁵ M.S. Neubauer,⁹ J. Nielsen,²⁸ T. Nigmanov,⁴⁷ L. Nodulman,² O. Norniella,³ E. Nurse,³⁰ T. Ogawa,⁵⁷ S.H. Oh,¹⁵ Y.D. Oh,²⁷ T. Okusawa,⁴¹ R. Oldeman,²⁹ R. Orava,²² K. Osterberg,²² C. Pagliarone,⁴⁶ E. Palencia,¹¹ R. Paoletti,⁴⁶ V. Papadimitriou,¹⁶ A.A. Paramonov,¹³ B. Parks,³⁹ S. Pashapour,³³ J. Patrick,¹⁶ G. Pauletta,⁵⁴ M. Paulini,¹² C. Paus,³² D.E. Pellett,⁷ A. Penzo,⁵⁴ T.J. Phillips,¹⁵ G. Piacentino,⁴⁶ J. Piedra,⁴⁴ L. Pinera,¹⁷ K. Pitts,²³ C. Plager,⁸ L. Pondrom,⁵⁹ X. Portell,³ O. Poukhov,¹⁴ N. Pounder,⁴² F. Prakoshyn,¹⁴ A. Pronko,¹⁶ J. Proudfoot,² F. Ptohos,¹⁸ G. Punzi,⁴⁶ J. Pursley,²⁴ J. Rademacker,⁴² A. Rahaman,⁴⁷ A. Rakitin,³² S. Rappoccio,²¹ F. Ratnikov,⁵² B. Reisert,¹⁶ V. Rekovic,³⁷ N. van Remortel,²² P. Renton,⁴² M. Rescigno,⁵¹ S. Richter,²⁵ F. Rimondi,⁵ L. Ristori,⁴⁶ W.J. Robertson,¹⁵ A. Robson,²⁰ T. Rodrigo,¹¹ E. Rogers,²³ S. Rolli,⁵⁶ R. Roser,¹⁶ M. Rossi,⁵⁴ R. Rossin,¹⁷ C. Rott,⁴⁸ A. Ruiz,¹¹ J. Russ,¹² V. Rusu,¹³ H. Saarikko,²² S. Sabik,³³ A. Safonov,⁵³ W.K. Sakumoto,⁴⁹ G. Salamanna,⁵¹ O. Saltó,³ D. Saltzberg,⁸ C. Sanchez,³ L. Santi,⁵⁴ S. Sarkar,⁵¹ L. Sartori,⁴⁶ K. Sato,⁵⁵ P. Savard,³³ A. Savoy-Navarro,⁴⁴ T. Scheidle,²⁵ P. Schlabach,¹⁶ E.E. Schmidt,¹⁶ M.P. Schmidt,⁶⁰ M. Schmitt,³⁸ T. Schwarz,³⁴ L. Scodellaro,¹¹ A.L. Scott,¹⁰ A. Scribano,⁴⁶ F. Scuri,⁴⁶ A. Sedov,⁴⁸ S. Seidel,³⁷ Y. Seiya,⁴¹ A. Semenov,¹⁴ L. Sexton-Kennedy,¹⁶ I. Sfiligoi,¹⁸ M.D. Shapiro,²⁸ T. Shears,²⁹ P.F. Shepard,⁴⁷ D. Sherman,²¹ M. Shimojima,⁵⁵ M. Shochet,¹³ Y. Shon,⁵⁹ I. Shreyber,³⁶ A. Sidoti,⁴⁴ P. Sinervo,³³ A. Sisakyan,¹⁴ J. Sjolín,⁴² A. Skiba,²⁵ A.J. Slaughter,¹⁶ K. Sliwa,⁵⁶ J.R. Smith,⁷ F.D. Snider,¹⁶ R. Snihur,³³ M. Soderberg,³⁴ A. Soha,⁷ S. Somalwar,⁵² V. Sorin,³⁵ J. Spalding,¹⁶ M. Spezziga,¹⁶ F. Spinella,⁴⁶ T. Spreitzer,³³ P. Squillacioti,⁴⁶ M. Stanitzki,⁶⁰ A. Staveris-Polykalas,⁴⁶ R. St. Denis,²⁰ B. Stelzer,⁸ O. Stelzer-Chilton,⁴² D. Stentz,³⁸ J. Strologas,³⁷ D. Stuart,¹⁰ J.S. Suh,²⁷ A. Sukhanov,¹⁷ K. Sumorok,³² H. Sun,⁵⁶ T. Suzuki,⁵⁵ A. Taffard,²³ R. Takashima,⁴⁰ Y. Takeuchi,⁵⁵ K. Takikawa,⁵⁵ M. Tanaka,² R. Tanaka,⁴⁰ N. Tanimoto,⁴⁰ M. Tecchio,³⁴ P.K. Teng,¹ K. Terashi,⁵⁰ S. Tether,³² J. Thom,¹⁶ A.S. Thompson,²⁰ E. Thomson,⁴⁵ P. Tipton,⁴⁹ V. Tiwari,¹² S. Tkaczyk,¹⁶ D. Toback,⁵³ S. Tokar,¹⁴ K. Tollefson,³⁵ T. Tomura,⁵⁵ D. Tonelli,⁴⁶ M. Tönnemann,³⁵ S. Torre,¹⁸ D. Torretta,¹⁶ S. Tourneur,⁴⁴ W. Trischuk,³³ R. Tsuchiya,⁵⁷ S. Tsuno,⁴⁰ N. Turini,⁴⁶ F. Ukegawa,⁵⁵ T. Unverhau,²⁰ S. Uozumi,⁵⁵ D. Usynin,⁴⁵ A. Vaiciulis,⁴⁹ S. Vallecorsa,¹⁹ A. Varganov,³⁴ E. Vataga,³⁷ G. Velev,¹⁶ G. Veramendi,²³ V. Veszpremi,⁴⁸ R. Vidal,¹⁶ I. Vila,¹¹ R. Vilar,¹¹ T. Vine,³⁰ I. Vollrath,³³ I. Volobouev,²⁸ G. Volpi,⁴⁶ F. Würthwein,⁹ P. Wagner,⁵³ R. G. Wagner,² R.L. Wagner,¹⁶ W. Wagner,²⁵ R. Wallny,⁸ T. Walter,²⁵ Z. Wan,⁵² S.M. Wang,¹ A. Warburton,³³ S. Waschke,²⁰ D. Waters,³⁰ W.C. Wester III,¹⁶ B. Whitehouse,⁵⁶ D. Whiteson,⁴⁵ A.B. Wicklund,² E. Wicklund,¹⁶ G. Williams,³³ H.H. Williams,⁴⁵ P. Wilson,¹⁶ B.L. Winer,³⁹ P. Wittich,¹⁶ S. Wolbers,¹⁶ C. Wolfe,¹³ T. Wright,³⁴ X. Wu,¹⁹ S.M. Wynne,²⁹ A. Yagil,¹⁶ K. Yamamoto,⁴¹ J. Yamaoka,⁵² T. Yamashita,⁴⁰ C. Yang,⁶⁰ U.K. Yang,¹³ Y.C. Yang,²⁷ W.M. Yao,²⁸ G.P. Yeh,¹⁶ J. Yoh,¹⁶ K. Yorita,¹³ T. Yoshida,⁴¹ G.B. Yu,⁴⁹ I. Yu,²⁷ S.S. Yu,¹⁶ J.C. Yun,¹⁶ L. Zanello,⁵¹ A. Zanetti,⁵⁴ I. Zaw,²¹ F. Zetti,⁴⁶ X. Zhang,²³ J. Zhou,⁵² and S. Zucchelli⁵

(CDF Collaboration)

¹*Institute of Physics, Academia Sinica, Taipei, Taiwan 11529, Republic of China*

²*Argonne National Laboratory, Argonne, Illinois 60439*

³*Institut de Física d'Altes Energies, Universitat Autònoma de Barcelona, E-08193, Bellaterra (Barcelona), Spain*

⁴*Baylor University, Waco, Texas 76798*

⁵*Istituto Nazionale di Fisica Nucleare, University of Bologna, I-40127 Bologna, Italy*

⁶*Brandeis University, Waltham, Massachusetts 02254*

⁷*University of California, Davis, Davis, California 95616*

⁸*University of California, Los Angeles, Los Angeles, California 90024*

⁹*University of California, San Diego, La Jolla, California 92093*

¹⁰*University of California, Santa Barbara, Santa Barbara, California 93106*

- ¹¹*Instituto de Fisica de Cantabria, CSIC-University of Cantabria, 39005 Santander, Spain*
- ¹²*Carnegie Mellon University, Pittsburgh, PA 15213*
- ¹³*Enrico Fermi Institute, University of Chicago, Chicago, Illinois 60637*
- ¹⁴*Joint Institute for Nuclear Research, RU-141980 Dubna, Russia*
- ¹⁵*Duke University, Durham, North Carolina 27708*
- ¹⁶*Fermi National Accelerator Laboratory, Batavia, Illinois 60510*
- ¹⁷*University of Florida, Gainesville, Florida 32611*
- ¹⁸*Laboratori Nazionali di Frascati, Istituto Nazionale di Fisica Nucleare, I-00044 Frascati, Italy*
- ¹⁹*University of Geneva, CH-1211 Geneva 4, Switzerland*
- ²⁰*Glasgow University, Glasgow G12 8QQ, United Kingdom*
- ²¹*Harvard University, Cambridge, Massachusetts 02138*
- ²²*Division of High Energy Physics, Department of Physics, University of Helsinki and Helsinki Institute of Physics, FIN-00014, Helsinki, Finland*
- ²³*University of Illinois, Urbana, Illinois 61801*
- ²⁴*The Johns Hopkins University, Baltimore, Maryland 21218*
- ²⁵*Institut für Experimentelle Kernphysik, Universität Karlsruhe, 76128 Karlsruhe, Germany*
- ²⁶*High Energy Accelerator Research Organization (KEK), Tsukuba, Ibaraki 305, Japan*
- ²⁷*Center for High Energy Physics: Kyungpook National University, Taegu 702-701, Korea; Seoul National University, Seoul 151-742, Korea; and SungKyunKwan University, Suwon 440-746, Korea*
- ²⁸*Ernest Orlando Lawrence Berkeley National Laboratory, Berkeley, California 94720*
- ²⁹*University of Liverpool, Liverpool L69 7ZE, United Kingdom*
- ³⁰*University College London, London WC1E 6BT, United Kingdom*
- ³¹*Centro de Investigaciones Energeticas Medioambientales y Tecnologicas, E-28040 Madrid, Spain*
- ³²*Massachusetts Institute of Technology, Cambridge, Massachusetts 02139*
- ³³*Institute of Particle Physics: McGill University, Montréal, Canada H3A 2T8; and University of Toronto, Toronto, Canada M5S 1A7*
- ³⁴*University of Michigan, Ann Arbor, Michigan 48109*
- ³⁵*Michigan State University, East Lansing, Michigan 48824*
- ³⁶*Institution for Theoretical and Experimental Physics, ITEP, Moscow 117259, Russia*
- ³⁷*University of New Mexico, Albuquerque, New Mexico 87131*
- ³⁸*Northwestern University, Evanston, Illinois 60208*
- ³⁹*The Ohio State University, Columbus, Ohio 43210*
- ⁴⁰*Okayama University, Okayama 700-8530, Japan*
- ⁴¹*Osaka City University, Osaka 588, Japan*
- ⁴²*University of Oxford, Oxford OX1 3RH, United Kingdom*
- ⁴³*University of Padova, Istituto Nazionale di Fisica Nucleare, Sezione di Padova-Trento, I-35131 Padova, Italy*
- ⁴⁴*LPNHE, Universite Pierre et Marie Curie/IN2P3-CNRS, UMR7585, Paris, F-75252 France*
- ⁴⁵*University of Pennsylvania, Philadelphia, Pennsylvania 19104*
- ⁴⁶*Istituto Nazionale di Fisica Nucleare Pisa, Universities of Pisa, Siena and Scuola Normale Superiore, I-56127 Pisa, Italy*
- ⁴⁷*University of Pittsburgh, Pittsburgh, Pennsylvania 15260*
- ⁴⁸*Purdue University, West Lafayette, Indiana 47907*
- ⁴⁹*University of Rochester, Rochester, New York 14627*
- ⁵⁰*The Rockefeller University, New York, New York 10021*
- ⁵¹*Istituto Nazionale di Fisica Nucleare, Sezione di Roma 1, University of Rome "La Sapienza," I-00185 Roma, Italy*
- ⁵²*Rutgers University, Piscataway, New Jersey 08855*
- ⁵³*Texas A&M University, College Station, Texas 77843*
- ⁵⁴*Istituto Nazionale di Fisica Nucleare, University of Trieste/ Udine, Italy*
- ⁵⁵*University of Tsukuba, Tsukuba, Ibaraki 305, Japan*
- ⁵⁶*Tufts University, Medford, Massachusetts 02155*
- ⁵⁷*Waseda University, Tokyo 169, Japan*
- ⁵⁸*Wayne State University, Detroit, Michigan 48201*
- ⁵⁹*University of Wisconsin, Madison, Wisconsin 53706*
- ⁶⁰*Yale University, New Haven, Connecticut 06520*

(Dated: September 24, 2018)

We present a measurement of the $t\bar{t}$ production cross section using events with one charged lepton and jets from $p\bar{p}$ collisions at a center-of-mass energy of 1.96 TeV. A b -tagging algorithm based on the probability of displaced tracks coming from the event interaction vertex is applied to identify b quarks from top decay. Using 318 pb⁻¹ of data collected with the CDF II detector, we measure the $t\bar{t}$ production cross section in events with at least one restrictive (tight) b -tagged jet and obtain $8.9_{-1.0}^{+1.0}(\text{stat.})_{-1.0}^{+1.1}(\text{syst.})$ pb. The cross section value assumes a top quark mass of $m_t = 178$ GeV/ c^2 in the acceptance corrections. The dependence of the cross section on m_t is presented in the paper. This result is consistent with other CDF measurements of the $t\bar{t}$ cross section using different samples and analysis techniques, and has similar systematic uncertainties. We have also performed consistency checks by using the b -tagging probability function to vary the signal to background ratio and also using events that have at least two b -tagged jets.

PACS numbers: 14.65.Ha, 13.85.Ni, 13.85.Qk

I. Introduction

The top quark is the most massive fundamental particle observed so far, and the study of its properties is interesting for several reasons ranging from its possible special role in electroweak symmetry breaking to its sensitivity to physics beyond the standard model (SM). In particular, the measurement of the top quark pair production cross section $\sigma_{t\bar{t}}$ is of interest as a test of QCD predictions. Recent QCD calculations done with perturbation theory to next-to-leading order predict $\sigma_{t\bar{t}}$ with an uncertainty of less than 15% [1, 2], which motivate measurements of comparable precision.

Top quark pairs in the SM are produced via either quark-antiquark annihilation or gluon-gluon fusion in hadron colliders. At the Fermilab Tevatron collider, with a center-of-mass energy of 1.96 TeV in $p\bar{p}$ collisions, about 85% of the total top pair production comes from quark-antiquark annihilation. At this center-of-mass energy, the calculated cross section, for the combined Tevatron Run I top mass of 178 GeV/ c^2 [3], is $6.1_{-0.8}^{+0.6}$ pb [1] and decreases by approximately 0.2 pb for each increase of 1 GeV/ c^2 in the value of the top mass over the range 170 GeV/ $c^2 < m_t < 190$ GeV/ c^2 . The standard model top quark decays to a W boson and a b quark almost 100% of the time, resulting in a final state from $t\bar{t}$ production of two W bosons and two b quarks from b quark fragmentation. When one W decays leptonically and the other W decays to quarks, the $t\bar{t}$ event typically contains a high momentum charged lepton, an undetected neutrino and four high transverse momentum jets, two of which originate from b quarks. The undetected neutrino results in an imbalance of the transverse energy of the event, labeled as “missing E_T ” (\cancel{E}_T). This decay mode is called “lepton+jets”.

In this paper, we report a measurement of the cross section for pair production of top quarks in the lepton+jets channel in 318 pb⁻¹ of $p\bar{p}$ collision data at

$\sqrt{s} = 1.96$ TeV. The data were recorded between March 2002 and August 2004, during Run II of the Tevatron, by the CDF II detector, a general purpose detector which combines charged particle trackers, sampling calorimeters, and muon detectors. Processes in which a W boson is produced in association with several jets with large transverse momentum can be misidentified as $t\bar{t}$, since they have the same signature. In order to separate the $t\bar{t}$ events from this background, we develop a method to tag b -jets based on tracking information from the silicon detector. The main event selection requires at least one tight (more restrictive) b tag in the event. As a cross check, we also measure the cross section using events with a loose (less restrictive) b tag and events which have at least two tight or at least two loose b tags. Background contributions from heavy flavor production processes, such as $Wb\bar{b}$, $Wc\bar{c}$ or Wc , misidentified W bosons, electroweak processes, single top production, and mistagged jets are estimated using a combination of Monte Carlo calculations and independent measurements in control data samples. An excess over background in the number of events that contain a lepton, missing energy and three or more jets with at least one b -tag is assumed to be a signal of $t\bar{t}$ production and is used to measure the production cross section $\sigma_{t\bar{t}}$.

Previous measurements [4] at $\sqrt{s} = 1.8$ TeV gave a production cross section consistent with the standard model prediction. Recent CDF measurements at $\sqrt{s} = 1.96$ TeV are reported in Refs. [5–9] and use different techniques and top decay channels. The measurement described here analyzes more data than the above, and uses a jet probability b -tagging algorithm. A feature of this algorithm is that b -tagging is based on a continuous probability function rather than on a discrete object such as a secondary vertex. Potentially, this tagger can also be used to statistically separate b and c heavy flavor contributions.

The organization of this paper is as follows. Section II reviews the detector systems relevant to this

analysis. In Section III, we describe the data sample and event reconstruction. The b -tagging algorithm and its efficiency and misidentification (“fake”) rate are discussed in Section IV. Section V describes the event selection. The estimate of the different backgrounds is presented in Section VI. The $t\bar{t}$ event acceptance and tagging efficiency are derived in Section VII. The $t\bar{t}$ production cross section measurements in single and double tagged events are reported in Sections VIII, and IX, respectively. Finally, the conclusions are presented in Section X.

II. THE CDF II DETECTOR

The CDF II detector uses a cylindrical coordinate system with the z coordinate along the proton direction, the azimuthal angle ϕ , and the polar angle θ usually expressed in terms of the pseudo-rapidity $\eta = -\ln[\tan(\theta/2)]$. The rectangular coordinates x and y point radially outward and vertically upward from the Tevatron ring, respectively. The detector has been described in detail elsewhere [10]. In this section, we give a brief description of the parts relevant for the analysis.

Tracking systems are essential to trigger on and identify high momentum charged particles such as electrons and muons. The charged particle tracking detectors are contained in a superconducting solenoid which generates a magnetic field of 1.4 T, oriented parallel to the proton beam direction. The Central Outer Tracker (COT) [11] is a 3.1 m long open cell drift chamber which performs up to 96 track position measurements in the region between 0.40 m and 1.37 m from the beam axis. Sense wires are arranged in 8 alternating axial and $\pm 2^\circ$ stereo superlayers with 12 wires each. The position resolution of a single drift time measurement is approximately 140 μm . For high momentum tracks, the COT transverse momentum resolution is $\sigma_{p_T}/p_T^2 \approx 0.0017 \text{ GeV}/c$.

Inside the inner radius of the COT, a five layer doubled-sided silicon microstrip detector (SVX) [12] covers the region between 2.5 cm to 11 cm from the beam axis. Three separate SVX barrel modules along the beamline cover a length of 96 cm, approximately 90% of the luminous beam intersection region. Three of the five layers combine an r - ϕ measurement on one side and a 90° stereo measurement on the other, and the remaining two layers combine r - ϕ with a small stereo angle of $\pm 1.2^\circ$. Silicon microstrips have a pitch of 60 to 65 μm depending on the layer. Three additional Intermediate Silicon Layers (ISL) [13] at radii between 19 cm and 30 cm in the central region link tracks in the COT to hits in SVX.

Electromagnetic (EM) and hadronic (HAD) sampling calorimeters [14–16] surround the tracking system and measure the energy flow of interacting particles in the pseudo-rapidity range $|\eta| < 3.64$. The EM and HAD calorimeters are lead-scintillator and iron-scintillator sampling devices, respectively. They are segmented into projective towers, each one covering a small range in pseudo-rapidity and azimuth. Most towers cover 15 degrees in ϕ and 0.10 to 0.13 units in pseudo-rapidity. Proportional chambers (CES) measure the transverse profile of EM showers at a depth corresponding to the shower maximum for electrons. Electrons are reconstructed in the central electromagnetic calorimeter (CEM) with a transverse energy precision $\sigma(E_T)/E_T = 13.5\%/\sqrt{E_T/\text{GeV}} \oplus 2\%$ [14]. Jets are identified as a group of electromagnetic and hadronic calorimeter towers with an energy resolution of approximately $0.1 \cdot E_T + 1.0 \text{ GeV}$ [17].

The muon system is located outside of the calorimeters. Four layers of planar drift chambers (CMU) [18] detect muons with $p_T > 1.4 \text{ GeV}/c$ that penetrate the five absorption lengths of calorimeter steel in the central region of $|\eta| < 0.6$. An additional four layers of planar drift chambers (CMP) [19] located behind 0.6 m of steel outside the magnet return yoke detect muons with $p_T > 2.0 \text{ GeV}/c$. When a track is linked to both CMU and CMP, it is called a CMUP muon. The Central Muon Extension detector (CMX), arranged in a conical geometry, provides muon detection in the region $0.6 < |\eta| < 1.0$ with four to eight layers of drift chambers, depending on the polar angle. All the muon chambers measure the azimuthal coordinates of hits via a drift time measurement. The CMU and CMX also measure the longitudinal coordinate, z .

The beam luminosity is determined by using gas Cherenkov counters [20] located in the region $3.7 < |\eta| < 4.7$ which measure the average number of inelastic $p\bar{p}$ collisions per bunch crossing. The total uncertainty on the luminosity is 5.9%, where 4.4% comes from the acceptance and operation of the luminosity monitor and 4.0% from the calculation of the inelastic $p\bar{p}$ cross section [21].

III. DATA SAMPLE AND EVENT RECONSTRUCTION

The data used in this analysis are from $p\bar{p}$ collisions at a center-of-mass energy of $\sqrt{s} = 1.96 \text{ TeV}$ recorded by the CDF II detector between March 2002 and September 2004. The data sample has been collected by triggers based on the selection of a high transverse momentum lepton (electron or muon). The total in-

tegrated luminosity is 318 pb^{-1} for CEM electron and CMUP muon candidates, and 305 pb^{-1} for CMX muon candidates. Briefly, we discuss the trigger and lepton identification requirements, the reconstruction of jets, and the missing transverse energy, \cancel{E}_T .

CDF has a three-level trigger system to filter events from a 2.5 MHz beam crossing rate down to 60 Hz for permanent storage. The first two levels of triggers are special purpose hardware and the third consists of a farm of computers.

The first trigger level (L1) reconstructs charged particle tracks in the COT r - ϕ projection using a hardware track processor called the Extremely Fast Tracker (XFT) [22]. The L1 electron trigger requires a XFT track with $p_T > 8 \text{ GeV}/c$ matched to an EM calorimeter tower with $E_T > 8 \text{ GeV}$ and with a ratio of hadronic-to-electromagnetic energy less than 0.125. The L1 muon trigger requires an XFT track with $p_T > 4 \text{ GeV}/c$ matched to a muon track segment with $p_T > 6 \text{ GeV}/c$ from the CMU and CMP chambers or a track with $p_T > 8 \text{ GeV}/c$ matched to a muon track segment with $p_T > 6 \text{ GeV}/c$ in the CMX chambers.

The second level (L2) electron trigger requires the XFT track found at L1 to be matched to a cluster of energy in the central EM calorimeter with $E_T > 16 \text{ GeV}$. The cluster adds the energy of the neighboring trigger towers with $E_T > 7.5 \text{ GeV}$ to the original L1 trigger tower. A trigger tower consists of two calorimeter towers. The L2 muon trigger accepts events passing L1.

The third trigger level (L3) is a farm of Linux computers which perform on-line event reconstruction, including 3D charged particle reconstruction. The L3 electron trigger requires a track with $p_T > 9 \text{ GeV}/c$ matched to an energy cluster of three adjacent towers in pseudo-rapidity in the central EM calorimeter with $E_T > 18 \text{ GeV}$, consistent with the shower profile expected from test beam electrons. The L3 muon trigger requires a track with $p_T > 18 \text{ GeV}/c$ matched to a track segment in the muon chambers within 10 cm in the $r - \phi$ view and, for CMU and CMX muons only, within 20 cm in the z view. The efficiency of these triggers is measured using $W^\pm \rightarrow e^\pm \nu$ and $Z \rightarrow \mu^+ \mu^-$ data (the method is described in Ref. [23]) and is found to be $(96.2 \pm 0.6)\%$ for CEM electrons, and $(90.8 \pm 0.5)\%$ and $(96.5 \pm 0.4)\%$ for CMUP and CMX muons respectively, for electrons and muons passing through the fiducial volume of these detectors.

A. Track and Primary Vertex Reconstruction

The trajectories of charged particles are found (in a first approximation) as a series of segments in the axial superlayers of the COT. Two complementary algorithms associate the segments lying on a common circle to define an axial track. Segments in the stereo layers are associated with the axial tracks to reconstruct 3D tracks. For muons and electrons used in this analysis, COT tracks are required to have at least 3 axial and 2 stereo segments with at least 5 hits per superlayer. The efficiency for finding isolated high momentum COT tracks in the COT fiducial volume with $p_T > 10 \text{ GeV}/c$ is measured using electrons from $W^\pm \rightarrow e^\pm \nu$ events and is found to be $(98.3 \pm 0.1)\%$. Silicon hit information is added to reconstructed COT tracks using an “outside-in” tracking algorithm. The COT tracks are extrapolated to the silicon detector and the track is refit using the information from the silicon measurements. The initial track parameters provide a width for a search region in a given layer. For each candidate hit in that layer, the track is refit and used to define the search region into the next layer. The search uses the two best candidate hits in each layer to generate a small tree of final track candidates, and the one with the best fit χ^2 is selected. The efficiency to associate at least three silicon hits with an isolated COT track is found to be $(91 \pm 1)\%$.

The primary vertex location for a given event is found by fitting well-measured tracks to a common point of origin. At high luminosities, more than one collision can occur on a given bunch crossing. For a luminosity of $\sim 10^{32} \text{ cm}^{-2} \text{ s}^{-1}$, there are ~ 2.3 interactions per bunch crossing. The luminous region is long, with $\sigma_z = 29 \text{ cm}$; therefore the primary vertices of each collision are typically separate in z . The first estimate of the primary vertices (x_V, y_V, z_V) is binned in the z coordinate, and the z position of each vertex is then calculated from the weighted average of the z coordinate of all tracks within 1 cm of the first iteration vertex, with a typical resolution of $100 \mu\text{m}$. The primary vertex is determined event by event by an iterative algorithm which uses tracks around a seed vertex, defined as above, to form a new vertex. The χ^2 for all tracks relative to the new vertex is calculated, tracks with bad χ^2 are removed, and the cycle is repeated until all tracks have a good χ^2 . The locus of all primary vertices defines the beamline, the position of the luminous region of the beam-beam collisions through the detector. A linear fit to (x_V, y_V) vs. z_V yields the beamline for each stable running period. The beamline is used as a constraint to refine the knowledge of the primary vertex in a given

event. The transverse beam cross section is circular, with a rms width of $\approx 30 \mu\text{m}$ at $z = 0$, rising to $\approx 50 - 60 \mu\text{m}$ at $|z| = 40 \text{ cm}$. The beam is not necessarily parallel nor centered in the detector.

B. Electron Identification

Electron reconstruction begins with a track with $p_T > 9 \text{ GeV}/c$ that extrapolates to a cluster of three CEM towers adjacent in pseudo-rapidity with a total $E_T > 20 \text{ GeV}$. Several cuts are successively applied in order to improve the purity of the electron selection, as summarized in Table I. Electron candidates passing these requirements are called tight electrons.

The ratios between the hadronic and the electromagnetic cluster energies E_{HAD}/E_{EM} and between the cluster energy and the track momentum E/p are required to be consistent with an electron's energy deposition in the calorimeters. The cluster is further required to be isolated, the isolation I being defined as the ratio of the additional transverse energy in a cone of radius $R = \sqrt{(\Delta\phi)^2 + (\Delta\eta)^2} = 0.4$ around the cluster to the transverse energy of the cluster itself.

The position of the electromagnetic shower measured by the CES detector is used to define matching requirements between the extrapolated track and the cluster in the CES x and z local coordinates. In particular, a charge dependent cut in the x position is applied to take into account the different flow of energy deposited by bremsstrahlung photons emitted by an electron or a positron. In addition, the CES provides electron identification through the observed shower shape. The CES shower shape is fitted in the z view to the distribution expected for an electron, and the chisquare probability for the fit, χ_{strip}^2 , is used as a cut on the shower profile. Finally, the sharing of energy between adjacent calorimeter towers is quantified by the lateral shower profile L_{shr} , which measures how close the energy distribution in the CEM towers adjacent to the cluster seed is to the electron hypothesis.

Electrons from photon conversions throughout the detector material are vetoed by rejecting electron candidates if an oppositely charged track with a small distance of closest approach (D) is found. This analysis is sensitive to any loss in efficiency from the misidentification of an electron from the W boson decay as a photon conversion. Therefore, in order to avoid loss of efficiency, the veto is not applied to events consistent with electrons radiating a photon that subsequently converts. The performance of this algorithm to identify electrons from photon conver-

sions is estimated to be $(72.6 \pm 0.1)\%$ [9], where the uncertainty covers both statistical and systematic.

The efficiency of the electron selection on $t\bar{t}$ events is determined by means of Monte Carlo simulation. Studies of $Z \rightarrow e^+e^-$ processes show that a data to Monte Carlo simulation scale factor of $(99.6^{+0.4}_{-0.5})\%$ is needed to correct the simulation predictions for the efficiency for CEM electron identification.

Other electron categories are defined. Candidate electrons passing all the above requirements except for the isolation cut are called loose electrons. Tracks matched to an energy deposit in the plug calorimeter ($1.2 < |\eta| < 2.0$) are called plug electrons.

C. Muon Identification

Muon identification starts by requiring an isolated, high momentum COT track that extrapolates to a track segment in the muon chambers. Several additional requirements are imposed in order to minimize contamination from hadrons punching through the calorimeter, decays in flight of charged hadrons and cosmic rays. Table II lists the selection requirements for candidate muons. Muon candidates passing these cuts are called tight muons.

The COT track must have $p_T \geq 20 \text{ GeV}/c$, and at least 3 axial and 2 stereo segments with a minimum of 5 hits per segment. The distance of closest approach of the track to the beamline in the transverse plane, d_0 , must be small in order to select prompt muons (coming from the interaction primary vertex) and reject cosmics and in-flight decays. The energy deposition in the EM and HAD calorimeters, E_{EM} and E_{HAD} , must be small as expected for the passage of a minimum ionizing particle. The distance between the extrapolated COT track and the track segment in the muon chambers, Δx , must be small in order to ensure a good match. If a track is matched to a CMU segment, a matching CMP segment is also required, and vice versa. Isolation is defined as the ratio between any additional transverse energy in a cone of radius $R = 0.4$ around the track direction and the muon p_T , and it is required to be smaller than 0.1. Cosmic rays are efficiently identified and rejected through their asynchronous track timing relative to the beam crossing time and their incoming and outgoing back-to-back track topology.

Studies of $Z \rightarrow \mu^+\mu^-$ processes show that a data to Monte Carlo simulation scale factor of $(87.4 \pm 0.9)\%$ ($(98.9 \pm 0.6)\%$) is needed to correct the simulation predictions for the CMUP (CMX) muon identification efficiency.

As for the electrons, candidate muons passing all

TABLE I: Selection requirements for tight electrons.

Electron Variable	Cut
p_T	≥ 10 GeV/c
E_T	≥ 20 GeV
COT Axial Segments	≥ 3
COT Stereo Segments	≥ 2
Hits for Each COT Segment	≥ 5
E_{HAD}/E_{EM}	$\leq 0.055 + 0.00045 \times E$
E/p	≤ 2.0 unless $p_T \geq 50$ GeV/c
Isolation	≤ 0.1
L_{shr}	≤ 0.2
CES $ \Delta z $	≤ 3.0 cm
CES $Q \times \Delta x $	$-3.0 \leq Q \times \Delta x \leq 1.5$ cm
CES χ_{strip}^2	≤ 10
Photon Conversions	Veto if $D \leq 0.2$ cm and $\Delta \cot(\theta) < 0.04$

TABLE II: Selection requirements for tight muons.

Muon Variable	Cut
p_T	≥ 20 GeV/c
COT Axial Segments	≥ 3
COT Stereo Segments	≥ 2
Hits for Each COT Segment	≥ 5
$ d_0 $	≤ 0.2 cm if no silicon hits
$ d_0 $	≤ 0.02 cm if silicon hits
E_{HAD}	$\leq \max(6, 6 + 0.0280(p - 100))$ GeV
E_{EM}	$\leq \max(2, 2 + 0.0115(p - 100))$ GeV
CMU $ \Delta x $	≤ 3.0 cm
CMP $ \Delta x $	≤ 5.0 cm
CMX $ \Delta x $	≤ 6.0 cm
Isolation	≤ 0.1
Cosmic Rays	Veto

the cuts except the isolation cut are called loose muons. A track matched to a CMU or a CMP segment only, which passes all the other cuts including isolation, is also accepted as a loose muon.

D. Jet Reconstruction and Corrections

The jets used in this analysis are reconstructed from calorimeter towers using a cone algorithm [24] with a radius $R \leq 0.4$, for which the E_T of each tower is calculated with respect to the z coordinate of the event. The calorimeter towers belonging to any electron candidate are not used by the jet clustering algorithm. The energy of the jets is corrected [25]

for the pseudo-rapidity dependence of the calorimeter response, the calorimeter time dependence, and extra E_T from any multiple interactions.

By definition, tight jets have corrected $E_T \geq 15$ GeV and detector $|\eta| < 2.0$, whereas loose jets have corrected $E_T \geq 8$ GeV and detector $|\eta| < 2.0$. Detector η is the pseudo-rapidity of the jet calculated with respect to the center of the detector.

E. Missing Transverse Energy Reconstruction

The presence of neutrinos in an event is inferred by an imbalance of transverse energy in the detector. The missing transverse energy, \cancel{E}_T , is defined as the

magnitude of $-\sum_i[E_{T,i}\cos(\phi_i), E_{T,i}\sin(\phi_i)]$, where $E_{T,i}$ is the transverse energy of the calorimeter tower i calculated with respect to the z coordinate of the event, ϕ_i is its azimuthal angle, and the sum is over all calorimeter towers. The \cancel{E}_T is corrected by subtracting the transverse momentum of the muon track and adding back the transverse energy in the calorimeter towers traversed by the muon. Because the \cancel{E}_T calculation uses all calorimeter towers, the \cancel{E}_T vector is adjusted for the effect of the jet corrections for all jets with $E_T \geq 8$ GeV and $|\eta| < 2.5$.

F. Monte Carlo Samples and Detector Simulation

The understanding of acceptances, efficiencies and backgrounds relies on detailed simulation of physics processes and detector response.

The detector acceptance for $t\bar{t}$ events is modeled using PYTHIA v6.2 [26] and HERWIG v6.4 [27]. This analysis uses the former for the final cross section estimate and the latter to estimate the systematics due to differences in the modeling of $t\bar{t}$ production and decay. These generators employ leading order matrix elements for the hard parton scattering, followed by parton showering to simulate gluon radiation and fragmentation effects. The generators are used with the CTEQ5L parton distribution functions [28]. Decays of b and c hadrons are modeled using QQ v9.1 [29]. Estimates of backgrounds from W bosons produced in association with jets are derived using the ALPGEN generator [30] with parton showering provided by HERWIG. The background from electroweak processes and single top production is studied using PYTHIA.

The CDF II detector simulation reproduces the response of the detector and uses the same detector geometry database as the event reconstruction. Particle interactions through matter are performed with GEANT3 [31]. Charge deposition in the silicon detectors is calculated using a simple geometrical model based on the path length of the ionizing particle and an unrestricted Landau distribution. The drift model for the COT uses a parametrization of a GARFIELD [32] simulation with parameters tuned to match COT collider data [11]. The calorimeter simulation uses the GFLASH [33] parametrization package interfaced with GEANT3. The GFLASH parameters are tuned to test beam data for electrons and high- p_T pions and they are checked by comparing the calorimeter energy of isolated tracks in collision data to their momentum as measured in the COT. More details on the CDF II simulation can be found in Ref. [34].

IV. JET PROBABILITY b -TAGGING ALGORITHM

The jet probability b -tagging algorithm [35] is used to determine whether a jet has been produced from the hadronization process of a light parton or a heavy parton. The latter result in long-lived hadrons whose decay gives rise to tracks displaced from the primary interaction vertex. This algorithm uses tracks associated with a jet to determine the probability for these to come from the primary vertex of the interaction. The calculation of the probability is based on the impact parameters (d_0) of the tracks in the jet and their uncertainties. The impact parameter is assigned a positive or negative sign depending on the position of the track's point of closest approach to the primary vertex with respect to the jet direction, as shown in Fig. 1. By construction, the probability for tracks originating from the primary vertex is uniformly distributed from 0 to 1. For a jet coming from heavy flavor hadronization, the distribution peaks at 0, due to tracks from long lived particles that have a large impact parameter with respect to the primary vertex.

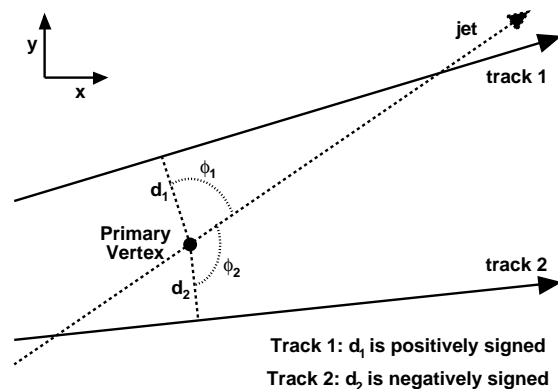


FIG. 1: The sign of the impact parameter of a track. The impact parameter is positive (negative) if the angle ϕ between the jet axis and the line connecting the primary vertex and the track's point of closest approach to the primary vertex itself is smaller (bigger) than $\pi/2$.

The particles in a jet coming from a light parton originate at the primary vertex, but these tracks are reconstructed with a non-zero impact parameter due to the finite tracking resolution. They have an equal probability of being positively or negatively signed. Jets which originate from a heavy parton contain long lived hadrons giving rise to tracks displaced in the jet direction, which preferentially populate the positive side of the signed impact parameter distribution. The

width of the negative impact parameter distribution is solely due to the tracking detector resolution, beam spot size, and multiple scattering.

The tracking resolution can be extracted from the data by fitting the negative side of the signed impact parameter distribution of tracks from prompt jets, which are the dominant component of inclusive jet data. Tracks are divided into 72 different categories according to the number and quality of SVX hits, detector η and p_T . To minimize the contribution from badly measured tracks with a large reconstructed impact parameter, the signed impact parameter significance, S_{d_0} (ratio of the impact parameter to its uncertainty), is parameterized for each track category. Tracks are fitted to a helix, and the impact parameter is corrected for beam offsets in order to take into account any displacement of the primary vertex from the nominal position. The uncertainty in the impact parameter is given by the error propagation of the uncertainties in the fit and in the beam offset correction. We parameterize the impact parameter significance for tracks satisfying the quality criteria listed in Table III that are associated with jets with $E_T > 7$ GeV and $|\eta| < 2.5$. These tracks must have $p_T > 0.5$ GeV/c, impact parameter less than 0.1 cm (in order to reject long lived K 's and Λ 's), three to five hits on different axial layers of the SVX, at least 20 (17) hits in the COT axial (stereo) layers, and the z position of the track must be within 5 cm of the event primary vertex. Tracks passing this selection are called jet probability tracks. The $|d_0|$ is measured with respect to the primary vertex. The event is required to have a primary vertex, and the vertex with highest sum of transverse momentum of all tracks is chosen in events which have more than one vertex.

TABLE III: Selection criteria for tracks used by the jet probability algorithm.

Variable	Cut
p_T	> 0.5 GeV/c
$ d_0 $	< 0.1 cm
$N_{\text{SVX axial}}$	≥ 3 and ≤ 5
$N_{\text{COT axial}}$	≥ 20
$N_{\text{COT stereo}}$	≥ 17
$ z_{\text{trk}} - z_{\text{pv}} $	< 5 cm

Figure 2 shows the distribution of the impact parameter significance of tracks in an inclusive jet sample for one of the track categories, namely tracks with at least 5 good SVX hits, $p_T > 5$ GeV/c and $|\eta| < 0.6$. The negative side of this distribution is fitted with a function $R(S)$ called the resolution function, which is used to determine the probability, $P_{tr}(S_{d_0})$, that the

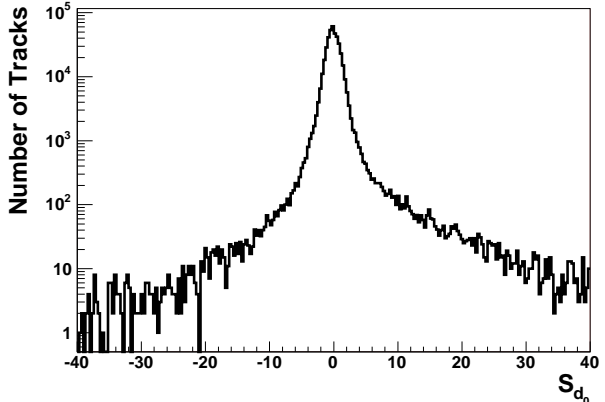


FIG. 2: Distribution of the impact parameter significance for tracks in an inclusive jet sample with at least 5 good SVX hits, $p_T > 5$ GeV/c, and $|\eta| < 0.6$.

impact parameter significance of a given track is due to the detector resolution, defined as:

$$P_{tr}(S_{d_0}) = \frac{\int_{-\infty}^{-|S_{d_0}|} R(S) dS}{\int_{-\infty}^0 R(S) dS}. \quad (1)$$

The S_{d_0} distribution peaks at zero and falls quickly with increasing absolute value of $|S_{d_0}|$, but the tails are rather long. In order to improve the statistics and obtain a better fit in the tail, we use non-linear bins by transforming it to $X = \ln(|S_{d_0}^-|)$, where the minus sign indicates that only the negative part of S_{d_0} is used. Figure 3 shows the result of such a fit, together with the fit residues defined as (data-fit)/uncertainty, where the uncertainty is taken as the statistical uncertainty on each data point. A resolution function parameterized as the convolution of four Gaussians with means at zero is found to fit well all distributions for all 72 track categories:

$$R(S) = \sum_{i=1}^4 \frac{p_i}{\sqrt{2\pi}\sigma_i} e^{-S^2/2\sigma_i^2}. \quad (2)$$

After the transformation to a logarithmic axis, the resolution function becomes

$$R(X) = \sum_{i=1}^4 \frac{p_i}{\sqrt{2\pi}\sigma_i} e^{(X - \frac{e^{2X}}{2\sigma_i^2})} \quad (3)$$

and $R(X)$ is used to fit the transformed $X = \ln(|S_{d_0}^-|)$ distribution.

The jet probability P_J that a jet is consistent with

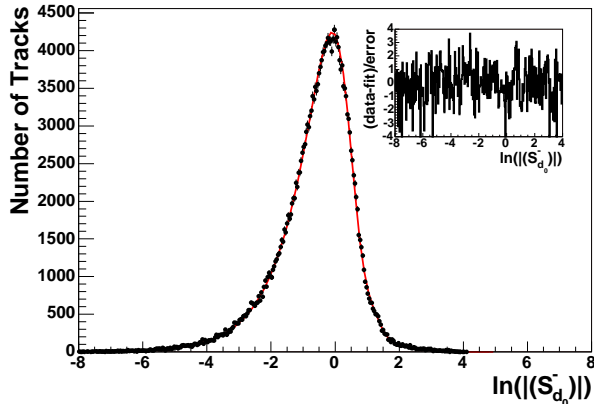


FIG. 3: Fit to the transformed impact parameter significance, $\ln(|S_{d_0}^-|)$, where only the negative side of the S_{d_0} distribution is used. The resolution function is chosen as the convolution of four Gaussians. The inset shows the residues of the fit, $(\text{data-fit})/\text{uncertainty}$.

a zero lifetime hypothesis is defined as

$$P_J = \prod \times \sum_{k=0}^{N_{trk}-1} \frac{(-\ln \prod)^k}{k!}, \quad (4)$$

where

$$\prod = \prod_{l=1}^{N_{trk}} P_{tr} \quad (5)$$

and N_{trk} is the number of jet probability tracks with positive impact parameter. Jets are required to have at least two jet probability tracks with positive impact parameter to be taggable. Both of these distributions should be uniformly distributed in the interval [0-1] for jets having only prompt tracks. Tracks with negative impact parameter are used to define a negative P_J , which is used to check the algorithm and to estimate the misidentification rate. We define positive (negative) tagged jets as those jets whose positive (negative) P_J is less than a cutoff, where we use 1% (main result) and 5% (cross check). Positive tagged jets are expected to be enriched in heavy flavor. The 1% cut was used in previous publications [35] and has similar performance to the secondary vertex tagger [7], while the loose (less restrictive) 5% cut was chosen near the point where the P_J distribution becomes flat (see Fig. 12). Further gain in $t\bar{t}$ selection efficiency resulting from a looser P_J cut is accompanied by an increase in background from light jets misidentified as heavy flavor (mistags). For compar-

ison, both the 1% and 5% numbers and figures are presented together throughout the paper.

A feature of this algorithm is that the b -tagging is performed using a continuous variable instead of a discrete object like a reconstructed secondary vertex. It therefore provides a variable that allows one to move continuously along the efficiency curve and to select the optimal signal to background point for a specific analysis. Furthermore, the ability to adjust the P_J cut is a valuable tool to understand the heavy flavor content of the sample. Potentially [35], this method can be used to statistically separate b and c heavy flavor contributions. This feature is illustrated in the left plot in Fig. 4, where the jet probability distributions for b , c and light jets are shown. Monte Carlo simulated $2 \rightarrow 2$ parton events are used as described in Section IV A. In the right plot, we show the jet probability distributions observed in two different data sets of jets. The first sample is enriched in heavy flavor content by requiring the jets to contain a soft momentum electron; here, events are triggered on low p_T inclusive electrons (see Section IV A). The second set consists of generic QCD jets selected by requiring events with at least one jet with $E_T > 50$ GeV (the Jet50 sample).

In this section we discuss the b -tagging algorithm itself, independently of the other details of this analysis.

A. Measurement of the Tagging Efficiency for Heavy Quark Jets

The method used to measure the jet probability tagging efficiency for heavy flavor jets is described in detail in Ref. [7]. The ideal events to study this efficiency are $b\bar{b}$ dijet events. We use a calibration data sample of jets whose heavy flavor fraction can be measured: a sample triggered on low p_T inclusive electrons which is enriched in semileptonic decays of bottom and charm hadrons. The tagging efficiency is also measured for simulated jets by using a Monte Carlo sample similar to the calibration sample. We use HERWIG to generate $2 \rightarrow 2$ parton events, which are passed through a filter requiring an electron with $p_T > 7$ GeV/c and $|\eta| < 1.3$. Events passing this filter are processed using the detector simulation described in Section III F. Electrons are identified using a selection similar to that described in Section III B, except that they are required to be non-isolated and have a lower energy threshold ($E_T > 9$ GeV and track $p_T > 8$ GeV/c). The heavy flavor content of the sample is further enhanced by requiring two jets in the event, an “electron jet”, presumed to contain the de-

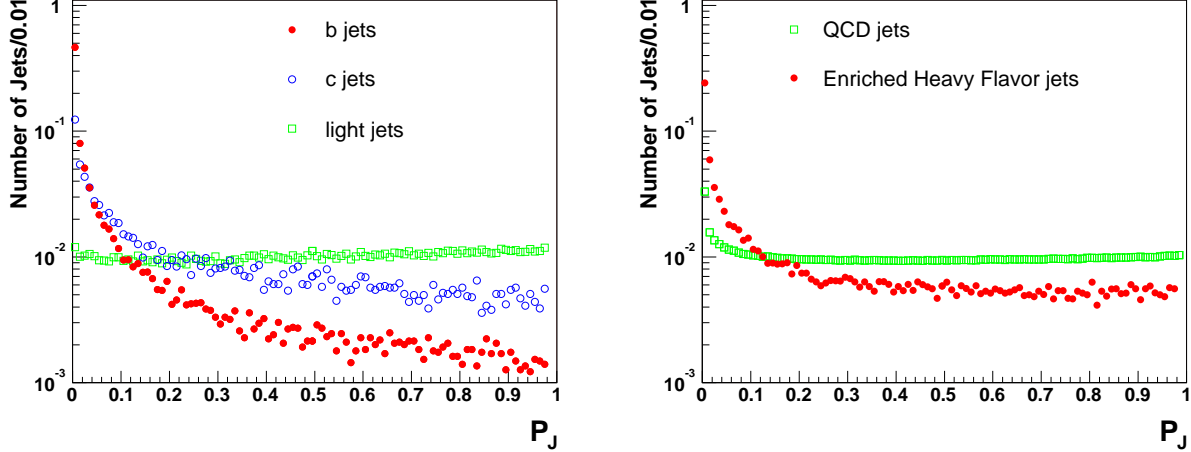


FIG. 4: Left: jet probability distributions for jets matched to b (full circles), c (empty circles) and light (empty squares) quarks in Monte Carlo simulated events. Right: jet probability distributions for electron jets in inclusive electron data (full circles) and for generic QCD jets in Jet50 data (empty squares).

cay products of a heavy flavor hadron, and an “away jet”. The electron jet must have $E_T > 15$ GeV and be within 0.4 of the electron direction in η - ϕ space. The away jet is required to have $E_T > 15$ GeV and $|\eta| < 1.5$, and it must be approximately back-to-back with the electron jet ($\Delta\phi_{e-j} > 2$ rad). If the fraction of electron jets containing heavy flavor for which the away jet is tagged (F_{HF}^a) is known, and if there were no prompt jets misidentified as b -jets, the efficiency to tag a heavy flavor jet containing an electron would be given by

$$\epsilon = \frac{N_{a+}^{e+}}{N_{a+}} \cdot \frac{1}{F_{HF}^a}, \quad (6)$$

where N_{a+}^{e+} is the number of events for which both the electron jet and the away jet are positively tagged, and N_{a+} is the total number of events for which the away jet is positively tagged. Since light jets can be tagged as well, we correct for this effect by subtracting the number of negative tags. We define the positive tag excess for events with a positive or negative tag in the away jet as

$$\Delta_{a+} = N_{a+}^{e+} - N_{a+}^{e-} \quad (7)$$

$$\Delta_{a-} = N_{a-}^{e+} - N_{a-}^{e-} \quad (8)$$

where, for example, N_{a+}^{e-} is the number of events where the electron jet is negatively tagged and the away jet is positively tagged. The tagging efficiency for heavy flavor jets containing an electron is then

given by

$$\epsilon = \frac{\Delta_{a+} - \Delta_{a-}}{(N_{a+} - N_{a-})} \cdot \frac{1}{F_{HF}^a}. \quad (9)$$

Since events with an electron jet and a tagged away jet are mostly due to heavy flavor pair production, one expects F_{HF}^a to be close to unity. This number is less than 1.0 due to events in which the away jet is mistagged or contains heavy flavor due to gluon splitting or flavor excitation, and the electron is either a jet misidentified as electron or part of a photon conversion pair. If P denotes the probability to positively tag the away jet in an event where the electron jet is a light jet, then F_{HF}^a is given by

$$F_{HF}^a = 1 - P(1 - F_{HF}), \quad (10)$$

where $F_{HF} = F_b + F_c = F_b \cdot (1 + F_{c/b})$ denotes the total heavy flavor fraction of electron jets. Here F_b and F_c are the total b and c fractions of electron jets, respectively, and $F_{c/b}$ is the c to b fraction ratio. We estimate P using identified conversions as

$$P = \frac{\frac{N_c^{a+} - N_c^{a-}}{N_{a+} - N_{a-}} - \epsilon'_c}{\frac{N_c}{N} - \epsilon'_c}, \quad (11)$$

where N is the number of events passing the selection, $\epsilon'_c = \frac{N_c^{e+} - N_c^{e-}}{N_{e+} - N_{e-}}$, and the c subscript refers to events where the electron was identified as a conversion. A full derivation of this expression can be

found in Ref. [7]. Two methods are used to measure the b -fraction, F_b , of the electron jets. The first method is to reconstruct $D^0 \rightarrow K^- \pi^+$ decays within the electron jet and use the invariant mass sidebands to subtract background. The second method involves searching for secondary muons within the electron jet resulting from cascade $b \rightarrow c \rightarrow l\nu q$ decays using the same-sign rate to estimate the background. The contribution from charm, $F_{c/b}$, is determined from Monte Carlo simulation to be $F_{c/b} = 0.61 \pm 0.10$. For inclusive electron data we measure $F_{HF} = 0.259 \pm 0.064$ and $F_{HF}^a = 0.71 \pm 0.05$.

The efficiencies to tag a taggable heavy flavor jet with $E_T > 15$ GeV in data are summarized in Table IV for $P_J < 1\%$ and 5% . The ratio of data efficiency to Monte Carlo simulation efficiency is called the tagging scale factor (SF). The uncertainties shown are statistical and systematic, which are described below.

TABLE IV: Efficiency to tag a taggable heavy flavor electron jet in data and the tagging scale factor (SF) for jet probability cuts of 1% and 5%.

	$P_J < 1\%$	$P_J < 5\%$
ϵ (Data)	0.258 ± 0.011	0.334 ± 0.016
SF	0.817 ± 0.07	0.852 ± 0.072

It is crucial to understand the tagging efficiency and scale factor dependences on the jet E_T in order to characterize the jet probability algorithm performance. The E_T dependence observed in the inclusive electron sample is shown in Fig. 5 and 6 for the tagging efficiency and scale factor respectively. Due to the lack of statistics at high jet E_T , we repeat the study using two samples of high energy jets selected by requiring events with at least one jet with $E_T > 20$ GeV (the Jet20 sample) or with $E_T > 50$ GeV (the Jet50 sample). The absolute value of the SF can not be extracted because of the unknown content of heavy flavor in these samples. However, since the variations of heavy flavor fraction are relatively small over a large range of E_T , we can still estimate the E_T dependence of the scale factor from the E_T dependence of the ratio of positive tag excess between data and Monte Carlo simulation. Table V shows the results of a linear fit of the tagging scale factor to the jet E_T in the inclusive electron, Jet20 and Jet50 samples. The combined estimate of the slopes is found to be consistent with a flat E_T dependence of the scale factor both when a P_J cut of 1% and 5% is applied. Based on these results, we conclude that the scale factor measured in the inclusive electron sample is valid at any E_T .

Different sources of systematic uncertainty in the determination of SF have been considered. An uncertainty on the value of F_b , determined from the rate of $D^0 \rightarrow K\pi$ decays, comes from the branching ratio $BR(B \rightarrow l\nu D^0 X)$. A factor 1.131 ± 0.070 is used to normalize the Monte Carlo simulation prediction to the PDG [36] value. The uncertainty includes both the PDG branching ratio uncertainty and the Monte Carlo simulation statistical error. Another uncertainty on F_b comes from the difference in D^0 reconstruction efficiency, ϵ_{D^0} , between data and Monte Carlo simulation. This uncertainty is derived by studying the efficiency of reconstruction for simulated $D^0 \rightarrow K\pi$ decays embedded into data events, and is found to be 10%. There is an additional uncertainty due to the assumption of symmetry between negative tags and positive mistags implicit in the derivation of Equation 9. The effect of a mistag asymmetry is estimated by scaling the subtracted negative tags by different factors ranging from 0 to 2 (0.4 to 1.4) for 1% (5%) jet probability cuts, and an uncertainty of 7% is conservatively derived on the tagging scale factor due to this effect. Final estimates for jet probability tagging efficiencies and scale factors are summarized in Table IV.

We do not measure the tagging scale factor for c jets. We assume a common scale factor for jets from b and c quarks and we increase the uncertainty for a c quark scale factor by 100% to take into account additional uncertainties due to this assumption.

B. Measurement of the Mistag Rate

An important ingredient of any analysis which uses heavy flavor tagging is the background from light quark or gluon jets incorrectly tagged as heavy flavor. The probability of (positively) tagging a light jet (the “mistag rate”) is closely related to the negative tag rate. We remind the reader that a positive (negative) P_J is calculated using positively (negatively) signed impact parameter tracks, and a jet which has positive (negative) P_J smaller than a certain cut is said to be positively (negatively) tagged. It is assumed that the negative tags are due to detector resolution effects only, while the positive tag rate has an additional contribution from real heavy flavor in the jets. Under this assumption, the mistag rate is equal to the negative tag rate, although in reality there is also a small contribution from heavy flavor jets to the negative tag rate and there are contributions from K ’s, Λ ’s and nuclear interactions with the detector material to the positive tag rate. These effects are considered later in Section IV B 1.

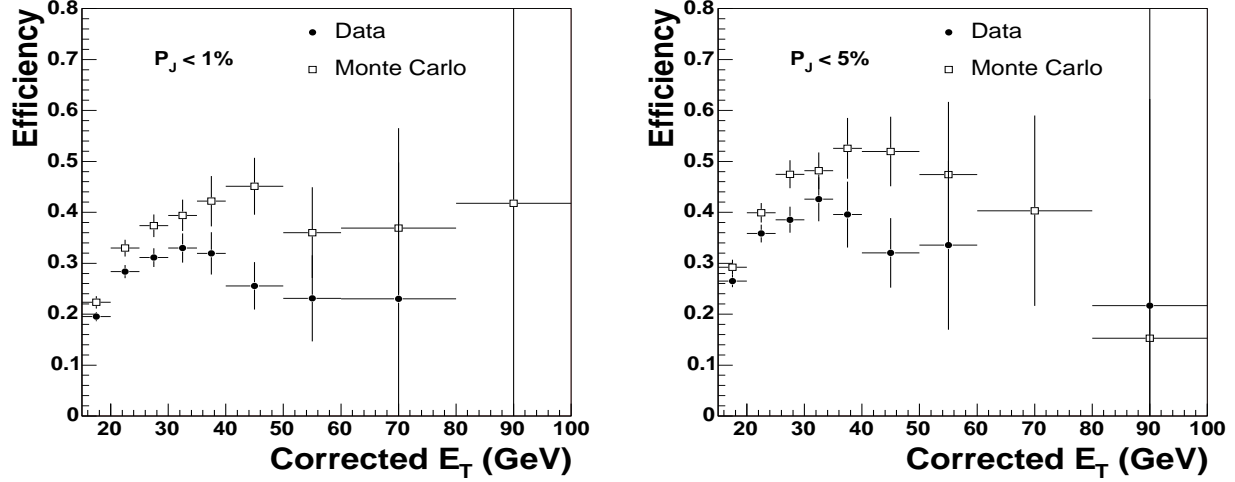


FIG. 5: Efficiency to tag a heavy flavor jet as a function of corrected jet E_T in data and Monte Carlo simulation for 1% (left) and 5% (right) jet probability cut values.

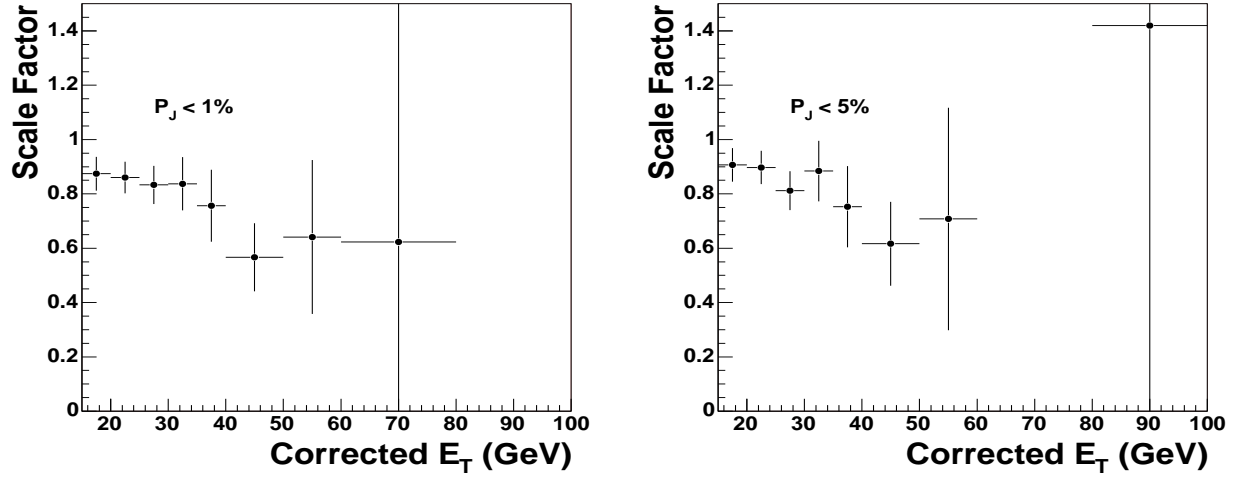


FIG. 6: The scale factor (SF) as a function of corrected jet E_T for 1% (left) and 5% (right) jet probability cut values.

TABLE V: Summary of the scale factor *vs.* E_T slope measurements in various samples.

Sample	$P_J < 1\%$	$P_J < 5\%$
Inclusive Electron	-0.0082 ± 0.0037	-0.0081 ± 0.0044
Jet 20	-0.0008 ± 0.0019	-0.0028 ± 0.0024
Jet 50	0.0005 ± 0.0008	0.0005 ± 0.0009
Weighted Average	-0.00002 ± 0.00070	-0.00020 ± 0.00072

Since the tag rate has a considerable dependence on jet kinematics, it is parameterized as a 6 dimensional

tag rate matrix, or look-up table, of the transverse energy E_T of the jet, the number of jet probability

tracks in the jet N_{trk} , the sum of the transverse energy of all jets in the event $\sum E_T^{jet}$, the η of the jet computed with respect to the center of the detector, the z vertex position z_{vtx} and the ϕ of the jet. The tag rates are obtained from four inclusive jet samples selected by requiring the E_T of the most energetic jet in the event to be greater than 20, 50, 70 or 100 GeV respectively. For a 1% (5%) P_J cut, the overall negative tag rate is $(1.22 \pm 0.08)\%$ ($(5.30 \pm 0.25)\%$), while the overall positive tag rate is $(3.54 \pm 0.18)\%$ ($(9.20 \pm 0.26)\%$). Overall tag rates depend on the sample, which is why the tag rates are parameterized as a function of different variables. Figure 7 shows the negative tag rates for $P_J < 1\%$ and $P_J < 5\%$ as a function of the jet E_T and pseudo-rapidity. The bands represent the total uncertainty.

We estimate the systematic uncertainties by comparing the observed and predicted tag rates in different data samples. We apply tag rate matrices, constructed using different inclusive jet subsamples, to different datasets. Results are shown in Table VI for a P_J cut of 1%. The largest deviation between observed and predicted tag rates across the different jet samples is taken as the systematic uncertainty due to the sample dependence of the matrix. In order to account for any possible bias due to the trigger selection, we apply the matrix separately to trigger and non-trigger jets. A trigger jet is defined as the jet closest in η - ϕ space to the level 2 cluster that fired the trigger. We also apply a matrix built with a high statistics sample of Jet20 events, to the Jet50 sample which has several jets below the trigger threshold of 50 GeV. Also considered is a sample selected by requiring at least four jets with $E_T > 15$ GeV and $\sum E_T^{jet} > 125$ GeV. These events are expected to give a reasonable estimate of the systematic uncertainty because of the higher jet and track multiplicities. Furthermore, this sample is not used to build the matrix, making it sensitive to any additional sources of systematic uncertainty. Figure 8 compares the observed and predicted tag rates in the $\sum E_T^{jet}$ sample as a function of jet E_T . The total systematic uncertainty on the overall tag rates is conservatively taken as the sum in quadrature of the $\sum E_T^{jet}$, Jet20 to Jet50, and the largest of the trigger and sample contributions. Table VII summarizes the relative uncertainties on the overall tag rates for P_J cuts of 1% and 5%. The total relative uncertainty is 5.0% (2.8%) for positive tag rate and 6.7% (4.7%) for negative tag rate for a P_J cut of 1% (5%).

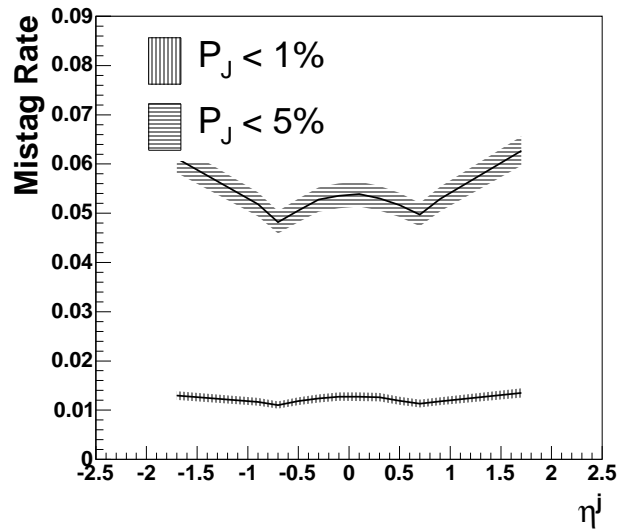
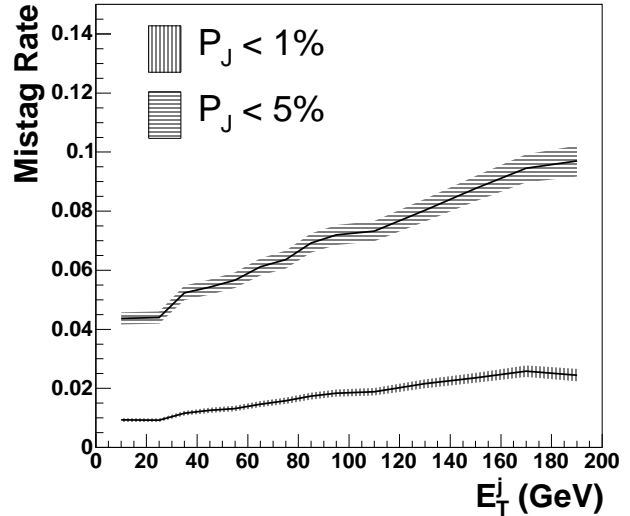


FIG. 7: Mistag rate for jet probability cuts of 1% and 5% as a function of jet E_T (top) and jet pseudo-rapidity (bottom) in inclusive jet data sample. The bands represent the statistical and systematic uncertainties added in quadrature.

1. Mistag Asymmetry

The rate of negatively tagged jets does not reflect the rate of positive mistags of light jets because of residual lifetime effects from Λ 's and K 's or interactions with the detector material. Corrections for these effects are determined by studying the flavor composition of tagged jets in data.

The set of jet probability tracks inside a tagged

TABLE VI: Ratios of observed to predicted rates of positive and negative tags when a P_J cut of 1% is applied. The first column specifies the sample used to build the matrix, while the second column reports the sample used to compute the rates. All(even)[odd] means that all(only even event number)[only odd event number] events are used. The errors shown are statistical only.

Matrix	Sample	Obs./Pred. Pos. Tag Rate Ratio	Obs./Pred. Neg. Tag Rate Ratio
Inc. Jet Even	Inc. Jet Odd	0.997±0.002	0.999±0.003
Inc. Jet Even	Jet20 Odd	0.987±0.003	0.970±0.006
Inc. Jet Even	Jet50 Odd	0.991±0.003	0.998±0.006
Inc. Jet Even	Jet70 Odd	0.997±0.004	0.996±0.006
Inc. Jet Even	Jet100 Odd	0.989±0.003	1.029±0.005
Jet20 All	Jet50 All	1.020±0.003	1.044±0.008
Inc. Jet Even	Trig. Jet Odd	0.976±0.002	0.978±0.004
Inc. Jet Even	Non trig. Jet Odd	1.028±0.003	1.028±0.005
Inc. Jet All	$\sum E_T^{jet}$ All	1.037±0.002	0.966±0.003

TABLE VII: Total relative uncertainties on the overall positive and negative tag rates. Different tag rate matrices are applied to orthogonal samples of jets as shown in Table VI, and the total uncertainty is taken as the sum in quadrature of the most relevant contributions. Sample refers to the largest uncertainty from lines 2 to 5 in Table VI.

P_J cut	Statistical	Trigger	\sum_j	Jet20→Jet50	Sample	TOTAL
Pos. $P_J < 1\%$	0.11%	2.4%	3.7%	2.0%	1.3%	5.0%
Neg. $P_J < 1\%$	0.25%	2.2%	3.4%	4.4%	3.0%	6.7%
Pos. $P_J < 5\%$	0.07%	1.5%	1.2%	1.6%	1.2%	2.8%
Neg. $P_J < 5\%$	0.09%	1.3%	2.4%	3.1%	2.2%	4.7%

jet is used to build a variable sensitive to the flavor content of the jet itself. The relative contributions from heavy and light partons to data are determined by fitting the distribution of this variable for tagged jets in data to Monte Carlo simulation templates for b , c and light jets. For data, a sample selected by requiring a jet with $E_T > 50$ GeV at the trigger level is used. For Monte Carlo simulation distributions, HERWIG is used to generate $2 \rightarrow 2$ processes with an outgoing parton $p_T > 40$ GeV/ c . We perform the fit using six different variables, the maximum impact parameter d_0 of the tracks in the jet, the maximum impact parameter significance S_{d_0} of the tracks in the jet, the mass of the system of tracks with $|d_0| > 0.01$ cm and $S_{d_0} > 2$, and the transverse momentum (P_T^{rel}) with respect to the jet direction of the system of tracks with $|d_0| > 0.01$ cm and $S_{d_0} > 2$.

The fit is made more robust by fitting the positive excess only, for which the distributions for negative tags are subtracted from the positive side. This removes contribution to the mistags due to detector resolution, which could be simulated poorly. The number of negative tags obtained for b , c and light jets in Monte Carlo simulation is normalized to the total number of negative tags found in data. From

the fit, the fractions of b , c and light jets in data are obtained; thus the ratio of positive to negative tags from light jets, β .

Figure 9 shows the result of the fit of the positive tag excess in data to Monte Carlo templates of the maximum impact parameter of the tracks contained within b , c and light tagged jets. A P_J cut of 1% is used. It should be noted that the c/b ratio gets a contribution from the c/b tagging efficiency ratio of about 0.2. The observed rise of light jets is the result of the fact that tags for light jets are usually due to one large impact parameter track. Table VIII summarizes the results of the mistag asymmetry measurement with the six variables chosen for $P_J < 1\%$ and 5%. As a final estimate of the mistag asymmetry, we take the average of the six measurements and assign the maximum difference between the average and each single determination as the uncertainty. The results are 1.56 ± 0.14 and 1.27 ± 0.17 for P_J cuts of 1% and 5%, respectively. The asymmetry is caused by secondary interactions with the detector material and residual lifetime effects from K 's and Λ 's, giving an excess of positive mistags. We study the expected contribution of K 's and Λ 's decays to the mistag asymmetry in Monte Carlo simulated events. We find

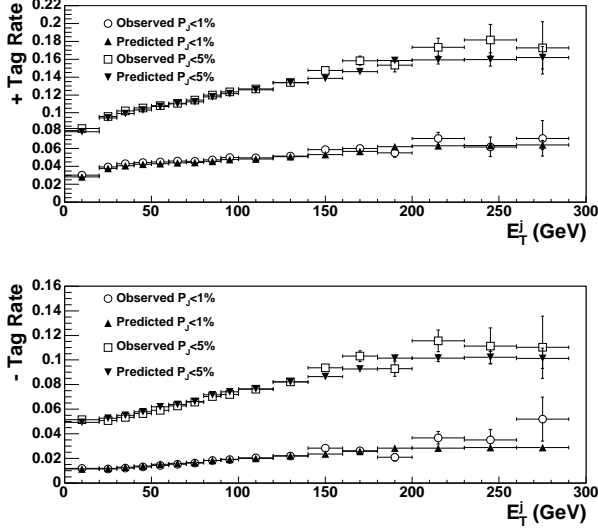


FIG. 8: Observed positive (top) and negative (bottom) tag rates as a function of E_T for events in $\sum E_T$ data vs. prediction from the matrix built with events in inclusive jet data. The two curves correspond to P_J cuts of 1% and 5%.

the ratio of positively to negatively tagged light jets to be 1.55 ± 0.11 (1.21 ± 0.04) for a P_J cut of 1% (5%). Uncertainties are statistical only. These results are in good agreement with our measurements on data and suggest K 's and Λ 's to be the main source of mistag asymmetry. The negative tag rates measured have therefore to be scaled up by the asymmetry factor in order to obtain an accurate estimate of the positive mistag rate. We repeat the measurement in bins of jet transverse energy to study the dependence of the mistag asymmetry on the jet E_T . Results are shown in Fig. 10. The asymmetry exhibits a small dependence with jet E_T which is taken into account to estimate the mistag background.

C. Jet Probability Performance on $t\bar{t}$ Events

We study the performance of the jet probability algorithm by computing the efficiency to tag a b jet in PYTHIA Monte Carlo $t\bar{t}$ events generated with a top mass = $178 \text{ GeV}/c^2$. Results are shown in Fig. 11 as a function of the transverse energy E_T and of the pseudo-rapidity η of the jets for P_J cuts of 1% and 5%. Jets are matched to b quarks (by requiring $\Delta R < 0.4$ between the reconstructed jet and the b quark) and the tagging SF is applied to the resulting efficiency. We also measure the average efficiency

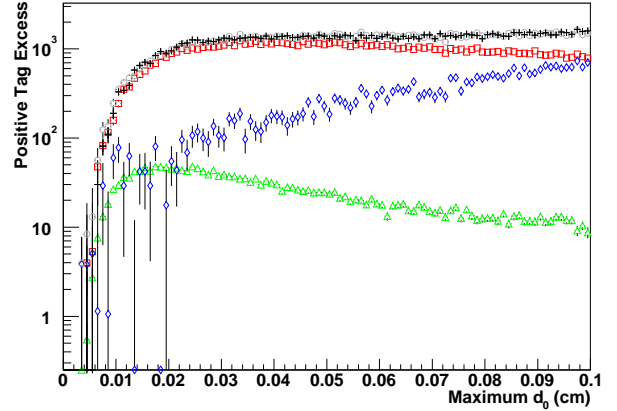


FIG. 9: Result of the fit of the positive tag excess in JET50 data as a function of the maximum impact parameter d_0 of jet probability tracks inside the tagged jets. A P_J cut of 1% is used. Observed data are the crosses, while the fitted component from b , c and light jets are the squares, triangles and diamonds, respectively. The circles are the sum of the three fitted components.

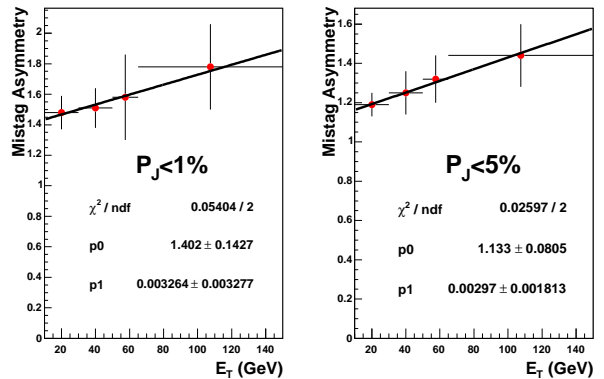


FIG. 10: Mistag asymmetry as a function of the jet transverse energy for $P_J < 1\%$ (left plot) and $P_J < 5\%$ (right plot).

to tag a b or a c jet in $t\bar{t}$ events passing the kinematic event selection described in Section V. Results are shown in Table IX before and after applying the tagging SF . The scaled per-jet efficiencies, together with the mistag matrix, are used to determine the efficiency to tag at least n jets per $t\bar{t}$ event, as described in Section VII. Although the tagging requirement results in some loss of efficiency for the $t\bar{t}$ signal, it significantly increases the signal-to-background ratio by heavily suppressing the dominant W +jets background.

TABLE VIII: Mistag asymmetry measured in Jet50 data for P_J cuts at 1% and 5%. The quoted uncertainties are derived from the uncertainty in the fits. The uncertainty used for the average is the maximum difference between the average and each measurement.

Fitted variable	$\beta (P_J < 1\%)$	$\beta (P_J < 5\%)$
Maximum d_0	1.64 ± 0.02	1.37 ± 0.02
Maximum S_{d_0}	1.56 ± 0.03	1.10 ± 0.02
Mass of the system of tracks with $ d_0 > 0.01 \text{ cm}$	1.51 ± 0.04	1.30 ± 0.02
Mass of the system of tracks with $S_{d_0} > 2$	1.43 ± 0.03	1.20 ± 0.02
$P_T^{rel.}$ of the system of tracks with $ d_0 > 0.01 \text{ cm}$	1.67 ± 0.03	1.32 ± 0.02
$P_T^{rel.}$ of the system of tracks with $S_{d_0} > 2$	1.57 ± 0.02	1.30 ± 0.02
Average	1.56 ± 0.14	1.27 ± 0.17

TABLE IX: Tagging efficiencies for b and c jets in $t\bar{t}$ events ($m_t = 178 \text{ GeV}/c^2$) before (raw efficiency) and after (scaled efficiency) applying the tagging scale factor.

	b jets		c jets	
	Raw Eff. (%)	Scaled Eff. (%)	Raw Eff. (%)	Scaled Eff. (%)
$P_J < 1\%$	43.2 ± 0.1	35.3 ± 3.0	9.6 ± 0.2	7.8 ± 0.7
$P_J < 5\%$	54.6 ± 0.1	46.5 ± 3.9	20.3 ± 0.2	17.3 ± 1.5

V. EVENT SELECTION

Top quark events in the lepton+jets channel are characterized by the presence of an electron or muon with high transverse energy, large missing transverse energy and four high energy jets, two of which are b jets. The basic pretag selection requires one tight electron or muon, $\cancel{E}_T > 20 \text{ GeV}$ and jets with corrected $E_T > 15 \text{ GeV}$ and $|\eta| < 2$.

In order to select a lepton+jets sample completely disjoint from the top dilepton sample ($t\bar{t} \rightarrow l^+l^-\nu\bar{\nu}q\bar{q}$), we reject events with an extra lepton that passes the loose requirements. Events consistent with $Z \rightarrow l^+l^-$ are removed if a tight lepton and a second object form an invariant mass within the range [76, 106] GeV/c^2 . If the tight lepton is an electron, the second object may be an isolated electromagnetic object, a jet with electromagnetic fraction greater than 0.95 or an oppositely-signed isolated track. If the tight lepton is a muon, the second object may be an isolated muon or an opposite-signed isolated track.

The event vertex z position is used to cluster jets and to ensure leptons and jets come from the same interaction. If more than one primary vertex is reconstructed in the event, the vertex closest to the lepton track is selected as event vertex. Events are rejected if the z of the lepton track is farther than 5 cm from the z of the event vertex. The vertex z position is required to be within 60 cm of the center of the detector in order to ensure good event reconstruction in

the projective tower geometry of the CDF detector. The efficiency of this requirement is measured using minimum bias data and found to be $(95.1 \pm 0.3)\%$. For consistency with the b -tagging algorithm, events are also rejected if the z of the vertex with highest $\sum p_T$ of all tracks is farther than 5 cm from the event vertex z . The efficiency of this requirement is $(98 \pm 2)\%$, where the 2% error accounts for the uncertainty in the simulation of multiple interactions.

The events selected by the above criteria are dominated by QCD production of W bosons in association with jets. Figure 12 shows the P_J distribution for taggable jets in this sample. In order to improve the signal to background ratio for $t\bar{t}$ events, we require at least one jet in the event to be tagged as a b jet. A $t\bar{t}$ event is expected to have four jets in the final state, but due to gluon radiation, jet merging, and inefficiencies in jet reconstruction, this number can eventually be different. We therefore use the tagged events with three or more jets to define our signal sample, while the events with one and two jets are used as a control sample.

A. Optimized Selection

The variable H_T , defined as the scalar sum of all the transverse energy in the event, i.e., the sum of the \cancel{E}_T , the electron E_T or muon p_T , and the E_T of the jets, is a measure of the energy in the hard

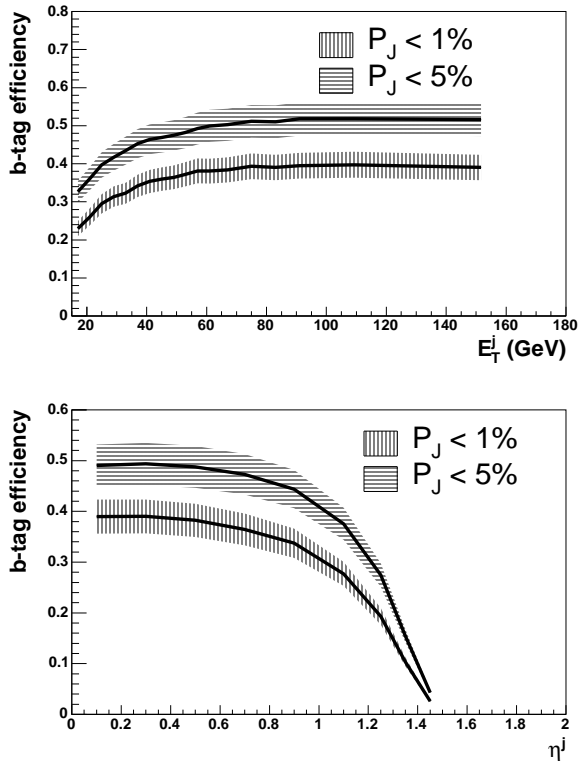


FIG. 11: Efficiency to tag b jets in $t\bar{t}$ Monte Carlo simulated events as a function of jet E_T (top) and jet η (bottom) for two different P_J cuts. The efficiency is obtained by multiplying the tag rate for jets matched to b quarks in the Monte Carlo simulation by the appropriate tagging scale factor. The bands represent the systematic uncertainty on the scale factors.

scatter, and is a powerful discriminant between the $t\bar{t}$ pair production signal events (S) and background events (B). In order to find the optimal H_T cut, we maximize the statistical significance ($S/\sqrt{S+B}$) in the signal region. Figure 13 (top) shows the H_T distribution of the $t\bar{t}$ Monte Carlo simulation, together with the various background contributions, properly normalized. Figure 13 (bottom) shows the statistical significance as a function of the H_T cut. Details about the background estimates and datasets used can be found in Section VI. Optimal statistical significance is reached with a cut of $H_T > 200$ GeV.

In addition, we enhance the W component of the sample by requiring the transverse mass of the lepton and the missing energy, $M_T^W = \sqrt{(E_T(l) + E_T(\nu))^2 - (\vec{P}_T(l) + \vec{P}_T(\nu))^2}$, be consistent with W boson production. Figure 14

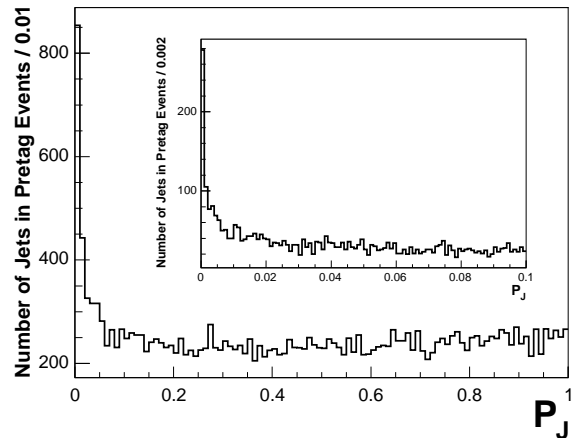


FIG. 12: The P_J distribution for taggable jets in the pre-tag sample (note that the vertical axis does not start at 0). The inset shows a zoom of the P_J distribution from 0.0 to 0.1.

(top) shows the M_T^W distribution for the $t\bar{t}$ Monte Carlo simulation together with the various normalized background contributions. Figure 14 (bottom) shows the statistical significance as a function of the M_T^W cut. Note that the non- W background lies at lower values of M_T^W . In the optimization of the M_T^W cut, we take S to be the number of events from real W bosons and B to be the number of events from non- W background. A cut of $M_T^W > 20$ GeV/ c^2 gives optimal statistical significance.

B. Yields of Events

Events which pass the selection criteria described so far, before applying b -tagging, form the pretag sample. The number of observed events in both the pretag and tagged samples for $P_J < 1\%$ and $P_J < 5\%$ are summarized in Table X as a function of the number of tight jets in the event.

VI. BACKGROUNDS: EXPECTED COMPOSITION OF THE b -TAGGED LEPTON+JETS SAMPLE

Other processes besides $t\bar{t}$ are expected to contribute to the tagged lepton+jets sample. The main contribution comes from heavy flavor production in association with a W boson ($Wb\bar{b}$, $Wc\bar{c}$, Wc). W +light flavor production also gives a significant

TABLE X: Yield of events in 318 pb⁻¹ of data for $P_J < 1\%$ and $P_J < 5\%$.

Jet Multiplicity	1 jet	2 jets	3 jets	≥ 4 jets
Pretag Events				
CEM	16897	2657	182	105
CMUP	8169	1175	83	44
CMX	4273	610	35	17
Total	29339	4442	300	166
Single Tagged Events, $P_J < 1\%$ (5%)				
CEM	207 (571)	106 (230)	33 (53)	36 (53)
CMUP	92 (256)	58 (105)	13 (24)	24 (29)
CMX	51 (148)	27 (50)	6 (10)	8 (11)
Total	350 (975)	191 (385)	52 (87)	68 (93)
Double Tagged Events, $P_J < 1\%$ (5%)				
CEM	—	8 (16)	7 (15)	9 (18)
CMUP	—	3 (9)	4 (4)	8 (17)
CMX	—	2 (3)	1 (3)	1 (4)
Total	—	13 (28)	12 (22)	18 (39)

contribution due to mistagged jets. Smaller contributions come from electroweak processes (diboson production, $Z \rightarrow \tau^+\tau^-$ events or single top) and generic QCD jet production with misidentified W bosons. These backgrounds are described in the following subsections.

A. Electroweak Processes

Electroweak processes are studied using Monte Carlo simulated samples. Diboson events (WW , WZ and ZZ) can contribute to the tagged lepton+jets sample when one boson decays leptonically and the other decays into heavy quarks. The process $Z \rightarrow \tau^+\tau^-$ can also give a contribution due to the leptonic decays of the tau. Finally, there is a contribution from single top quarks produced in association with a b quark through $q\bar{q}$ annihilation in W^* (s-channel) or W -gluon fusion (t-channel), in which an initial gluon splits into a $b\bar{b}$ pair and a b quark interacts with a virtual W .

The number of events from these processes are predicted based on their theoretical cross sections [37–39] (listed in Table XI), the measured integrated luminosity, and the acceptances and tagging efficiencies derived from Monte Carlo simulations. The expectations for these backgrounds are corrected for differences between Monte Carlo simulations and data, which include the lepton identification scale factor, trigger efficiencies, the z vertex cut efficiency and the tagging scale factor.

The total diboson, $Z \rightarrow \tau^+\tau^-$ and single top predictions for $P_J < 1\%$ (5%) are shown in Table XIX (Table XX) and account for 2.5% (3.0%) of the number of events in the signal region of 3 and ≥ 4 jets. Following the same procedure, we also compute the electroweak background contributions to the pretag sample. The results are shown in Table XVIII.

TABLE XI: Cross sections used to estimate electroweak backgrounds. For diboson and single top production, the theoretical values are used. For $Z \rightarrow \tau^+\tau^-$, we use the cross section measured by CDF.

Process	Cross Section (pb)
WW	13.25 ± 0.25
WZ	3.96 ± 0.06
ZZ	1.58 ± 0.02
Single Top $W - g$ (t-channel)	1.98 ± 0.08
Single Top W^* (s-channel)	0.88 ± 0.05
$Z \rightarrow \tau^+\tau^-$	254.3 ± 5.4

B. Non-W Background

The non- W background consists of events for which the lepton+ \cancel{E}_T signature is not due to the decay of a W boson. The main contribution to this source of background comes from QCD jet production where a jet provides the signature of a lepton and the missing transverse energy is due to a bad measurement of the jet energies. Semileptonic decays of b mesons and

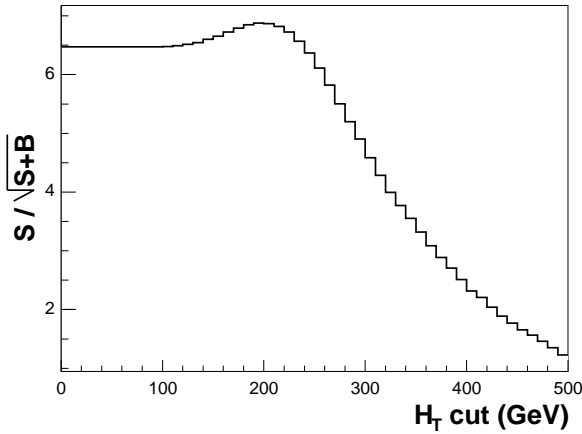
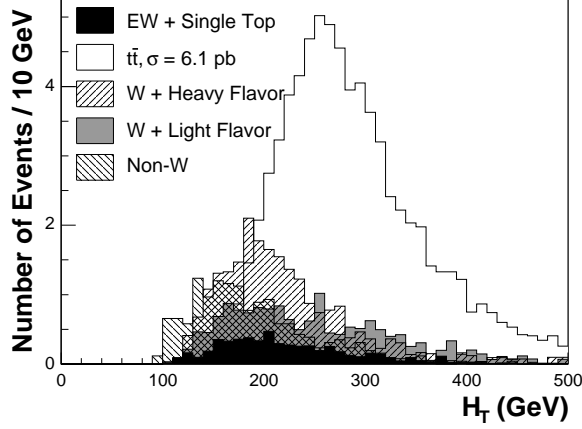


FIG. 13: Top: H_T distribution for tagged events with 3 or more tight jets in $t\bar{t}$ Monte Carlo simulation (6.1 pb) and main backgrounds, for an integrated luminosity of 318 pb^{-1} . Bottom: statistical significance as a function of the cut applied.

misidentified photon conversions can also contribute. Due to its inherent instrumental nature, this background is difficult to estimate. In the event selection, its contribution to the lepton+jets sample is minimized by the requirement on the W boson transverse mass M_T^W . In particular, note that the optimization of this cut has been performed by requiring the lepton to be non-isolated in order to have an independent data sample to construct the kinematical variables (we use region C of Fig. 15).

The method used to estimate the non- W background assumes that the isolation of the high- p_T lepton and the event \cancel{E}_T are uncorrelated for QCD processes, so that the ratio of non- W events with low lepton isolation to those with high lepton isolation in the region at low \cancel{E}_T is the same as in the high \cancel{E}_T region.

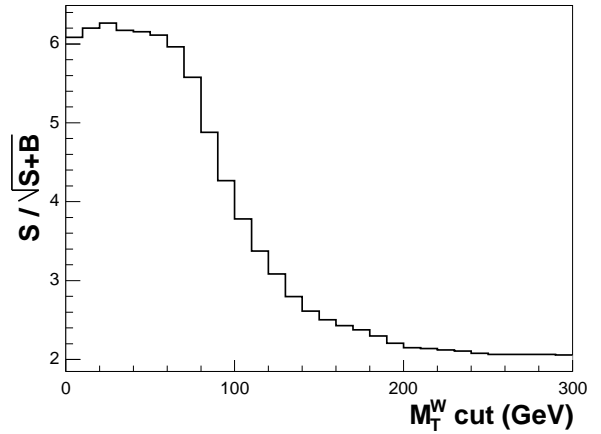
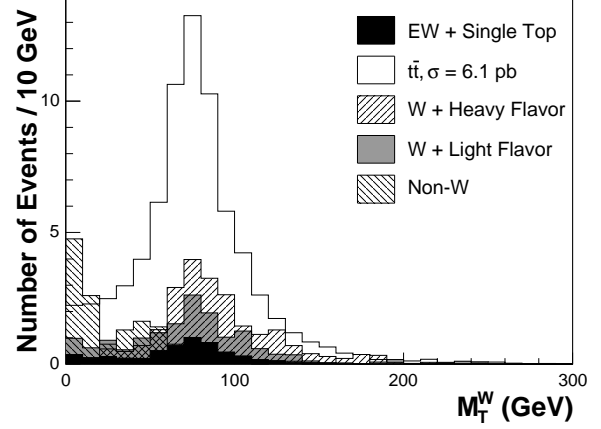


FIG. 14: Top: W_T^M distribution for tagged events with 3 or more tight jets in $t\bar{t}$ Monte Carlo simulation (6.1 pb) and main backgrounds, for an integrated luminosity of 318 pb^{-1} . Bottom: statistical significance as a function of the cut applied.

Four regions in the lepton isolation *versus* missing transverse energy plane are defined (see Fig. 15):

- Region A: Isolation > 0.2 and $\cancel{E}_T < 15 \text{ GeV}$
- Region B: Isolation < 0.1 and $\cancel{E}_T < 15 \text{ GeV}$
- Region C: Isolation > 0.2 and $\cancel{E}_T > 20 \text{ GeV}$
- Region D: Isolation < 0.1 and $\cancel{E}_T > 20 \text{ GeV}$.

The $t\bar{t}$ signal is expected to populate region D (signal region), while the non- W events dominate regions A, B and C (sideband regions). We can therefore estimate the fraction of events in the signal region which originate from non- W backgrounds as follows:

$$F_{non-W} = \frac{N_B \times N_C}{N_A \times N_D}, \quad (12)$$

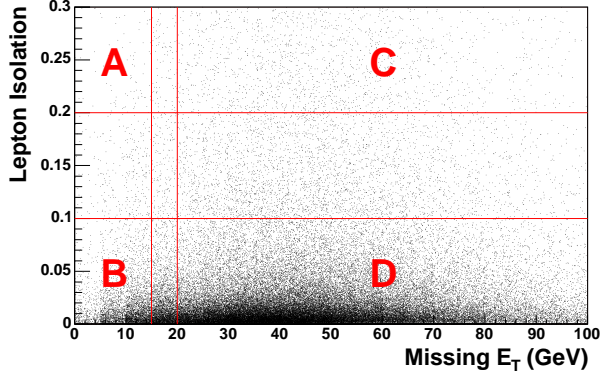


FIG. 15: Definition of the sideband regions used to estimate the non- W background. Lepton isolation *versus* missing transverse energy distribution for $t\bar{t}$ simulated events is also shown.

where N_A , N_B , N_C and N_D are the total numbers of observed events in the four regions. We describe next the estimate of the non- W events in both the pretag and tagged samples.

1. Fraction of non- W Events in the Pretag Sample

An estimate of the contribution of the non- W events to the pretag sample is mandatory to correctly normalize most of the backgrounds in the tagged sample. Table XII summarizes the results for the non- W fractions in the pretag sample as a function of the jet multiplicity for electrons and muons. Note that we do not apply the H_T and M_T^W cuts in regions A and B to preserve statistics. We correct the yields in regions A, B and C by subtracting the expected contribution from $t\bar{t}$ events assuming $\sigma_{t\bar{t}} = 6.1$ pb (this assumption is found to have a negligible impact on the final non- W estimate). Uncertainties in Table XII are statistical only. The main source of systematic uncertainty comes from the lepton isolation and missing transverse energy not being fully uncorrelated for QCD events. We study the effect of this assumption by varying the values of the \cancel{E}_T and lepton isolation cuts in the definition of the sideband regions. We observe a maximum variation of 50% in the resulting non- W fraction, which we assign as a systematic uncertainty on our estimates.

To further cross check the accuracy of the predictions, we define new intermediate isolation regions B' and D':

- Region B: $\cancel{E}_T < 15$, $\text{Isol} < 0.1 \rightarrow$ Region B': $\cancel{E}_T < 15$, $0.1 < \text{Isol} < 0.2$,

- Region D: $\cancel{E}_T > 20$, $\text{Isol} < 0.1 \rightarrow$ Region D': $\cancel{E}_T > 20$, $0.1 < \text{Isol} < 0.2$.

From the intermediate region B', we estimate the number of non- W events in region D'. The predicted non- W fractions are shown in Table XIII. The uncertainties quoted are statistical only. In the same table, these fractions are compared with the expected non- W fractions computed from the difference between the observed events and the contributions from $t\bar{t}$ and W +jets events. The expected number of $t\bar{t}$ events is derived by normalizing the Monte Carlo prediction to a cross section of 6.1 pb. In order to estimate the W +jets contribution in region D', we compute the ratio of W +jets events in the regions D' and D using simulations and normalize the expectations for W +jets production in D' to the number of events in the signal region after removing $t\bar{t}$, electroweak contributions. We compute the relative differences as the ratio of the difference between expected and predicted non- W fractions to the predicted fraction. For each jet multiplicity bin, the differences between predicted and expected non- W fractions in region D' are consistent with the 50% uncertainty we derived varying the \cancel{E}_T and lepton isolation cuts in the definition of the sideband regions.

2. Non- W Events in the Tagged Sample

The non- W background contributes to the tagged sample through both real heavy flavor production ($b\bar{b}$ and $c\bar{c}$ events) and mistags. We compute the number of non- W events with tagged jets in the signal region using equation 12 with the numbers of tagged events in the sideband regions. Yields in regions A, B and C are corrected for $t\bar{t}$ contributions. The results are summarized in Table XIV: $(N_B/N_A)^{\text{tagged}}$ is the ratio of tagged events in regions B and A and it is used to normalize the number N_C^{tagged} of tagged events in the region C to get the expected number $N_{\text{non-}W}^{\text{tagged},l}$ of non- W events on the signal region. The precision of these estimates is limited by the number of tagged events in the sideband regions.

We cross check these results by estimating the non- W contribution to the tagged lepton+jets sample following two alternative methods. In the first one (*check 1*), we assume the tag rate in region D to be the same as in region B:

$$N_{\text{non-}W}^{\text{tagged}} = F_{\text{non-}W} \times N_D \times \epsilon_B, \quad (13)$$

where ϵ_B is the event tag rate in region B and N_D is the number of events in region D. This method has a large systematic uncertainty since the tag rate

TABLE XII: Number of events in the sideband regions and fraction of non- W events in the signal region before and after correcting for $t\bar{t}$ contribution. Quoted errors are statistical only.

Jet Multiplicity	1 jet	2 jets	3 jets	≥ 4 jets
Pretag Electrons				
Region A	100600	12756	1745	216
Region B	61818	5228	593	98
Region C	1651	428	27	15
Region D	16897	2657	182	105
$F_{non-W}^{uncorr.}$	0.060 ± 0.002	0.066 ± 0.004	0.05 ± 0.01	0.06 ± 0.02
F_{non-W}	0.060 ± 0.002	0.066 ± 0.004	0.05 ± 0.01	0.05 ± 0.02
Pretag Muons				
Region A	36599	5248	657	97
Region B	11718	968	114	21
Region C	737	181	12	11
Region D	12442	1785	118	61
$F_{non-W}^{uncorr.}$	0.0190 ± 0.0007	0.019 ± 0.002	0.018 ± 0.006	0.04 ± 0.02
F_{non-W}	0.0190 ± 0.0007	0.019 ± 0.002	0.014 ± 0.005	0.03 ± 0.01

TABLE XIII: Predicted and expected fractions of non- W events in the intermediate region D' for the electron and muon samples. Errors are statistical only.

Jet Multiplicity	1 jet	2 jets	3 jets	≥ 4 jets
Electron+Jets Sample				
Predicted Non- W Fraction	0.82 ± 0.03	0.60 ± 0.05	0.53 ± 0.16	0.49 ± 0.21
Expected Non- W Fraction	0.78 ± 0.01	0.82 ± 0.02	0.76 ± 0.10	0.59 ± 0.16
Fractional Relative Difference	-0.05	0.37	0.42	0.20
Muon+Jets Sample				
Predicted Non- W Fraction	0.41 ± 0.03	0.41 ± 0.06	0.40 ± 0.23	0.40 ± 0.33
Expected Non- W Fraction	0.70 ± 0.02	0.62 ± 0.05	0.44 ± 0.22	0.26 ± 0.25
Fractional Relative Difference	0.70	0.50	0.11	-0.35

could depend on the missing transverse energy due to the contribution of $b\bar{b}$ events with a b quark decaying into leptons. Events with large \cancel{E}_T would have a larger heavy flavor contribution due to real neutrino production from semileptonic b decay. In the second alternative method (*check 2*), we compute the tagging rates per jet in the sideband regions, and then we predict the tag rate per jet in the signal region D as

$$Pred\ Tag\ Rate\ D = \frac{Tag\ Rate\ B \times Tag\ Rate\ C}{Tag\ Rate\ A}. \quad (14)$$

We compute the jet tagging rate by assuming it to be the same in all the jet multiplicity bins and use this estimate to predict the non- W background in the signal region taking into account the jet multiplicity and the number of non- W events expected in the pretag

lepton+jets sample. Table XV compares the non- W contributions predicted by the three methods.

Finally, we use the results of the two alternative estimates to assign a systematic uncertainty of 50% which takes into account the differences with the base method. The total non- W background accounts for 1.2% of the observed events with tagged jets in the signal region, both for $P_J < 1\%$ and $P_J < 5\%$.

C. W + Heavy Flavor Processes

W +heavy flavor production is the main source of background in the tagged lepton+jets sample. It is estimated using the heavy flavor fractions in W boson production in association with partons and the tagging efficiency for these processes. These quantities are derived from Monte Carlo simulations. The

TABLE XIV: The number of non- W events in the signal region D estimated from the corrected numbers of tagged events in the sideband regions with equation 12. Uncertainties are statistical only.

Jet Multiplicity	1 jet	2 jets	3 jets	≥ 4 jets
Electron+Jets Sample ($P_J < 1\%$)				
$(N_B/N_A)^{tagged}$	0.36 ± 0.01	0.26 ± 0.02	0.26 ± 0.05	0.4 ± 0.2
N_C^{tagged}	74.8	25.1	1.8	1.0
$N_{non-W}^{tagged,e}$	26.7 ± 3.3	6.6 ± 1.4	0.5 ± 0.4	0.4 ± 0.4
Muon+Jets Sample ($P_J < 1\%$)				
$(N_B/N_A)^{tagged}$	0.102 ± 0.008	0.10 ± 0.02	0.11 ± 0.04	0.2 ± 0.1
N_C^{tagged}	36.9	20.3	4.0	0.81
$N_{non-W}^{tagged,\mu}$	3.8 ± 0.7	2.0 ± 0.6	0.5 ± 0.3	0.2 ± 0.1
Electron+Jets Sample ($P_J < 5\%$)				
$(N_B/N_A)^{tagged}$	0.42 ± 0.01	0.33 ± 0.02	0.29 ± 0.04	0.5 ± 0.1
N_C^{tagged}	142.8	52.9	3.5	1.5
$N_{non-W}^{tagged,e}$	59.6 ± 5.2	17.6 ± 2.6	1.0 ± 0.5	0.7 ± 0.6
Muon+Jets Sample ($P_J < 5\%$)				
$(N_B/N_A)^{tagged}$	0.141 ± 0.007	0.12 ± 0.01	0.09 ± 0.03	0.17 ± 0.07
N_C^{tagged}	65.8	32.1	3.7	0.6
$N_{non-W}^{tagged,\mu}$	9.3 ± 1.2	3.8 ± 0.8	0.3 ± 0.2	0.1 ± 0.1

TABLE XV: Number of non- W events expected in the tagged lepton+jets sample as a function of the jet multiplicity for the three methods described. Uncertainties are statistical only.

Jet Multiplicity	1 jet	2 jets	3 jets	≥ 4 jets
$P_J < 1\%$				
N_{non-W}^{tagged}	30.5 ± 3.3	8.6 ± 1.5	0.9 ± 0.5	0.5 ± 0.4
$N_{non-W}^{tagged, check 1}$	19.0 ± 0.7	6.7 ± 0.6	0.6 ± 0.1	0.6 ± 0.3
$N_{non-W}^{tagged, check 2}$	27.7 ± 2.6	9.3 ± 0.9	0.7 ± 0.1	0.6 ± 0.2
$P_J < 5\%$				
N_{non-W}^{tagged}	68.8 ± 5.4	21.4 ± 2.8	1.3 ± 0.6	0.8 ± 0.6
$N_{non-W}^{tagged, check 1}$	43.5 ± 1.3	16.2 ± 1.0	1.1 ± 0.2	1.6 ± 0.5
$N_{non-W}^{tagged, check 2}$	65.4 ± 4.4	21.9 ± 1.8	1.6 ± 0.3	1.5 ± 0.4

overall normalization is obtained from the number of observed events in the pretag sample.

The estimate of the heavy flavor fraction in W +jets events is described elsewhere [7]. We use the ALPGEN event generator, which is able to compute exact matrix element calculations at leading order for parton level QCD and electroweak processes. We can therefore compute the ratio between the W +heavy flavor production cross section and the inclusive W +jets cross section since it is expected to be stable in the transition from leading-order to next-to-leading-order matrix elements. We generate events where inclusive W , $Wb\bar{b}$, $Wc\bar{c}$ and Wc are produced in as-

sociation with n light partons. Parton level events from ALPGEN are fed to the HERWIG parton shower program which generates additional jets from gluon radiation, and a full CDF detector simulation is applied. Events containing a different number n of light partons are combined following a rigorous prescription in order to avoid double counting due to parton shower radiation, which causes $W + n$ parton events to populate part of the phase space described by the $W + (n + 1)$ parton sample. The $Wb\bar{b}$ and $Wc\bar{c}$ samples are further divided into two classes according to the number of reconstructed heavy flavor jets in the event. We refer to these classes as 1B and 2B (1C

and 2C) for $Wb\bar{b}$ ($Wc\bar{c}$). By means of these combined Monte Carlo simulated samples, the heavy flavor fractions for W +jets events are measured as the ratio between the computed W +heavy flavor and W +jets cross sections. Jet data samples are used to correct for residual discrepancies between data and Monte Carlo simulations: a factor 1.5 ± 0.4 is applied to the $Wb\bar{b}$ and $Wc\bar{c}$ fractions [7], where the uncertainty is dominated by the systematic uncertainties associated with the ALPGEN heavy flavor calculations. The final heavy flavor fractions are shown in Table XVI.

The contribution of W +heavy flavor production to the pretag lepton+jets sample is estimated by multiplying heavy flavor fractions by the observed number of events in the pretag sample, corrected for the non- W , and electroweak background expectations. The results are shown in Table XVIII.

The above Monte Carlo simulated samples after pretag selection are used to compute the tagging efficiencies. In order to avoid double counting of the mistag background, the jet probability algorithm is applied only to jets known to be due to a b or c quark. Each tagged jet is weighted according to the scale factor. Results are summarized in Table XVII. The systematic uncertainties are dominated by the uncertainties on the scale factor for b and c jets. The pretag expectations are multiplied by the tagging efficiencies to estimate the contributions of these processes to the tagged sample. The numbers of $Wb\bar{b}$, $Wc\bar{c}$ and Wc events expected in the tagged lepton+jets sample for $P_J < 1\%$ (5%) are shown, along with the rest of the backgrounds, in Table XIX (Table XX) and account for 12.3% (13.2%) of the observed number of events in the signal region.

D. Mistag Background

Events in which jets from light partons are tagged as heavy flavor jets can contribute to the tagged sample. The number of events with negative tags in the pretag sample would be a simple estimate of this background, but this method has the problem of a large statistical uncertainty. Instead, we count the events in the pretag sample weighted by their probability to have at least one mistagged jet. This probability is computed by applying the negative tag rate matrix to all the taggable jets in the event.

This estimate is corrected for the mistag asymmetry derived in Section IV B 1. In order to take into account the dependence of the mistag asymmetry on the jet E_T , we convolute it with the jet E_T spectra in events with W +three or more jets for data and $t\bar{t}$ Monte Carlo simulation, as shown in Fig. 16. The ob-

served difference between the means of the distributions and the mistag asymmetry values measured in Section IV B 1 are negligible within the uncertainties. We therefore decide to use the former in our analysis. The RMS of the distributions gives an estimate of how much the asymmetry changes over the jets in our samples, and it is taken as an additional uncertainty on the mistag asymmetry. The final mistag asymmetry scale factors are 1.56 ± 0.17 for $P_J < 1\%$ and 1.27 ± 0.20 for $P_J < 5\%$.

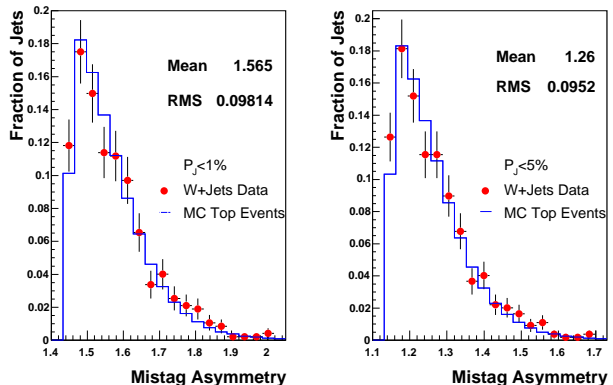


FIG. 16: Mistag asymmetry distribution for jets in data (dots) and $t\bar{t}$ Monte Carlo simulated events (histogram) in the signal region for $P_J < 1\%$ (5%) in the left (right) side.

The estimate of the mistag background is also scaled down by one minus the fraction of pretag events which are due to non- W , and electroweak backgrounds. The contribution of the mistag background to the lepton+jets sample when a jet with $P_J < 1\%$ (5%) is required is shown in Table XIX (Table XX) and accounts for 12.8% (27.9%) of the observed number of events in the signal region.

1. Mistag Cross Check

The negative tag rate matrix has been extensively tested on inclusive jet samples. Results are discussed in Section IV B. The mistag matrix is found to correctly predict the number of events with negatively tagged jets observed in independent samples to within a few percent. To further test the mistag matrix reliability on lepton+jets data, we select a subsample of events by requiring $\cancel{E}_T < 20$ GeV. This sample is expected to be dominated by QCD jet production with the high- p_T lepton signature provided by a jet. Figure 17 compares the observed number of

TABLE XVI: Summary of $Wb\bar{b}$, $Wc\bar{c}$ and Wc fractions. 1B and 2B (1C and 2C) indicate the $Wb\bar{b}$ ($Wc\bar{c}$) events with one and two b -jets (c -jets) reconstructed, respectively. Uncertainties are statistical only.

Jet Multiplicity	1 jet	2 jets	3 jets	≥ 4 jets
1B	0.010 ± 0.003	0.014 ± 0.004	0.024 ± 0.006	0.022 ± 0.006
2B	—	0.014 ± 0.004	0.023 ± 0.006	0.026 ± 0.007
1C	0.016 ± 0.004	0.024 ± 0.006	0.038 ± 0.010	0.035 ± 0.010
2C	—	0.018 ± 0.005	0.029 ± 0.008	0.037 ± 0.010
Wc	0.043 ± 0.009	0.060 ± 0.013	0.060 ± 0.013	0.059 ± 0.013

TABLE XVII: Jet probability tagging efficiencies for $Wb\bar{b}$, $Wc\bar{c}$ and Wc events. The first uncertainty is statistical, while the second is systematic.

Jet Multiplicity	1 jet	2 jet	3 jet	≥ 4 jets
Event Tagging Efficiencies (%), $P_J < 1\%$				
1B (≥ 1 tag)	$29.5 \pm 0.3 \pm 2.5$	$30.7 \pm 0.6 \pm 2.6$	$37.0 \pm 1.5 \pm 3.2$	$33.5 \pm 3.2 \pm 2.9$
2B (≥ 1 tag)	—	$50.5 \pm 0.7 \pm 4.3$	$56.0 \pm 1.6 \pm 4.8$	$54.6 \pm 2.2 \pm 4.7$
1C (≥ 1 tag)	$6.8 \pm 0.2 \pm 0.9$	$7.8 \pm 0.4 \pm 1.0$	$9.1 \pm 1.0 \pm 1.2$	$8.0 \pm 1.9 \pm 1.0$
2C (≥ 1 tag)	—	$13.5 \pm 0.6 \pm 1.7$	$16.8 \pm 1.5 \pm 2.2$	$14.3 \pm 1.7 \pm 1.8$
Wc (≥ 1 tag)	$7.2 \pm 0.2 \pm 0.9$	$7.9 \pm 0.3 \pm 1.0$	$8.3 \pm 0.9 \pm 1.1$	$6.9 \pm 1.1 \pm 0.9$
Event Tagging Efficiencies (%), $P_J < 5\%$				
1B (≥ 1 tag)	$39.6 \pm 0.3 \pm 3.4$	$40.8 \pm 0.6 \pm 3.4$	$47.1 \pm 1.6 \pm 4.0$	$41.4 \pm 3.4 \pm 3.5$
2B (≥ 1 tag)	—	$63.5 \pm 0.7 \pm 5.4$	$68.4 \pm 1.5 \pm 5.8$	$66.7 \pm 2.1 \pm 5.6$
1C (≥ 1 tag)	$14.8 \pm 0.3 \pm 1.9$	$17.2 \pm 0.5 \pm 2.2$	$18.7 \pm 1.4 \pm 2.4$	$16.3 \pm 2.6 \pm 2.1$
2C (≥ 1 tag)	—	$27.1 \pm 0.8 \pm 3.4$	$33.2 \pm 1.9 \pm 4.2$	$32.3 \pm 2.3 \pm 4.1$
Wc (≥ 1 tag)	$15.3 \pm 0.3 \pm 1.9$	$16.4 \pm 0.5 \pm 2.1$	$19.4 \pm 1.3 \pm 2.5$	$18.6 \pm 1.7 \pm 2.4$

events with negative tags and the matrix prediction as a function of the jet multiplicity. Good agreement is observed confirming the reliability of the mistag matrix to predict the negative tag rate in events dominated by prompt jets. We repeat the test on the pretag lepton+jets sample, where a $\cancel{E}_T > 20$ GeV requirement is applied. Results are shown in Fig. 18. We observe a discrepancy between observed and predicted negative tags which we attribute to the higher fraction of heavy flavor in lepton+jets events with high value of \cancel{E}_T with respect to the inclusive jet samples where the matrix has been computed. To corroborate this hypothesis, we make a first-order correction to the mistag prediction by using the heavy flavor fractions (f_T) in W +jets events (see Table XVI). We compute the negative tag rates for light (M_l) and heavy (M_h) flavor jets in $t\bar{t}$ Monte Carlo simulation. For each jet multiplicity bin, a scale factor R is then determined as:

$$R = (1 - \sum f_T) + \sum f_T C_T, \quad (15)$$

$$T = 1B, 2B, 1C, 2C, Wc, \quad (16)$$

where

$$C_T = \frac{1 - (1 - M_l)^{j-k}(1 - M_h)^k}{1 - (1 - M_l)^j}. \quad (17)$$

The numbers j and k in the formula are the jet multiplicity and the number of heavy flavor jets ($k = 1$ for $T = 1B, 1C$ or Wc and $k = 2$ for $T = 2B$ or $2C$), respectively. The corrected distributions, also shown in Fig. 18, show a much better agreement with the observed rates of negative tagged events. We therefore use the mistag matrix prediction corrected by the mistag asymmetry as an estimate of the number of events with a tagged light jet.

E. Background Summary

Table XVIII summarizes the contributions of the different background estimates in the pretag sample. The difference between the observed number of events and the total background estimate is due to W +light flavor and $t\bar{t}$ contributions.

Table XIX and Table XX summarize the contri-

TABLE XVIII: Summary of the background estimate in the pretag sample. The difference between the total background estimate and the observed number of events is due to W +light flavor and $t\bar{t}$ contributions.

Jet Multiplicity	1 jet	2 jets	3 jets	≥ 4 jets
Electroweak				
WW	127 ± 9	123 ± 9	10.0 ± 0.8	3.6 ± 0.3
WZ	16.8 ± 1.2	18.8 ± 1.4	1.7 ± 0.1	0.61 ± 0.06
ZZ	0.67 ± 0.05	0.68 ± 0.05	0.14 ± 0.02	0.052 ± 0.008
Single Top $W - g$	13.4 ± 1.1	13.6 ± 1.1	1.44 ± 0.12	0.38 ± 0.04
Single Top W^*	4.0 ± 0.4	7.9 ± 0.7	1.02 ± 0.10	0.24 ± 0.02
$Z \rightarrow \tau^+\tau^-$	87 ± 7	16.5 ± 1.7	1.0 ± 0.3	0 ± 0
Total	249 ± 18	180 ± 13	15.3 ± 1.2	4.9 ± 0.4
W + Heavy Flavor				
Wbb	281 ± 75	116 ± 31	12.9 ± 3.3	7.4 ± 2.0
$Wc\bar{c}$	459 ± 123	170 ± 46	18.4 ± 5.0	11.1 ± 3.1
Wc	1197 ± 252	243 ± 53	16.9 ± 3.6	9.1 ± 2.0
Total	1938 ± 322	530 ± 94	47.8 ± 9.0	27.5 ± 5.5
Others				
Non- W	1250 ± 626	208 ± 104	10.0 ± 5.3	7.3 ± 4.1
Total Background	3436 ± 741	917 ± 150	73 ± 11	39.7 ± 7.2
Data	29339	4442	300	166

butions of the different background sources in the tagged lepton+jets sample for $P_J < 1\%$ and $P_J < 5\%$ respectively.

We observe good agreement between data and background predictions in events with one and two jets, which supports the validity of our background estimates. In events with three or more jets, we observe an excess of tagged events in data which we attribute to $t\bar{t}$ events. The estimates of the W +heavy flavor and mistag background contributions have been normalized to the data in the pretag sample assuming no signal. Having actually observed a significant number of $t\bar{t}$ events in the tagged sample, we need to correct those estimates by the number of signal events in the pretag sample. We make this correction through an iterative procedure which is described in Section VIII.

VII. SIGNAL ACCEPTANCE

The signal acceptance, or $t\bar{t}$ event detection efficiency, is defined as the fraction of $t\bar{t}$ events that satisfy all selection requirements, and includes trigger and reconstruction efficiencies as well as the efficiencies of the kinematic selection and of the b -tagging algorithm. We measure it using a PYTHIA $t\bar{t}$ Monte Carlo sample generated with a top quark mass $m_t = 178 \text{ GeV}/c^2$ and simulated as discussed

in Section III. Wherever possible, effects which are not sufficiently well modeled in the simulation are measured using data. The acceptance is defined as

$$\begin{aligned} \epsilon_{t\bar{t}} &= (A_{t\bar{t}} \times K_{lep} \times \epsilon_{trig} \times \epsilon_{z_0} \times \epsilon_{zvtx}) \times \epsilon_{b-tag} \\ &= \epsilon_{t\bar{t}}^{\text{pretag}} \times \epsilon_{b-tag} \end{aligned} \quad (18)$$

where $A_{t\bar{t}}$ is the fraction of Monte Carlo simulated $t\bar{t}$ events which pass the kinematic requirements (except b -tagging) and includes the branching fraction for $t\bar{t} \rightarrow e/\mu + jets$, the lepton identification efficiency (including isolation and cosmic/conversion veto efficiency, as described in Section III), the dilepton and $Z^0 \rightarrow l^+l^-$ veto efficiencies, and the kinematic and geometric acceptances. $A_{t\bar{t}}$ is measured separately for electron and muon events. K_{lep} is a scale factor which takes into account the difference in lepton identification efficiency between data and Monte Carlo simulations estimated using $Z \rightarrow l^+l^-$ events; ϵ_{trig} is the trigger efficiency for identifying high p_T leptons and is measured using data from independent triggers. Both K_{lep} and ϵ_{trig} are discussed in Section III. ϵ_{z_0} and ϵ_{zvtx} are the efficiencies for the z vertex cuts described in Section V and ϵ_{b-tag} is the efficiency to tag at least one tight jet in a $t\bar{t}$ event and includes a tagging scale factor to account for differences between Monte Carlo simulations and data.

The event tagging efficiency ϵ_{b-tag} is obtained from

TABLE XIX: Summary of the background estimate in the lepton+jets sample when a jet with $P_J < 1\%$ is required.

Jet Multiplicity	1 jet	2 jets	3 jets	≥ 4 jets
Electroweak				
WW	2.2 ± 0.3	5.0 ± 0.6	0.7 ± 0.1	0.28 ± 0.06
WZ	1.0 ± 0.1	2.0 ± 0.2	0.23 ± 0.03	0.09 ± 0.02
ZZ	0.027 ± 0.006	0.09 ± 0.01	0.012 ± 0.004	0.007 ± 0.002
Single Top $W - g$	4.1 ± 0.5	4.9 ± 0.6	0.73 ± 0.08	0.20 ± 0.02
Single Top W^*	1.3 ± 0.2	4.2 ± 0.5	0.60 ± 0.07	0.14 ± 0.02
$Z \rightarrow \tau^+ \tau^-$	0.7 ± 0.3	0.4 ± 0.2	0.04 ± 0.04	0 ± 0
Total	9.3 ± 1.1	16.6 ± 1.8	2.3 ± 0.3	0.71 ± 0.09
W + Heavy Flavor				
Wbb	83 ± 23	47 ± 13	6.0 ± 1.6	3.3 ± 0.9
$Wc\bar{c}$	31 ± 9	17.5 ± 5.2	2.3 ± 0.7	1.2 ± 0.4
Wc	86 ± 21	19.2 ± 5.0	1.4 ± 0.4	0.6 ± 0.2
Total	200 ± 42	84 ± 20	9.6 ± 2.4	5.2 ± 1.4
Others				
Mistag	149 ± 17	51.8 ± 5.9	8.5 ± 1.0	6.7 ± 0.8
Non- W	31 ± 16	8.6 ± 4.6	0.9 ± 0.6	0.5 ± 0.5
Total Background	389 ± 49	161 ± 22	21.4 ± 2.7	13.1 ± 1.7
Data	350	191	52	68

TABLE XX: Summary of the background estimate in the lepton+jets sample when a jet with $P_J < 5\%$ is required.

Jet Multiplicity	1 jet	2 jets	3 jets	≥ 4 jets
Electroweak				
WW	5.5 ± 0.6	12.5 ± 1.4	1.81 ± 0.21	0.74 ± 0.10
WZ	1.6 ± 0.2	3.3 ± 0.3	0.40 ± 0.05	0.16 ± 0.02
ZZ	0.049 ± 0.009	0.14 ± 0.02	0.027 ± 0.006	0.014 ± 0.004
Single Top $W - g$	5.4 ± 0.6	6.5 ± 0.7	0.92 ± 0.10	0.26 ± 0.03
Single Top W^*	1.7 ± 0.2	5.2 ± 0.6	0.74 ± 0.08	0.17 ± 0.02
$Z \rightarrow \tau^+ \tau^-$	2.1 ± 0.5	1.1 ± 0.3	0.13 ± 0.10	0 ± 0
Total	16.3 ± 1.8	28.8 ± 3.0	4.0 ± 0.4	1.4 ± 0.1
W + Heavy Flavor				
Wbb	111 ± 31	61 ± 17	7.4 ± 2.0	4.1 ± 1.2
$Wc\bar{c}$	68 ± 20	36 ± 11	4.6 ± 1.4	2.7 ± 0.8
Wc	184 ± 45	40 ± 10	3.2 ± 0.8	1.7 ± 0.5
Total	363 ± 75	137 ± 31	15.2 ± 3.6	8.5 ± 2.1
Others				
Mistag	585 ± 92	194 ± 30	28.2 ± 4.4	22.1 ± 3.5
Non- W	69 ± 35	21 ± 11	1.3 ± 0.9	0.79 ± 0.74
Total Background	1033 ± 125	381 ± 46	48.8 ± 5.9	32.7 ± 4.2
Data	975	385	87	93

the same $t\bar{t}$ Monte Carlo simulated sample. We compute, for each $t\bar{t}$ event, the probability of having n tagged jets in the event by assigning to each jet a probability to be tagged. The sum of these probabilities over all the events returns the number of

expected events with at least n tags, from which we calculate the tagging efficiency. For light flavor jets, this probability is computed using the mistag matrix, while for heavy flavor jets the probability is the value of the tagging scale factor (see Section IV) if

TABLE XXI: Summary of acceptances for $t\bar{t}$ events. Efficiencies are expressed as percentages. The average $\epsilon_{b\text{-tag}}$ is the luminosity-weighted CEM/CMUP/CMX tagging efficiency. First uncertainty is statistical and the second one corresponds to systematics.

Quantity	CEM	CMUP	CMX
$\epsilon_{t\bar{t}}^{\text{pretag}}$	$3.67 \pm 0.02 \pm 0.22$	$1.92 \pm 0.01 \pm 0.12$	$0.751 \pm 0.008 \pm 0.046$
$\int Ldt$ (pb $^{-1}$)	318 ± 19	318 ± 19	305 ± 18
Single Tag, $P_J < 1\%$, $SF = 0.817 \pm 0.070$			
$\epsilon_{b\text{-tag}}$	$54.7 \pm 0.2 \pm 3.6$	$54.1 \pm 0.3 \pm 3.5$	$55.2 \pm 0.5 \pm 3.6$
Average $\epsilon_{b\text{-tag}}$	$54.5 \pm 0.2 \pm 3.6$		
$\epsilon_{t\bar{t}}$	$2.00 \pm 0.01 \pm 0.18$	$1.04 \pm 0.01 \pm 0.09$	$0.41 \pm 0.01 \pm 0.04$
$\epsilon_{t\bar{t}} \int Ldt$ (pb $^{-1}$)	$6.38 \pm 0.04 \pm 0.68$	$3.30 \pm 0.03 \pm 0.36$	$1.32 \pm 0.02 \pm 0.14$
Total $\epsilon_{t\bar{t}} \int Ldt$	$11.00 \pm 0.05(\text{stat}) \pm 1.17(\text{syst}) \text{ pb}^{-1}$		
Single Tag, $P_J < 5\%$, $SF = 0.852 \pm 0.072$			
$\epsilon_{b\text{-tag}}$	$68.8 \pm 0.2 \pm 3.7$	$68.6 \pm 0.3 \pm 3.7$	$69.6 \pm 0.5 \pm 3.7$
Average $\epsilon_{b\text{-tag}}$	$68.8 \pm 0.2 \pm 3.7$		
$\epsilon_{t\bar{t}}$	$2.52 \pm 0.01 \pm 0.20$	$1.315 \pm 0.009 \pm 0.108$	$0.523 \pm 0.006 \pm 0.042$
$\epsilon_{t\bar{t}} \int Ldt$ (pb $^{-1}$)	$8.03 \pm 0.05 \pm 0.80$	$4.19 \pm 0.03 \pm 0.42$	$1.67 \pm 0.02 \pm 0.17$
Total $\epsilon_{t\bar{t}} \int Ldt$	$13.89 \pm 0.06(\text{stat}) \pm 1.38(\text{syst}) \text{ pb}^{-1}$		

the jet is tagged and zero otherwise. We estimate the systematic uncertainty on the event tagging efficiency by varying the tagging scale factor and mistag prediction by $\pm 1\sigma$.

Table XXI summarizes the acceptance for $t\bar{t}$ events. For P_J cuts of 1% and 5%, the combined acceptance times integrated luminosity are, respectively, $11.00 \pm 0.05(\text{stat}) \pm 1.17(\text{syst}) \text{ pb}^{-1}$ and $13.89 \pm 0.06(\text{stat}) \pm 1.38(\text{syst}) \text{ pb}^{-1}$, where the statistical uncertainty is uncorrelated between the lepton types, and the systematic uncertainty is assumed to be 100% correlated since it is dominated by the luminosity and tagging scale factor uncertainties.

Table XXII summarizes the contributions to the systematic uncertainty on the signal acceptance. Trigger, lepton identification and z vertex cuts have already been discussed in Sections III and V. The observed difference in the conversion veto efficiency between $t\bar{t}$ events and the $Z \rightarrow e^+e^-$ sample used to measure the electron identification scale factor is added as an uncertainty on the tight electron identification efficiency. The efficiency of the cosmic ray veto is measured from data and accounts for a 1% uncertainty on the tight muon identification efficiency. Additional uncertainties in the electron (muon) acceptance are due to E_T (p_T) scale, E_T (p_T) resolution and material (geometrical) effects, and are found to be 0.3% (1.2%) in inclusive W events. The lepton isolation uncertainty accounts for differences in the modeling of the lepton identification in events with different jet multiplicity. It has been evaluated

by comparing data to Monte Carlo simulations for W +jets and $t\bar{t}$ events. The uncertainty due to the jet energy scale is estimated by the shift in signal acceptance observed by changing the jet energy corrections within their uncertainties. The uncertainty due to parton distribution functions (PDF) is estimated by re-weighting the $t\bar{t}$ events generated with CTEQ5L for different sets of PDFs [28]. In particular, we consider the difference in signal acceptance between NLO CTEQ6M and CTEQ5L, between MRST for two different values of α_S , and between NLO CTEQ6M and the 20 CTEQ eigenvectors, and we add in quadrature all the contributions. Differences in the modeling of $t\bar{t}$ production and decay are evaluated as the difference in acceptance between samples of signal events generated with HERWIG and PYTHIA. Samples of $t\bar{t}$ events with different levels of initial and final state radiation (ISR/FSR) are used to evaluate the effect of this source of uncertainty on the signal acceptance. The systematic uncertainty on the event tagging efficiency is estimated by varying the tagging scale factor and the mistag prediction by $\pm 1\sigma$. The total systematic uncertainty on the signal acceptance is 8.9% (8.0%) for $P_J < 1\%$ (5%), and is dominated by the tagging scale factor and the jet energy scale uncertainties.

TABLE XXII: Summary of the systematic uncertainties on the signal acceptance. The second column quotes the relative uncertainty on the indicated quantities, while the third column shows the effect on the overall $t\bar{t}$ acceptance.

Source	Relative Uncertainty (%)	Uncertainty on the Acceptance (%)
Central Electron Trigger	0.6	0.3
Central Electron ID SF	0.5	0.3
Conversion Veto Eff.	1.4	0.8
E_T Scale of Electron	0.3	0.2
Central Muon Trigger	0.5	0.2
Central Muon ID SF	1.0	0.3
CMX Muon Trigger	0.4	0.05
CMX Muon ID SF	0.6	0.07
Cosmic Veto Eff.	1.0	0.4
p_T Scale of Muon	1.2	0.5
Lepton Isolation	2.0	2.0
$ Z_{vtx} $ Cut Eff.	0.3	0.3
$Z_{vtx}^{JetProb}$ Cut Eff.	2	2
Jet Energy Scale	—	4.2
PDF	—	2
MC Modeling	—	1.6
ISR/FSR	—	1.3
Tagging SF $P_J < 1\%$ (b's/c's)	8.6/12.9	6.5
Mistag Asymmetry $P_J < 1\%$	11.0	0.2
Tagging SF $P_J < 5\%$ (b's/c's)	8.5/12.7	5.4
Mistag Asymmetry $P_J < 5\%$	15.5	0.4
Total Uncertainty ($P_J < 1\%$)	—	8.9
Total Uncertainty ($P_J < 5\%$)	—	8.0

VIII. CROSS SECTION FOR SINGLE TAGGED EVENTS

We measure the cross section as

$$\sigma_{t\bar{t}} = \frac{N_{obs} - N_{bck}}{\epsilon_{t\bar{t}} \times \int L dt}, \quad (19)$$

where N_{obs} is the observed number of events with at least one jet tagged, N_{bck} is the background estimate in the signal region, $\epsilon_{t\bar{t}}$ is the signal acceptance including the tagging efficiency and $\int L dt$ is the integrated luminosity. The estimated number of background events must be corrected for the $t\bar{t}$ contribution, since we normalize mistag and W +heavy flavor backgrounds assuming no $t\bar{t}$ signal events in the pretag sample. We apply an iterative procedure in which we first estimate the number of tagged top candidates in the sample as the number of tagged signal events minus the total background in the ≥ 3 jet bins. Successively, the obtained signal cross section is used to estimate the number of $t\bar{t}$ events before the b -tagging requirement, and this contribution is subtracted from the total number of events to which we normalize the mistag, $Wb\bar{b}$, $Wc\bar{c}$ and Wc

backgrounds. The expectations for single top, diboson and $Z \rightarrow \tau^+ \tau^-$ do not change with the number of $t\bar{t}$ events in the signal region. The change for non- W background is found to be negligible compared to its uncertainty. Therefore, this background is also kept fixed. Having obtained a new estimate for the tagged background, we re-evaluate the number of $t\bar{t}$ candidates. The procedure is repeated until the cross section $\sigma_{t\bar{t}}$ changes by less than 0.1%.

Starting with the backgrounds shown in Tables XIX and XX, we apply the iterative procedure and measure

$$\sigma_{t\bar{t}} = 8.9_{-1.0}^{+1.0}(\text{stat.})_{-1.0}^{+1.1}(\text{syst.}) \text{ pb}$$

for $P_J < 1\%$. As a cross check, we apply the iterative procedure for $P_J < 5\%$ and measure

$$\sigma_{t\bar{t}} = 9.6_{-0.9}^{+1.0}(\text{stat.})_{-1.1}^{+1.2}(\text{syst.}) \text{ pb.}$$

The final signal and background estimates are shown in Table XXIII, together with the observed number of events.

Figure 19 compares the numbers of observed data to background and signal expectations, for $P_J < 1\%$

TABLE XXIII: Summary of the final signal and background estimates and observed data in the single tag sample.

Jet Multiplicity	1 jet	2 jets	3 jets	≥ 4 jets
Pretag Data	29339	4442	300	166
$P_J < 1\%$				
Electroweak	9.3 ± 1.1	16.6 ± 1.8	2.3 ± 0.3	0.71 ± 0.09
$Wb\bar{b}$	83 ± 23	47 ± 13	4.3 ± 1.2	1.1 ± 0.3
$Wc\bar{c}$	31 ± 9	17.3 ± 5.2	1.6 ± 0.5	0.4 ± 0.1
Wc	86 ± 21	19.0 ± 4.9	1.0 ± 0.3	0.21 ± 0.06
Mistag	149 ± 17	51 ± 6	6.1 ± 0.7	2.2 ± 0.3
Non- W	31 ± 16	8.6 ± 4.6	0.9 ± 0.6	0.5 ± 0.5
Total Background	389 ± 49	159 ± 22	16.3 ± 2.0	5.1 ± 0.7
$t\bar{t}$ (8.9 pb)	2.5 ± 0.5	20.6 ± 2.4	40.4 ± 4.5	58.1 ± 6.2
Data	350	191	52	68
$P_J < 5\%$				
Electroweak	16.3 ± 1.8	28.8 ± 3.0	4.0 ± 0.4	1.4 ± 0.1
$Wb\bar{b}$	111 ± 31	60 ± 17	5.2 ± 1.4	1.1 ± 0.3
$Wc\bar{c}$	68 ± 20	36 ± 11	3.2 ± 1.0	0.76 ± 0.24
Wc	184 ± 45	40 ± 10	2.2 ± 0.6	0.5 ± 0.13
Mistag	585 ± 92	191 ± 30	19.6 ± 3.1	6.1 ± 1.0
Non- W	69 ± 35	21 ± 11	1.3 ± 0.9	0.8 ± 0.7
Total Background	1033 ± 125	377 ± 46	35.5 ± 4.2	10.6 ± 1.4
$t\bar{t}$ (9.6 pb)	3.6 ± 0.6	28.4 ± 3.1	55.1 ± 5.7	78.6 ± 7.8
Data	975	385	87	93

and 5%, for the measured $t\bar{t}$ production cross sections.

The statistical uncertainty on the measured cross section is dominated by the data sample size. Table XXIV summarizes the systematic contributions to the cross section uncertainty. The correlations in acceptances, tagging scale factor and luminosity uncertainty are taken into account. $Wb\bar{b}$ and $Wc\bar{c}$ systematics are considered correlated across all the bins. All the other uncertainties are treated as uncorrelated.

A. $t\bar{t}$ Cross Section Dependence on the Top Quark Mass

The signal acceptance used in this analysis has been computed using a sample of $t\bar{t}$ events generated with PYTHIA for $m_t = 178$ GeV/ c^2 , which corresponds to the combined Run I top mass measurement at the Tevatron Collider [3]. We study the dependence of the $t\bar{t}$ cross section on the top quark mass by reevaluating the signal acceptance through a set of Monte Carlo simulated samples generated by HERWIG for different values of the top mass. Results are shown in Fig. 20. A linear fit to the mea-

sured cross sections as a function of the top mass returns a slope of -0.052 ± 0.008 pb/(GeV/ c^2) and -0.066 ± 0.008 pb/(GeV/ c^2) for $P_J < 1\%$ and 5% respectively, where the uncertainties are due to Monte Carlo simulation statistics. Note that the fit results for $m_t = 178$ GeV/ c^2 agree with the measured cross section within the 1.6% uncertainty estimated in Section VII due to different modeling in PYTHIA and HERWIG.

B. Electron versus Muon $t\bar{t}$ Cross Section Measurements

As an additional cross check, we measure the cross section separately for events with tight electrons and muons. Table XXV summarizes the cross sections for the two analyses with $P_J < 1\%$ and $P_J < 5\%$. The cross section measurements in the electron and muon+jets samples agree within their statistical uncertainty.

TABLE XXIV: Summary of the systematic uncertainties in the single tag analysis.

Source	Fractional Syst. Uncert. (%)	Contribution to $\sigma_{t\bar{t}}$ (%)	
		$P_J < 1\%$	$P_J < 5\%$
Central Electron ID	1.6	+0.99/-0.97	+1.00/-0.98
Central Muon ID	1.9	+0.61/-0.61	+0.62/-0.61
CMX Muon ID	1.8	+0.22/-0.22	+0.22/-0.22
PDF	2	+2.1/-2.0	+2.1/-2.0
Jet Energy Scale	4.2	+4.5/-4.2	+4.6/-4.2
Lepton Isolation	2	+2.1/-2.0	+2.1/-2.0
ISR/FSR	1.3	+1.4/-1.3	+1.4/-1.3
MC Modeling	1.6	+1.7/-1.6	+1.7/-1.6
Z Vertex	2.0	+2.1/-2.1	+2.2/-2.1
Tagging SF $P_J < 1\%$ (b's/c's)	8.6/12.9	+8.2/-7.2	—
Tagging SF $P_J < 5\%$ (b's/c's)	8.5/12.7	—	+7.0/-6.3
Mistag Asymmetry $P_J < 1\%$	11.0	+0.93/-0.93	—
Mistag Asymmetry $P_J < 5\%$	15.5	—	+3.0/-3.0
Non- W Fraction	50	0.33	0.56
Non- W Prediction	50	0.71	0.79
W +HF Prediction	30	2.6	2.9
Cross Sections Bck.	1.8	0.056	0.072
Luminosity	5.9	+6.5-5.7	+6.5-5.8
Total Systematic Uncertainty		+12.5/-11.3	+12.3/-11.3

TABLE XXV: Summary of the cross sections for $P_J < 1\%$ and $P_J < 5\%$ and for each lepton type. Results are expressed in pb.

	Total	Electrons	Muons
$P_J < 1\%$	$8.9^{+1.0}_{-1.0}$ (stat.) $^{+1.1}_{-1.0}$ (syst.)	$8.6^{+1.4}_{-1.2}$ (stat.) $^{+1.1}_{-1.0}$ (syst.)	$9.4^{+1.7}_{-1.4}$ (stat.) $^{+1.2}_{-1.0}$ (syst.)
$P_J < 5\%$	$9.6^{+1.0}_{-0.9}$ (stat.) $^{+1.2}_{-1.1}$ (syst.)	$9.4^{+1.3}_{-1.2}$ (stat.) $^{+1.2}_{-1.1}$ (syst.)	$9.9^{+1.6}_{-1.4}$ (stat.) $^{+1.2}_{-1.1}$ (syst.)

IX. CROSS SECTION FOR DOUBLE TAGGED EVENTS

The measurement of the $t\bar{t}$ cross section in a sample with at least two b tags follows the same procedure as the single tag analysis, with a much purer sample of $t\bar{t}$ events. As shown in Table X, after requiring the event selection described in Section V, we observe 30 (61) events with two b -tagged jets out of the 120 (180) events with at least one b -tagged jet for $P_J < 1\%$ ($P_J < 5\%$). Table XXVI shows the signal acceptances and the efficiencies to tag two jets in signal events passing the pretag selection. The total acceptance times luminosity for $P_J < 1\%$ and $P_J < 5\%$ is $2.57 \pm 0.02(\text{stat}) \pm 0.49(\text{syst}) \text{ pb}^{-1}$ and $4.92 \pm 0.04(\text{stat}) \pm 0.87(\text{syst}) \text{ pb}^{-1}$ respectively.

A. Backgrounds in the Double b -Tag Sample

A few differences with respect to the single tag analysis must be taken into account in order to estimate the backgrounds. We define the mistag background as the events with at least two mistagged jets. The negative tag rate matrix is applied to negatively taggable jets in the event and the probability to have at least two mistagged jets is summed over all events. The mistag prediction is scaled by the fraction of non- W , electroweak backgrounds and by the mistag asymmetry as is done for the single tag analysis.

Events with one real heavy flavor tag plus a mistag are included in the other background sources. The contribution of mistags to the W +heavy flavor background is taken into account by applying the mistag rate matrix to light flavor jets in events with an extra real tag when computing the tagging efficiency. Results are summarized in Table XXVII.

The strategy to estimate the non- W background

TABLE XXVI: Summary of acceptances for $t\bar{t}$ events. Efficiencies are expressed as percentages. The first uncertainty quoted is statistical and the second is systematic. The average $\epsilon_{b\text{-tag}}$ is the luminosity-weighted CEM/CMUP/CMX tagging efficiency.

Quantity	CEM	CMUP	CMX
$\epsilon_{t\bar{t}}^{\text{pretag}}$	$3.67 \pm 0.02 \pm 0.22$	$1.92 \pm 0.01 \pm 0.12$	$0.751 \pm 0.008 \pm 0.046$
$\int Ldt$ (pb^{-1})	318 ± 19	318 ± 19	305 ± 18
Double Tag, $P_J < 1\%$, $SF = 0.817 \pm 0.070$			
$\epsilon_{b\text{-tag}}$	$12.7 \pm 0.2 \pm 2.1$	$12.6 \pm 0.2 \pm 2.0$	$13.4 \pm 0.4 \pm 2.2$
Average $\epsilon_{b\text{-tag}}$	$12.7 \pm 0.1 \pm 2.1$		
$\epsilon_{t\bar{t}}$	$0.465 \pm 0.006 \pm 0.081$	$0.241 \pm 0.004 \pm 0.042$	$0.101 \pm 0.003 \pm 0.018$
$\epsilon_{t\bar{t}} \int Ldt$ (pb^{-1})	$1.48 \pm 0.02 \pm 0.27$	$0.77 \pm 0.01 \pm 0.14$	$0.32 \pm 0.01 \pm 0.06$
Total $\epsilon_{t\bar{t}} \int Ldt$	$2.57 \pm 0.02(\text{stat}) \pm 0.49(\text{syst}) \text{ pb}^{-1}$		
Double Tag, $P_J < 5\%$, $SF = 0.852 \pm 0.072$			
$\epsilon_{b\text{-tag}}$	$24.4 \pm 0.2 \pm 3.6$	$24.1 \pm 0.3 \pm 3.6$	$25.2 \pm 0.5 \pm 3.7$
Average $\epsilon_{b\text{-tag}}$	$24.4 \pm 0.2 \pm 3.6$		
$\epsilon_{t\bar{t}}$	$0.895 \pm 0.009 \pm 0.142$	$0.462 \pm 0.006 \pm 0.074$	$0.189 \pm 0.004 \pm 0.030$
$\epsilon_{t\bar{t}} \int Ldt$ (pb^{-1})	$2.85 \pm 0.03 \pm 0.48$	$1.47 \pm 0.02 \pm 0.25$	$0.60 \pm 0.01 \pm 0.10$
Total $\epsilon_{t\bar{t}} \int Ldt$	$4.92 \pm 0.04(\text{stat}) \pm 0.87(\text{syst}) \text{ pb}^{-1}$		

TABLE XXVII: Jet probability tagging efficiencies for $Wb\bar{b}$, $Wc\bar{c}$ and Wc events for double tagged events. Values are expressed as percentages. The first uncertainty quoted is statistical and the second is systematic. 1B and 2B (1C and 2C) refer to $Wb\bar{b}$ ($Wc\bar{c}$) events with one and two reconstructed heavy flavor jets respectively.

jet multiplicity	2 jets	3 jets	≥ 4 jets
Double Tag Tagging Efficiencies, $P_J < 1\%$			
1B (≥ 2 tags)	$0.27 \pm 0.06 \pm 0.05$	$0.90 \pm 0.30 \pm 0.15$	$1.3 \pm 0.8 \pm 0.2$
2B (≥ 2 tags)	$10.3 \pm 0.4 \pm 1.8$	$13.1 \pm 1.1 \pm 2.2$	$14.1 \pm 1.5 \pm 2.4$
1C (≥ 2 tags)	$0.067 \pm 0.037 \pm 0.017$	$0.23 \pm 0.17 \pm 0.06$	$0.29 \pm 0.38 \pm 0.08$
2C (≥ 2 tags)	$0.43 \pm 0.12 \pm 0.11$	$1.3 \pm 0.5 \pm 0.3$	$1.1 \pm 0.5 \pm 0.3$
Wc (≥ 2 tags)	$0.05 \pm 0.03 \pm 0.01$	$0.20 \pm 0.14 \pm 0.05$	$0.22 \pm 0.21 \pm 0.06$
Double Tag Tagging Efficiencies, $P_J < 5\%$			
1B (≥ 2 tags)	$1.3 \pm 0.1 \pm 0.2$	$3.7 \pm 0.6 \pm 0.6$	$5.0 \pm 1.5 \pm 0.8$
2B (≥ 2 tags)	$18.6 \pm 0.6 \pm 3.1$	$23.9 \pm 1.4 \pm 4.0$	$26.0 \pm 1.9 \pm 4.4$
1C (≥ 2 tags)	$0.54 \pm 0.11 \pm 0.14$	$1.6 \pm 0.4 \pm 0.4$	$1.8 \pm 0.9 \pm 0.5$
2C (≥ 2 tags)	$2.5 \pm 0.3 \pm 0.6$	$5.6 \pm 0.9 \pm 1.4$	$6.3 \pm 1.2 \pm 1.6$
Wc (≥ 2 tags)	$0.40 \pm 0.08 \pm 0.10$	$1.5 \pm 0.4 \pm 0.4$	$2.1 \pm 0.6 \pm 0.5$

is changed, compared to that used for the single tag sample, due to low statistics in the double tagged event sample in the sideband regions (see Section VI B). We compute a common tag rate for all the jet multiplicity bins by using data in region B (isolation < 0.1 and $\cancel{E}_T < 15$ GeV). We divide the total number of double tagged events by the sum of the number of pretag events scaled by the jet pair multiplicity. Finally, we apply this tag rate to the pretag expectation in the signal region derived in Section VI B 1.

Background predictions for $P_J < 1\%$ and $P_J <$

5% are compared to the data in Tables XXVIII and XXIX, respectively.

The iterative procedure described in Section VIII is applied, and we obtain a cross section of

$$\sigma_{t\bar{t}} = 11.1_{-1.9}^{+2.3}(\text{stat.})_{-1.9}^{+2.5}(\text{syst.}) \text{ pb}$$

for $P_J < 1\%$ and

$$\sigma_{t\bar{t}} = 11.6_{-1.5}^{+1.7}(\text{stat.})_{-1.8}^{+2.4}(\text{syst.}) \text{ pb}$$

for $P_J < 5\%$. Signal and background estimates after

TABLE XXVIII: Summary of the background estimate in the double tag sample for $P_J < 1\%$.

Jet Multiplicity	2 jets	3 jets	≥ 4 jets
Electroweak			
WW	0.05 ± 0.02	0.03 ± 0.02	0.006 ± 0.006
WZ	0.25 ± 0.05	0.03 ± 0.01	0.013 ± 0.006
ZZ	0.014 ± 0.005	0.001 ± 0.001	0.001 ± 0.001
Single Top $W - g$	0.17 ± 0.03	0.12 ± 0.03	0.05 ± 0.01
Single Top W^*	0.88 ± 0.17	0.14 ± 0.03	0.035 ± 0.007
$Z \rightarrow \tau^+ \tau^-$	0.06 ± 0.06	0 ± 0	0 ± 0
Total	1.4 ± 0.3	0.33 ± 0.06	0.10 ± 0.02
W + Heavy Flavour			
Wbb	6.2 ± 2.0	0.89 ± 0.29	0.61 ± 0.21
$Wc\bar{c}$	0.38 ± 0.17	0.13 ± 0.06	0.077 ± 0.046
Wc	0.13 ± 0.08	0.03 ± 0.03	0.02 ± 0.02
Total	6.7 ± 2.1	1.1 ± 0.3	0.71 ± 0.24
Others			
Mistag	0.21 ± 0.05	0.10 ± 0.02	0.12 ± 0.03
Non- W	0.19 ± 0.12	0.03 ± 0.02	0.05 ± 0.03
Total Background	8.5 ± 2.3	1.5 ± 0.4	0.97 ± 0.25
Data	13	12	18

TABLE XXIX: Summary of the background estimate in the double tag sample for $P_J < 5\%$.

Jet Multiplicity	2 jets	3 jets	≥ 4 jets
Electroweak			
WW	0.29 ± 0.06	0.13 ± 0.04	0.07 ± 0.03
WZ	0.51 ± 0.10	0.06 ± 0.02	0.03 ± 0.01
ZZ	0.026 ± 0.007	0.004 ± 0.002	0.002 ± 0.001
Single Top $W - g$	0.39 ± 0.07	0.23 ± 0.04	0.09 ± 0.02
Single Top W^*	1.5 ± 0.3	0.26 ± 0.05	0.06 ± 0.01
$Z \rightarrow \tau^+ \tau^-$	0.07 ± 0.07	0 ± 0	0 ± 0
Total	2.83 ± 0.51	0.70 ± 0.12	0.25 ± 0.05
W + Heavy Flavour			
Wbb	11.5 ± 3.7	1.8 ± 0.6	1.2 ± 0.4
$Wc\bar{c}$	2.4 ± 0.9	0.61 ± 0.24	0.45 ± 0.19
Wc	0.98 ± 0.38	0.25 ± 0.11	0.19 ± 0.09
Total	14.9 ± 4.7	2.6 ± 0.8	1.9 ± 0.6
Others			
Mistag	2.7 ± 0.9	1.0 ± 0.3	1.3 ± 0.4
Non- W	0.63 ± 0.34	0.09 ± 0.05	0.14 ± 0.09
Total Background	21.1 ± 5.1	4.4 ± 0.9	3.5 ± 0.7
Data	28	22	39

the iterative procedure are shown in Table XXX, together with the observed number of events. Figure 21 compares the numbers of observed data to background and signal expectations for $P_J < 1\%$ and 5% for the measured $t\bar{t}$ production cross sections.

The statistical uncertainty on the measured cross section is dominated by the data sample size. Table XXXI summarizes the systematic contributions to the cross section uncertainty.

TABLE XXX: Summary of the final signal and background estimates and observed data in the double tag sample. MC derived refers to electroweak processes.

Jet Multiplicity	2 jets	3 jets	≥ 4 jets
Pretag Data	4442	300	166
$P_J < 1\%$			
MC Derived	1.4 ± 0.3	0.33 ± 0.06	0.10 ± 0.02
$Wb\bar{b}$	6.1 ± 1.9	0.57 ± 0.19	0.10 ± 0.03
$Wc\bar{c}$	0.38 ± 0.17	0.09 ± 0.04	0.013 ± 0.008
Wc	0.12 ± 0.08	0.02 ± 0.02	0.003 ± 0.003
Mistag	0.21 ± 0.05	0.06 ± 0.01	0.019 ± 0.004
Non- W	0.19 ± 0.12	0.03 ± 0.02	0.05 ± 0.03
Total Background	8.4 ± 2.2	1.1 ± 0.3	0.28 ± 0.06
$t\bar{t}$ (11.1 pb)	3.9 ± 0.9	10.2 ± 2.0	18.4 ± 3.4
Data	13	12	18
$P_J < 5\%$			
MC Derived	2.83 ± 0.51	0.70 ± 0.12	0.25 ± 0.05
$Wb\bar{b}$	11.4 ± 3.6	1.1 ± 0.3	0.16 ± 0.05
$Wc\bar{c}$	2.3 ± 0.9	0.38 ± 0.15	0.06 ± 0.03
Wc	0.97 ± 0.37	0.16 ± 0.07	0.03 ± 0.01
Mistag	2.7 ± 0.8	0.65 ± 0.20	0.15 ± 0.05
Non- W	0.63 ± 0.34	0.09 ± 0.05	0.14 ± 0.09
Total Background	20.9 ± 5.0	3.1 ± 0.6	0.80 ± 0.15
$t\bar{t}$ (11.6 pb)	7.5 ± 1.5	20.5 ± 3.7	36.6 ± 6.1
Data	28	22	39

TABLE XXXI: Summary of the systematical uncertainties in the double tag analysis.

Source	Fractional Syst. Uncert. (%)	Contribution to $\sigma_{t\bar{t}}$ (%)	
		$P_J < 1\%$	$P_J < 5\%$
Central Electron ID	1.6	+0.98/-0.96	+0.98/-0.96
Central Muon ID	1.9	+0.60/-0.60	+0.61/-0.60
CMX Muon ID	1.8	+0.21/-0.21	+0.21/-0.21
PDF	2	+2.1/-2.0	+2.1/-2.0
Jet Energy Scale	4.2	+4.5/-4.1	+4.5/-4.1
Lepton Isolation	2	+2.1/-2.0	+2.1/-2.0
ISR/FSR	1.3	+1.3/-1.3	+1.3/-1.3
MC Modeling	1.6	+1.7/-1.6	+1.7/-1.6
Z Vertex	2.0	+2.1/-2.0	+2.1/-2.0
Tagging SF $P_J < 1\%$ (b's/c's)	8.6/12.9	+20.3/-14.7	—
Tagging SF $P_J < 5\%$ (b's/c's)	8.5/12.7	—	+18.3/-13.6
Mistag Asymmetry $P_J < 1\%$	11.0	+0.063/-0.063	—
Mistag Asymmetry $P_J < 5\%$	15.5	—	+0.44/-0.44
Non- W Fraction	50	0.060	0.092
Non- W Prediction	50	0.13	0.21
W+HF Prediction	30	0.84	1.0
Cross Sections Bkg.	1.8	0.027	0.030
Luminosity	5.9	+6.4/-5.7	+6.4/-5.7
Total Systematic Uncertainty		+22.2/-16.8	+20.4/-15.9

B. Cross Section Dependence on the Top Quark Mass

in an analogous way to Section VIII A. Results are

We study the dependence of the $t\bar{t}$ cross section

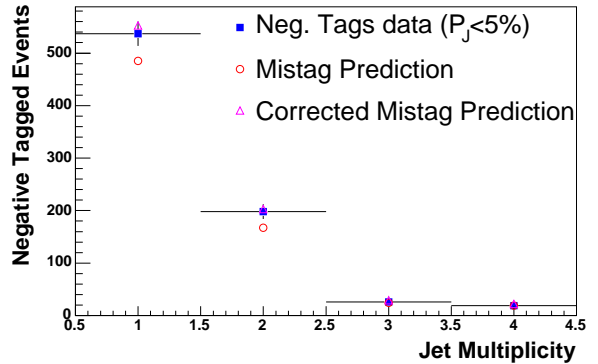
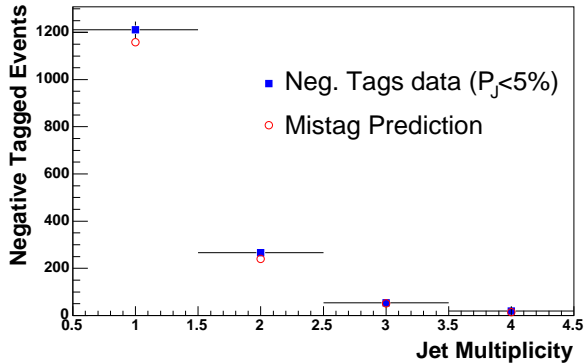
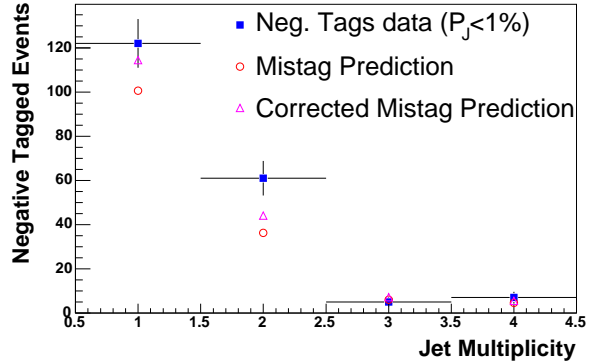
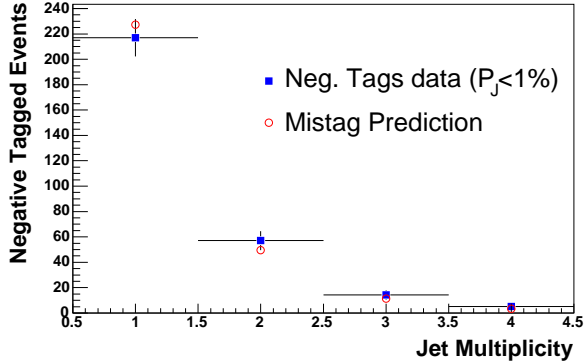


FIG. 17: Events with negative tagged jets compared to the prediction using the mistag matrix. We select events in the high- p_T lepton sample with $\cancel{E}_T < 20$ GeV. P_J cuts of 1% and 5% are used on the top and bottom plots respectively.

FIG. 18: Events with negative tagged jets (squares) in the pretag lepton+jets sample compared to the prediction using the mistag matrix before (empty circles) and after (empty triangles) heavy flavor corrections for $P_J < 1\%$ (5%) in the top (bottom) plot.

shown in Fig. 22. A linear fit to the measured cross sections as a function of the top mass returns a slope of -0.096 ± 0.022 pb/(GeV/c²) and -0.082 ± 0.019 pb/(GeV/c²) for $P_J < 1\%$ and $P_J < 5\%$, respectively, where the uncertainties are due to Monte Carlo simulation statistics. As before, note that the fit results for $m_t = 178$ GeV/c² agree with the measured cross section within the 1.6% uncertainty estimated in Section VII due to different modeling in PYTHIA and HERWIG.

C. Comparison Between Single and Double Tag Cross Sections

Although the measurements of the single and double tag cross sections are statistically compatible, we observe a ratio of about 1.2 between the measured cross sections in the double and single tag samples. We use pseudo-experiments to estimate the probabil-

ity to obtain a cross section greater than the measured double tag cross section when we assume that the measured single tag cross section is correct. For each pseudo-experiment, we vary the total double tag background estimate according to a Gaussian distribution with a width equal to its uncertainty. Successively, we add the background to the expected signal by assuming the single tag $t\bar{t}$ cross section and we vary the total number of events according to a Poisson distribution. We repeat this procedure 10,000 times and count the number of pseudo-experiments in which we have a result greater than the one observed in data. We find a probability of 13.2% for $P_J < 1\%$ and 15.6% for $P_J < 5\%$.

The systematic uncertainty in the double tag measurement is dominated by the uncertainties on the acceptance, luminosity and tagging scale factor. The systematic uncertainties on the background prediction are negligible. A bias on the values of acceptance and luminosity would affect the cross section

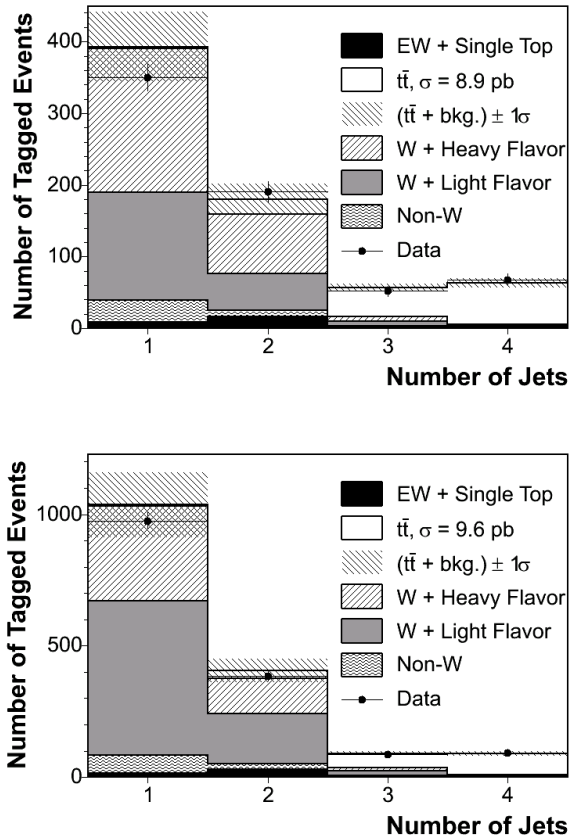


FIG. 19: Single tag data and background contributions (for an integrated luminosity of 318 pb^{-1}) as a function of the event jet multiplicity for $P_J < 1\%$ (top) and $P_J < 5\%$ (bottom). A top mass of $m_t = 178 \text{ GeV}/c^2$ is assumed.

measurement in the single and double tag samples in the same way. However, a bias on the tagging scale factor would have a greater effect in the double tag analysis than in the single tag one. To study this, we vary the tagging scale factor by $\pm 1\sigma$ and we repeat the cross section measurements and the pseudo-experiments. Results are summarized in Tables XXXII and XXXIII. As expected, the cross sections measured in the double tag sample are more sensitive to a change in the scale factor, resulting in a better agreement between the single and double tag cross sections when a larger value for the scale factor is used.

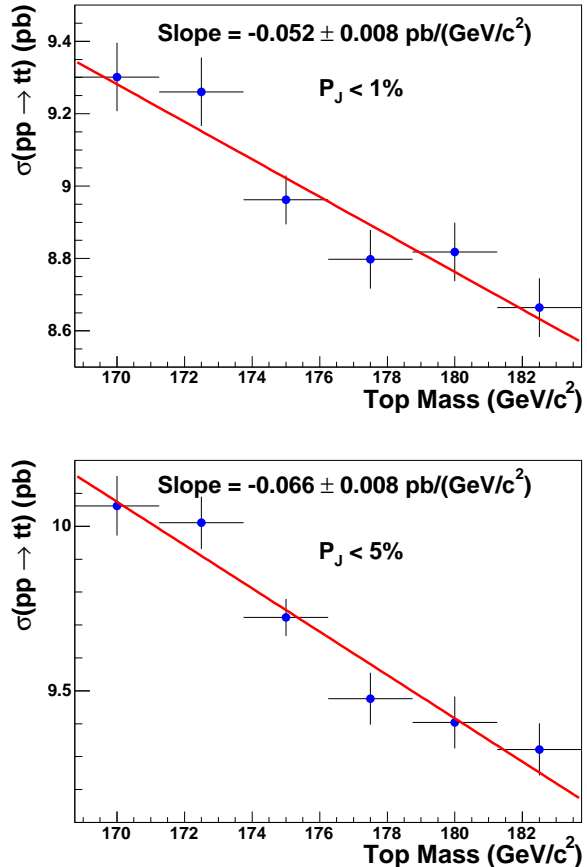


FIG. 20: Top pair production cross sections as a function of the top quark mass for $P_J < 1\%$ (top) and $P_J < 5\%$ (bottom). The uncertainties shown are the statistical uncertainties on the acceptances for each mass.

X. CONCLUSIONS

We present a measurement of the $t\bar{t}$ production cross section in $p\bar{p}$ collisions at $\sqrt{s} = 1.96 \text{ TeV}$ with an integrated luminosity of $318 \pm 18 \text{ pb}^{-1}$ at the CDF detector. We select events compatible with the $t\bar{t} \rightarrow lvq\bar{q}b\bar{b}$ decay mode by requiring one isolated electron (muon) with transverse energy E_T (p_T) $> 20 \text{ GeV}$ and missing transverse energy $\cancel{E}_T > 20 \text{ GeV}$ and at least three jets with transverse energy $E_T > 15 \text{ GeV}$. We further require at least one jet tagged by the jet probability algorithm. This selection accepts an estimated $(3.5 \pm 0.3)\%$ of all $t\bar{t}$ events when a $P_J < 1\%$ cut is applied, and an estimated $(4.4 \pm 0.4)\%$ with a looser P_J cut at 5%. Backgrounds are estimated using data and Monte Carlo simulations. We find good agreement with the observed data in a control region defined by events with W+one or two

TABLE XXXII: Cross section for $t\bar{t}$ event production in single and double tag analysis for $P_J < 1\%$ and $< 5\%$ and different values of the tagging scale factors (SF). Results are expressed in pb.

	$SF - 1\sigma$	SF	$SF + 1\sigma$
$P_J < 1\%, \leq 1$ tag	$9.8^{+1.1}_{-1.0}(\text{stat.})^{+1.3}_{-1.1}(\text{syst.})$	$8.9^{+1.0}_{-1.0}(\text{stat.})^{+1.1}_{-1.0}(\text{syst.})$	$8.3^{+1.0}_{-0.9}(\text{stat.})^{+1.0}_{-0.9}(\text{syst.})$
$P_J < 1\%, \leq 2$ tags	$13.3^{+2.8}_{-2.3}(\text{stat.})^{+3.3}_{-2.4}(\text{syst.})$	$11.1^{+2.3}_{-1.9}(\text{stat.})^{+2.5}_{-1.9}(\text{syst.})$	$9.4^{+2.0}_{-1.7}(\text{stat.})^{+2.0}_{-1.4}(\text{syst.})$
$P_J < 5\%, \leq 1$ tag	$10.5^{+1.1}_{-1.0}(\text{stat.})^{+1.3}_{-1.2}(\text{syst.})$	$9.6^{+1.0}_{-0.9}(\text{stat.})^{+1.2}_{-1.1}(\text{syst.})$	$9.0^{+1.0}_{-0.9}(\text{stat.})^{+1.1}_{-1.0}(\text{syst.})$
$P_J < 5\%, \leq 2$ tags	$13.7^{+2.0}_{-1.7}(\text{stat.})^{+3.3}_{-2.4}(\text{syst.})$	$11.6^{+1.7}_{-1.5}(\text{stat.})^{+2.4}_{-1.8}(\text{syst.})$	$9.9^{+1.5}_{-1.3}(\text{stat.})^{+2.0}_{-1.5}(\text{syst.})$

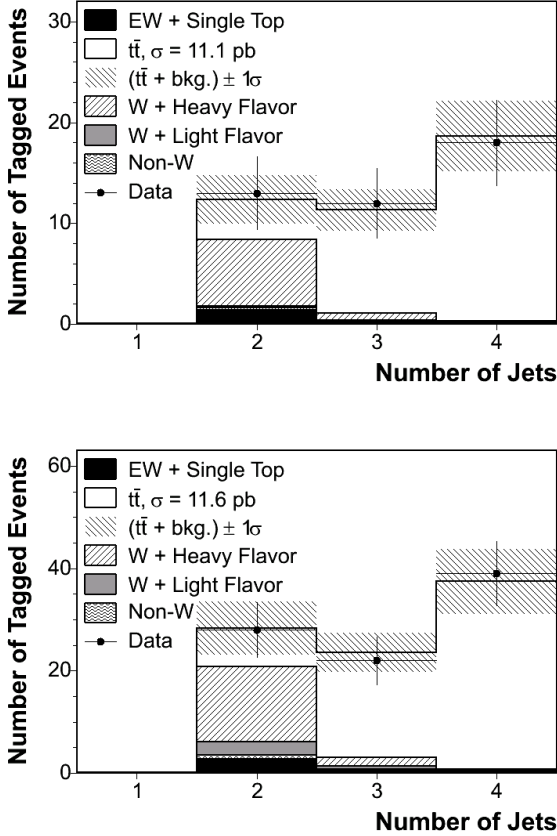


FIG. 21: Double tag data and background contributions (for an integrated luminosity of 318 pb^{-1}) as a function of the event jet multiplicity for $P_J < 1\%$ (top) and $P_J < 5\%$ (bottom). A top mass of $m_t = 178 \text{ GeV}/c^2$ is assumed.

jets. Using the excess of events with three or more jets and at least one b tag with $P_J < 1\%$, we measure a top pair production cross section of

$$\sigma_{t\bar{t}} = 8.9^{+1.0}_{-1.0}(\text{stat.})^{+1.1}_{-1.0}(\text{syst.}) \text{ pb.}$$

As cross checks, we measure the cross section using

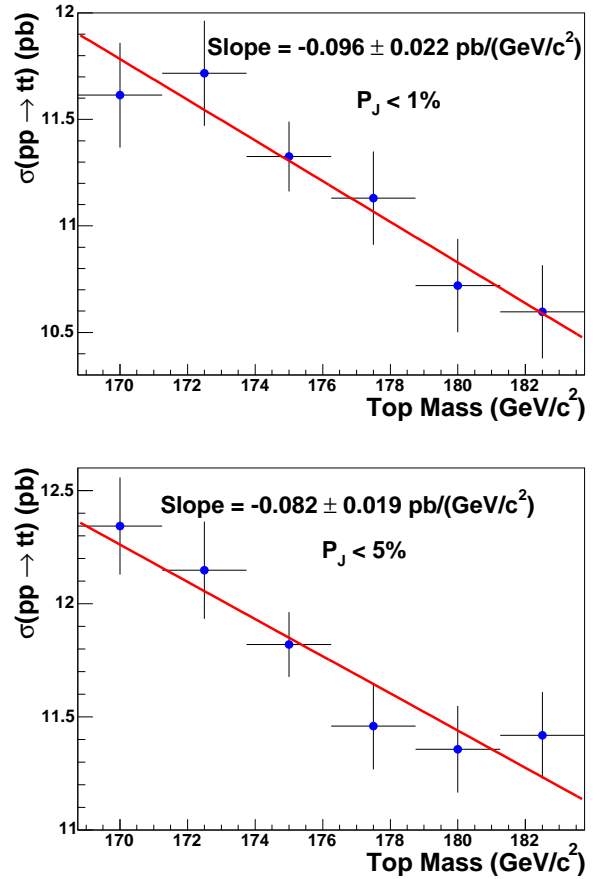


FIG. 22: Top pair production cross sections as a function of the top quark mass for $P_J < 1\%$ (top) and $P_J < 5\%$ (bottom) in the double tag analysis. The uncertainties shown are the statistical uncertainties on the acceptances for each mass.

samples with different b -tagging requirements. Using events with at least one b tag with $P_J < 5\%$ we obtain

$$\sigma_{t\bar{t}} = 9.6^{+1.0}_{-0.9}(\text{stat.})^{+1.2}_{-1.1}(\text{syst.}) \text{ pb.}$$

We also measure the $t\bar{t}$ production cross section in

TABLE XXXIII: Probability to measure a cross section greater than the one obtained in the double tag analysis when the $t\bar{t}$ cross section measured in the single tag analysis is assumed.

	$SF - 1\sigma$	SF	$SF + 1\sigma$
$P_J < 1\%$	4.5%	13.2%	30%
$P_J < 5\%$	2.8%	15.6%	35%

events with at least two tagged jets. The acceptance for signal events is estimated to be $(0.8 \pm 0.1)\%$ for $P_J < 1\%$ and $(1.5 \pm 0.3)\%$ for $P_J < 5\%$. We measure a cross section of

$$\sigma_{t\bar{t}} = 11.1^{+2.3}_{-1.9}(\text{stat.})^{+2.5}_{-1.9}(\text{syst.}) \text{ pb}$$

for $P_J < 1\%$ and

$$\sigma_{t\bar{t}} = 11.6^{+1.7}_{-1.5}(\text{stat.})^{+2.4}_{-1.8}(\text{syst.}) \text{ pb}$$

for $P_J < 5\%$.

Figure 23 shows our main result together with other CDF $t\bar{t}$ cross section measurements and theoretical predictions. Our result is above the central theoretical value by $\sim 1.9\sigma$. It should be noted that our result is highly correlated with the lepton+jets measurement using secondary vertex b -tagging, described in [40], where a comparison between the jet probability and secondary vertex b -taggers is given.

Acknowledgments

We thank the Fermilab staff and the technical staffs of the participating institutions for their vital contributions. This work was supported by the U.S. Department of Energy and National Science Foundation; the Italian Istituto Nazionale di Fisica Nucleare; the Ministry of Education, Culture, Sports, Science and Technology of Japan; the Natural Sciences and Engineering Research Council of Canada; the National Science Council of the Republic of China; the Swiss National Science Foundation; the A.P. Sloan Foundation; the Bundesministerium für Bildung und Forschung, Germany; the Korean Science and Engineering Foundation and the Korean Research Foundation; the Particle Physics and Astronomy Research Council and the Royal Society, UK; the Russian Foundation for Basic Research; the Comisión Interministerial de Ciencia y Tecnología, Spain; the European Community's Human Potential Programme under contract HPRN-CT-2002-00292; and the Academy of Finland.

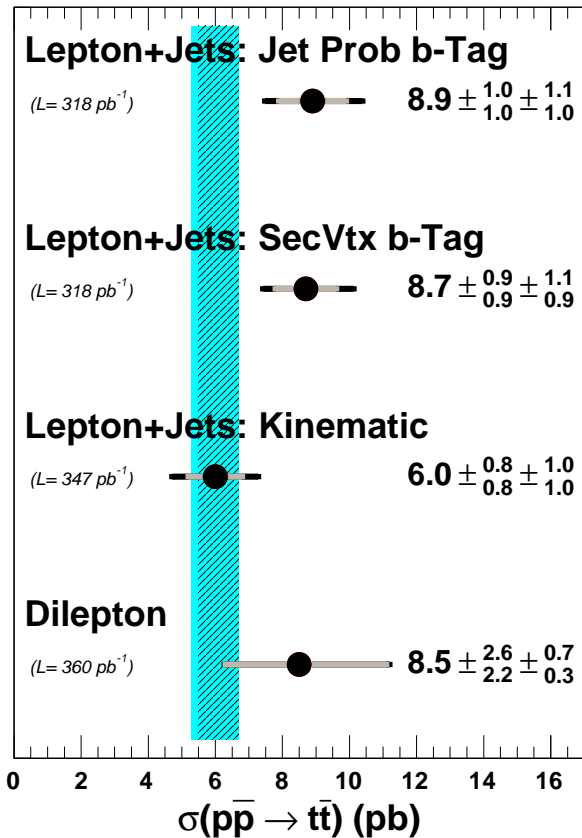


FIG. 23: Comparison of the $t\bar{t}$ production cross section measurement presented in this paper with theoretical predictions (solid band [1], dashed band [4]). Also shown are the CDF results obtained in the lepton+jets channel when using the secondary vertex tagger [40] and when no b -tagging is applied (only kinematic information) [41], and the result obtained in the dilepton channel [42]. All the measured cross sections are evaluated at $m_t = 178 \text{ GeV}/c^2$. The grey (black) lines represent the statistical (total) uncertainties. For the dilepton analysis, the grey (black) lines represent the uncertainties coming from the fit (shape).

APPENDIX: KINEMATIC DISTRIBUTIONS

We compare the distributions for different kinematic variables observed in data to the expectations for signal and backgrounds derived from a combination of simulation and $t\bar{t}$ cross section measurements. Figures 24 to 27 show the results for the four samples of events passing the selection criteria with at least three jets and one or two tags for $P_J < 1\%$ or $P_J < 5\%$. The considered kinematic variables are the sum of the transverse energies of each object in the final state (H_T), the reconstructed transverse mass

of the W boson, the missing transverse energy (E_T) of the event, the E_T of the lepton, the transverse energy of the tagged jets, and the pseudo-rapidity of the tagged jets with respect to the center of the detector. Kolmogorov-Smirnov (KS) probabilities are computed to test the agreement between observed and expected distributions. The distributions observed in the data are statistically consistent with the expected signal-plus-background distributions.

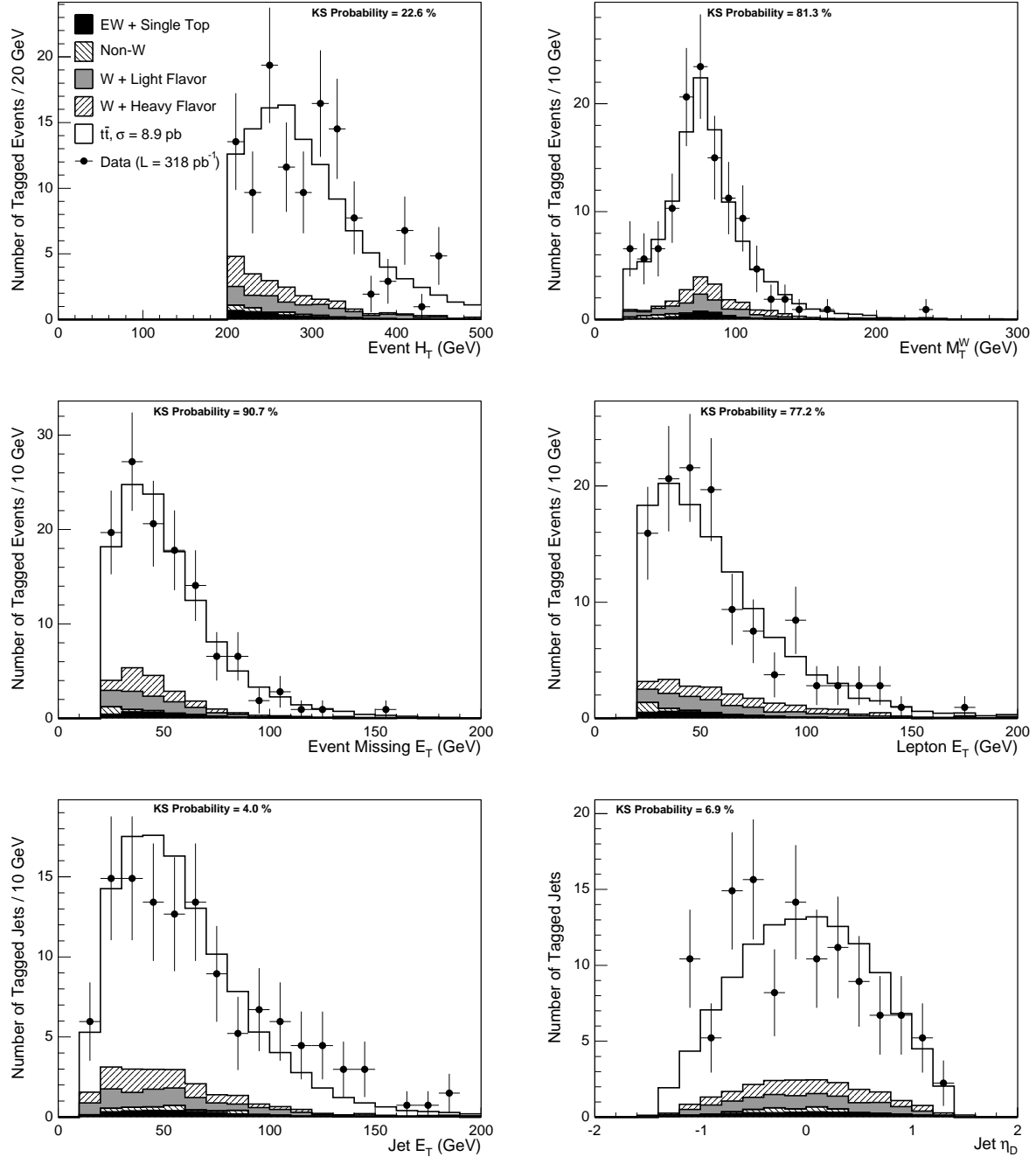


FIG. 24: Comparison of kinematic distributions in data to signal and background expectations for events passing the selection criteria with at least three jets and at least one tag for $P_J < 1\%$. From the top-left corner: sum of the transverse energies of each object in the final state (H_T), reconstructed transverse mass of the W boson, missing transverse energy (\cancel{E}_T), lepton E_T , transverse energy of the tagged jets, and the pseudo-rapidity of the tagged jets with respect to the center of the detector.

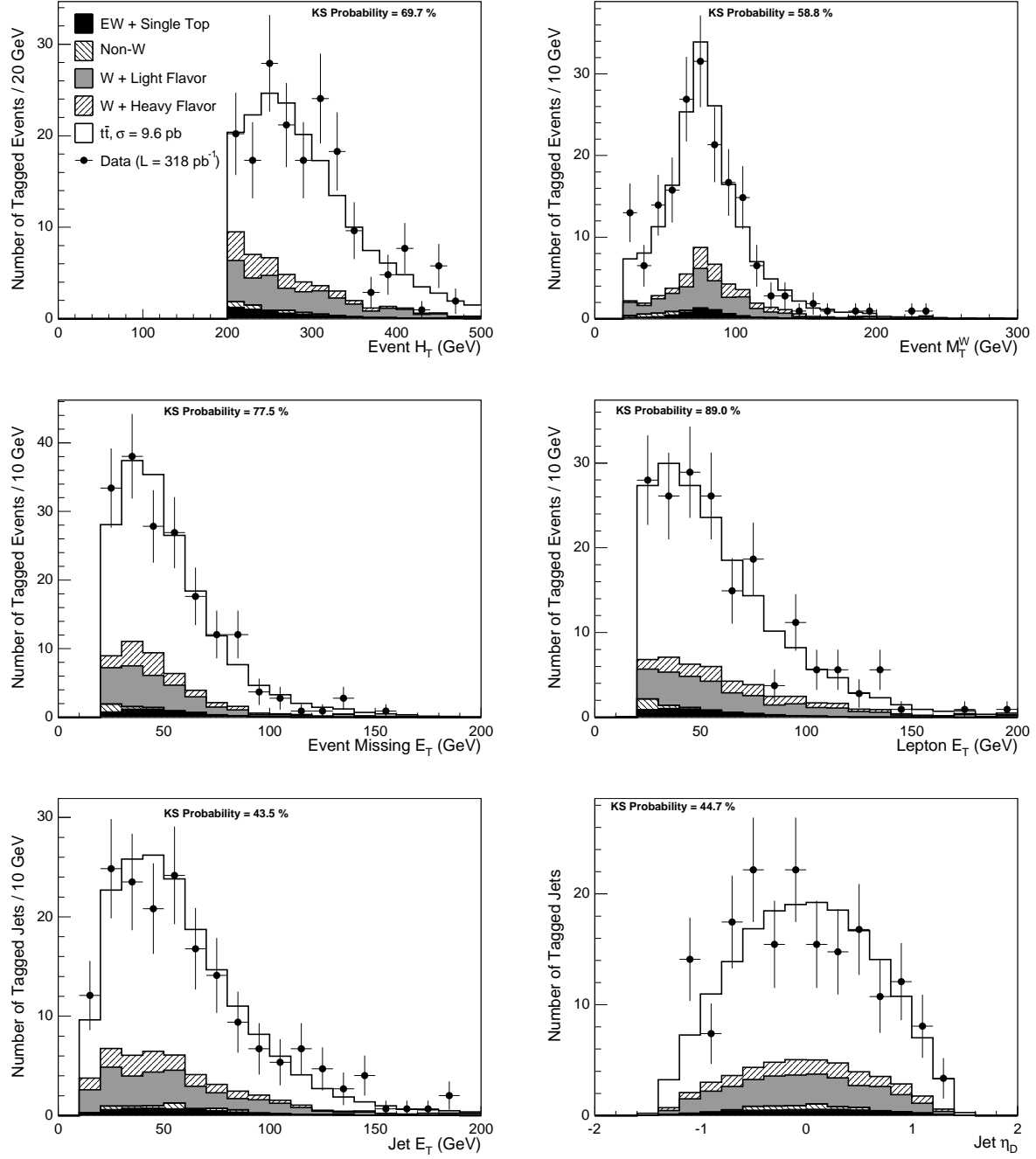


FIG. 25: Comparison of kinematic distributions in data to signal and background expectations for events in the single tag sample ($P_J < 5\%$).

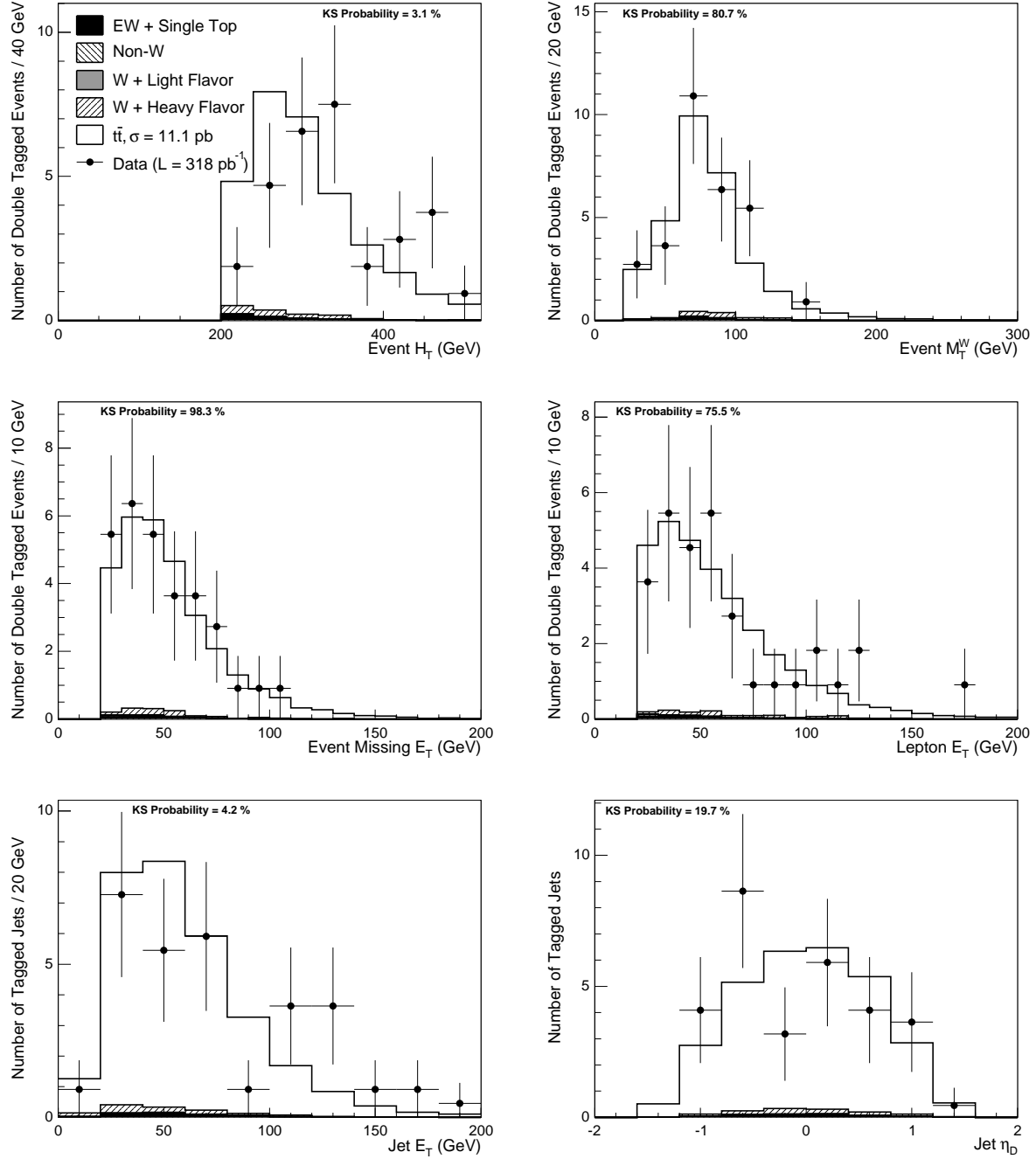


FIG. 26: Comparison of kinematic distributions in data to signal and background expectations for events in the double tag sample ($P_J < 1\%$).

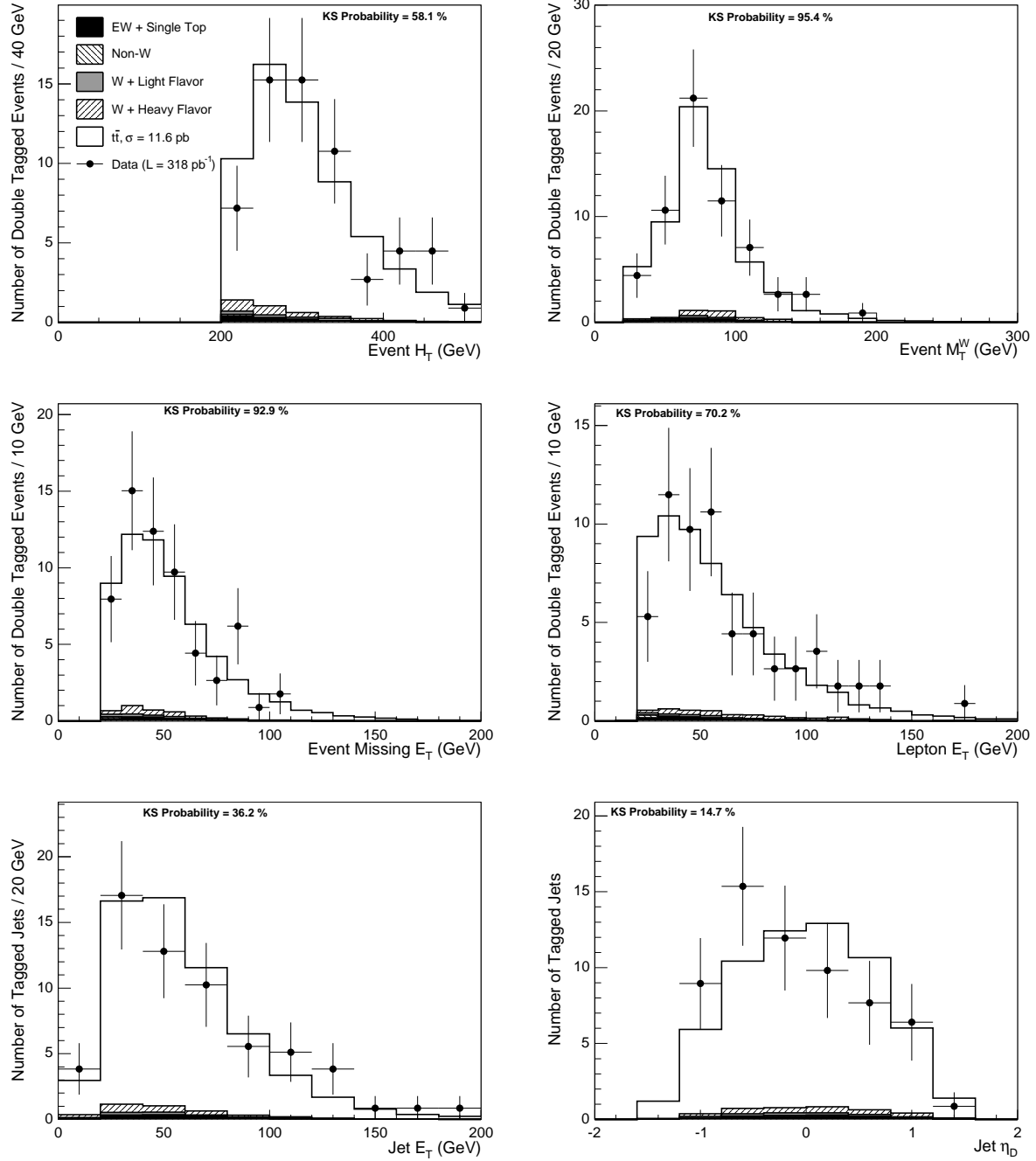


FIG. 27: Comparison of kinematic distributions in data to signal and background expectations for events in the double tag sample ($P_J < 5\%$).

-
- [1] M. Cacciari, S. Frixione, G. Ridolfi, M. Mangano, and P. Nason, *J. High Energy Phys.* **0404**, 068 (2004).
- [2] N. Kidonakis and R. Vogt, *Phys. Rev. D* **68**, 114014 (2003).
- [3] P. Azzi *et al.* (CDF/DØ Collaborations), hep-ex/0404010.
- [4] A. Affolder *et al.* (CDF Collaboration), *Phys. Rev. D* **64**, 032002 (2001), Erratum-ibid: *Phys. Rev. D* **67**, 119901 (2003); V.M. Abazov *et al.* (DØ Collaboration), *Phys. Rev. D* **67**, 012004 (2003).
- [5] D. Acosta *et al.* (CDF Collaboration), *Phys. Rev. Lett.* **93**, 142001 (2004).
- [6] D. Acosta *et al.* (CDF Collaboration), *Phys. Rev. D* **71**, 072005 (2005).
- [7] D. Acosta *et al.* (CDF Collaboration), *Phys. Rev. D* **71**, 052003 (2005).
- [8] D. Acosta *et al.* (CDF Collaboration), *Phys. Rev. D* **72**, 032002 (2005).
- [9] D. Acosta *et al.* (CDF Collaboration), *Phys. Rev. D* **72**, 052003 (2005).
- [10] D. Acosta *et al.* (CDF Collaboration), *Phys. Rev. D* **71**, 032001 (2005).
- [11] A. Affolder *et al.* (CDF Collaboration), *Nucl. Instrum. Methods A* **526**, 249 (2004).
- [12] A. Sill *et al.* (CDF Collaboration), *Nucl. Instrum. Methods A* **447**, 1 (2000).
- [13] A. Affolder *et al.* (CDF Collaboration), *Nucl. Instrum. Methods A* **453**, 84 (2000).
- [14] L. Balka *et al.* (CDF Collaboration), *Nucl. Instrum. Methods A* **267**, 272 (1988).
- [15] M. Albrow *et al.* (CDF Collaboration), *Nucl. Instrum. Methods A* **480**, 524 (2002).
- [16] S. Bertolucci *et al.* (CDF Collaboration), *Nucl. Instrum. Methods A* **267**, 301 (1988).
- [17] F. Abe *et al.* (CDF Collaboration), *Phys. Rev. Lett.* **68**, 1104 (1992).
- [18] G. Ascoli *et al.*, *Nucl. Instrum. Methods A* **268**, 33 (1988).
- [19] T. Dorigo *et al.* (CDF Collaboration), *Nucl. Instrum. Methods A* **461**, 560 (2001).
- [20] D. Acosta *et al.* (CDF Collaboration), *Nucl. Instrum. Methods A* **494**, 57 (2002).
- [21] S. Klimentenko, J. Konigsberg, and T.M. Liss, FERMILAB-FN-0741 (2003).
- [22] E. J. Thomson *et al.*, *IEEE Trans. Nucl. Sci.* **49**, 1063 (2002).
- [23] A. Abulencia *et al.* (CDF Collaboration), hep-ex/0508029.
- [24] F. Abe *et al.* (CDF Collaboration), *Phys. Rev. D* **45**, 1448 (1992).
- [25] A. Bhatti *et al.*, hep-ex/0510047, Fermilab-Pub-05-470.
- [26] T. Sjostrand *et al.*, *Comput. Phys. Commun.* **135**, 238 (2001).
- [27] G. Corcella *et al.*, *J. High Energy Phys.* **0101**, 010 (2001).
- [28] H.L. Lai *et al.* (CTEQ Collaboration), *Eur. Phys. J* **C12**, 375 (2000).
- [29] P. Avery, K. Read, and G. Trahern, CLEO Report CSN-212, 1985 (Unpublished).
- [30] M. Mangano *et al.*, *J. High Energy Phys.* **0307**, 001 (2003).
- [31] R. Brun and F. Carminati, CERN Programming Library Long Writeup **W5013** 1993.
- [32] R. Veenhof, *Nucl. Instrum. Methods A* **419**, 726 (1998).
- [33] G. Grindhammer, M. Rudowitz, and S. Peters, *Nucl. Instrum. Methods A* **290**, 469 (1990).
- [34] E. Gerchtein and M. Paulini, ECONF **C0303241**, TUMT005 (2003), physics/0306031.
- [35] D. Buskulic *et al.* (ALEPH Collaboration), *Phys. Lett. B* **313**, 535 (1993); F. Abe *et al.* (CDF Collaboration), *Phys. Rev. D* **53**, 1051 (1996); A. Affolder *et al.* (CDF Collaboration), *Phys. Rev. D* **64**, 032002 (2001), Erratum-ibid: *Phys. Rev. D* **67**, 119901 (2003).
- [36] S. Eidelman *et al.* (Particle Data Group), *Phys. Lett. B* **592**, 1 (2004).
- [37] J.M. Campbell *et al.*, *Phys. Rev. D* **60**, 113006 (2002).
- [38] B.W. Harris *et al.*, *Phys. Rev. D* **66**, 054024 (2002).
- [39] D. Acosta *et al.* (CDF Collaboration), *Phys. Rev. Lett.* **94**, 091803 (2005).
- [40] A. Abulencia *et al.* (CDF Collaboration), hep-ex/0606017.
- [41] J. Guimaraes da Costa (CDF Collaboration), FERMILAB-PUB-05-593-E (2005).
- [42] In preparation, to be submitted to *Phys. Rev. Lett.*